


2020-01-01

Investigation Of Iron Doped Gallium Oxide (Ga-Fe-O) System: Structure Property Relationship And Performance Evaluation For Optical And Catalytic Applications

Swadipta Roy
University of Texas at El Paso

Follow this and additional works at: https://scholarworks.utep.edu/open_etd

 Part of the [Chemistry Commons](#), [Materials Science and Engineering Commons](#), and the [Mechanics of Materials Commons](#)

Recommended Citation

Roy, Swadipta, "Investigation Of Iron Doped Gallium Oxide (Ga-Fe-O) System: Structure Property Relationship And Performance Evaluation For Optical And Catalytic Applications" (2020). *Open Access Theses & Dissertations*. 3030.

https://scholarworks.utep.edu/open_etd/3030

This is brought to you for free and open access by ScholarWorks@UTEP. It has been accepted for inclusion in Open Access Theses & Dissertations by an authorized administrator of ScholarWorks@UTEP. For more information, please contact lweber@utep.edu.

INVESTIGATION OF IRON DOPED GALLIUM OXIDE (Ga-Fe-O) SYSTEM: STRUCTURE
PROPERTY RELATIONSHIP AND PERFORMANCE EVALUATION FOR OPTICAL AND
CATALYTIC APPLICATIONS

SWADIPTA ROY

Doctoral Program in Materials Science and Engineering

APPROVED:

Ramana V. Chintalapalle, Ph.D., Chair

Stephen W. Stafford, Ph.D.

David A. Roberson, Ph.D.

Skye Fortier, Ph.D.

Vaithiyalingam Shutthanandan, Ph.D.

Stephen L. Crites, Jr., Ph.D.
Dean of the Graduate School

Copyright ©

by

Swadipta Roy

2020

Dedication

I dedicate this dissertation work to my parents and to my family.

INVESTIGATION OF IRON DOPED GALLIUM OXIDE (Ga-Fe-O) SYSTEM: STRUCTURE
PROPERTY RELATIONSHIP AND PERFORMANCE EVALUATION FOR OPTICAL AND
CATALYTIC APPLICATIONS

by

SWADIPTA ROY, M.Tech

DISSERTATION

Presented to the Faculty of the Graduate School of

The University of Texas at El Paso

in Partial Fulfillment

of the Requirements

for the Degree of

DOCTOR OF PHILOSOPHY

Department of Metallurgical, Materials and Biomedical Engineering

THE UNIVERSITY OF TEXAS AT EL PASO

May 2020

Acknowledgements

First, I would like to thank my supervisor, Prof. Ramana V. Chintalapalle, for his relentless support and continuous guidance, financial support, and his overall help throughout my doctoral research programme. He directed me towards becoming a better scholar, researcher, as well as an efficient professional individual. I am very obliged for all his lessons and support that allowed me to complete this research.

I would like to thank Prof. Stephen W. Stafford (Metallurgical, Materials and Biomedical Engineering), Prof. David A. Roberson (Metallurgical, Materials and Biomedical Engineering), and Prof. Skye Fortier (Chemistry and Biochemistry), who agreed to be part of my doctoral committee and were willing to spend their valuable time to evaluate my dissertation research. Also, I am highly indebted to all of them for their noteworthy feedbacks during my doctoral research programme. I would also like to thank Dr. Vaithiyalingam Shutthanandan (external committee member), Dr. Vijayakumar Murugesan, Dr. Venkateshkumar Prabhakaran, Dr. Suntharampillai Thevuthasan and Mr. Abraham Martinez of Pacific Northwest National Laboratory (PNNL) for their continuous guidance and support during my internship days at Environmental and Molecular Sciences Laboratory (EMSL) of PNNL. I want to extend my gratitude to Joint Center for Energy Storage Research (JCESR) under Department of Energy (DOE) for the financial support during my internship period.

I would like to thank my past and present team members at UTEP: Dr. Gustavo Martinez, Dr. Sandeep Manandhar, Dr. Mallesh Bandi, Mr. Cristian Orozco, Mr. Vishal B. Zade and Mr. Anil K. Battu and all others who have helped me in this endeavor. I would like to dedicate this to my parents and family who always pushed me to accomplish my goals and without their continual support, this would not have been achieved.

I wish to express my sincere thanks to the DOE and National Science Foundation (NSF) for the financial support through research grants. Part of the research presented in this dissertation was supported by the DOE; however, the views and opinions expressed by the author(s) herein do not necessarily state or reflect those of the United States government or funding agency thereof.

Abstract

We report on the optimized synthesis conditions of iron (Fe)-doped gallium oxide (Ga_2O_3 ; $\text{Ga}_{1.9}\text{Fe}_{0.1}\text{O}_3$, referred to as GFO) inorganic compounds. The GFO materials were synthesized using a standard high-temperature solid-state chemical reaction method by maintaining the Fe doping amount constant. X-ray diffraction (XRD) revealed that GFO compounds crystallize in the β - Ga_2O_3 phase. The effect of the sintering temperature (T_{sint}), which was varied in the range of 900–1200 °C, is significant, as revealed by scanning electron microscopy (SEM) analysis. T_{sint} influences the grain size and microstructure evolution, which, in turn, influences the dielectric properties of GFO compounds. The energy-dispersive X-ray spectrometry (EDS) data demonstrate the uniform distribution of the elemental composition over the microstructure. The temperature and frequency-dependent dielectric measurements indicate the characteristic features that are specifically due to Fe doping in Ga_2O_3 . The results demonstrate that densification and control over the microstructure and properties of GFO can be achieved by optimizing T_{sint} .

New sets of GFO compounds were synthesized by varying the iron (Fe)-doping amount (i.e., $\text{Ga}_{2-x}\text{Fe}_x\text{O}_3$; $x = 0.00 - 0.30$) following the standard high-temperature (T_{sint} : 1200 °C) solid-state chemical reaction method. XRD studies of the sintered compounds provided evidence for the Fe^{3+} substitution at Ga^{3+} site without any secondary phase formation. Rietveld refinement of XRD patterns reveal that the GFO compounds crystallized in monoclinic crystal symmetry. X-ray photoelectron spectroscopy (XPS) data revealed that at lower concentrations of doping, Fe exhibited mixed chemical valence states, whereas single chemical valence state was evident for higher Fe content. Local structure and chemical bonding analyses using X-ray absorption near edge structure (XANES) revealed that the Fe occupied octahedral and tetrahedral sites similar to Ga in parent Ga_2O_3 lattice without considerable changes in the local symmetry. Raman

spectroscopy also confirmed the crystalline nature of the GFO compounds. Morphology of the GFO compounds was characterized by the presence of rod-shaped particle features employing SEM. The EDS confirmed the chemical stoichiometry of the GFO compounds, where the atomic ratio of the constituted elements was in accordance with the calculated concentration values.

Optical absorption spectra revealed a significant red shift in the optical band gap with Fe doping. Origin of the significant red shift is attributed to the strong sp-d exchange interaction originated from the 3d⁵ electrons of Fe³⁺. Coupled with optical band gap red shift, electrocatalytic studies of GFO compounds revealed that doped Ga₂O₃ compound exhibited electrocatalytic activity in contrast to intrinsic Ga₂O₃. Fe doped samples demonstrated appreciable electrocatalytic activity towards the generation of H₂ through electrocatalytic water splitting. Electrocatalytic activity of the GFO compounds is attributed to cumulative effect of different mechanisms such as doping resulted new catalytic centers, enhanced conductivity, and electron mobility. Hence, a new pathway in which electrocatalytic behavior of the GFO compounds resulted due to Fe chemical states, red shift in optical band gap was explored for the very first time. The implications derived from this work may be applicable to a large class of compounds and further options may be available to design functional materials for electrocatalytic energy production.

Table of Contents

Acknowledgements.....	v
Abstract	vii
Table of Contents.....	ix
List of Tables	xii
List of Figures.....	xiii
Chapter 1: Introduction	1
Chapter 2: Motivation and Significance of the Project.....	4
2.1 Research Objectives.....	5
2.1.1 Fabrication of Iron (Fe) Doped Ga ₂ O ₃ Compounds.....	5
2.1.2 Optimization of Synthesis Conditions	6
2.1.3 Establishing Structure-Property Correlation	6
2.1.4. Evaluation of Practical Application Potential.....	7
Chapter 3: Literature Review.....	9
3.1. Gallium Oxide	9
3.1.1 Crystal Structure of Gallium Oxide	11
α -Ga ₂ O ₃	12
β -Ga ₂ O ₃	13
γ -Ga ₂ O ₃	14
δ -Ga ₂ O ₃	15
ε -Ga ₂ O ₃	16
3.1.2 Gallium Oxide Crystal Growth and Hybrid Oxide Synthesis Techniques.....	17
Melt Growth	17
Solid-State Synthesis Method.....	18
3.1.3 Application of β -Ga ₂ O ₃	18
Electrocatalytic Properties of β -Ga ₂ O ₃	18
3.2 Iron(III) Oxide.....	19
Chapter 4: Materials and Methods.....	21
4.1 Materials	21
4.2 Synthesis Technique	21

4.3 Experimental Methods.....	22
4.3.1 Crystal Structure and Surface Morphology.....	22
X-ray Diffraction (XRD).....	22
Scanning Electron Microscope (SEM).....	24
4.3.2 Chemical Analysis.....	25
Energy-Dispersive X-ray Spectrometry (EDS).....	25
X-ray Photoelectron Spectroscopy (XPS).....	26
X-ray Absorption Near-Edge Structure (XANES).....	28
Raman Spectroscopy.....	29
4.3.3 Dielectric Properties.....	31
4.3.4 Spectral Selectivity - Optical Absorption.....	31
4.3.5 Electrocatalytic Activity Studies.....	32
Chapter 5: Effect of Sintering Temperature-Optimization of Synthesis Conditions.....	34
5.1 Crystal Structure and Surface Morphology.....	34
5.2 Chemical Analysis.....	45
5.2.1 Energy-Dispersive X-ray Spectroscopy (EDS).....	45
5.2.2 X-ray Photoelectron Spectroscopy (XPS).....	48
5.3 Dielectric Properties.....	52
Chapter 6: Effect of Variable Fe Concentration- GFO Compounds at Optimized Sintering Condition.....	61
6.1 Crystal Structure and Surface Morphology.....	61
6.2 Chemical Analysis.....	70
6.2.1 Energy-Dispersive X-ray Spectrometry (EDS).....	70
6.2.2 X-ray Photoelectron Spectroscopy (XPS).....	72
6.2.3 Local Structure and Bonding.....	77
6.3 Dielectric Properties.....	82
Chapter 7: Applications.....	90
7.1 Optical.....	90
7.2: Electrocatalytic Activity.....	94

Chapter 8: Summary and Conclusions	98
Chapter 9: Future Studies	101
Bibliography	102
Vita	122

List of Tables

Table 5.1: Lattice Parameter, Unit Cell Volume, Density and Relative Porosity of GFO Compounds for Different Sintering Conditions	38
Table 5.2: Raman data for $\text{Ga}_{1.9}\text{Fe}_{0.1}\text{O}_3$ ceramics at various T_{sint} . The data of $\text{Ga}_{1.9}\text{Fe}_{0.1}\text{O}_3$ ceramics is compared with that of bulk Ga_2O_3	43
Table 5.3: Average Particle Size Measured from SEM Micrograph	45
Table 5.4: Elemental Composition Data from EDS.....	47
Table 5.5: Calculated Values of the Spreading Factor (α) and Relaxation Time (τ) of GFO Compounds at Different T_{sint}	58
Table 6.1: Lattice Constant, Unit Cell Volume, Density, and Relative Porosity of GFO Compounds	64
Table 6.2: Unit Cell Parameters of GFO Compounds Obtained from Structural Refinement	66
Table 6.3: Rietveld Structural Refinement Parameters Obtained for GFO Compounds	67

List of Figures

Figure 1.1: Projection of energy production by IEA.	1
Figure 3.1: Synthesizing route of Ga ₂ O ₃ polymorphs.....	12
Figure 3.2: Crystal structure of α-Ga ₂ O ₃	13
Figure 3.3: Crystal structure of β-Ga ₂ O ₃	14
Figure 3.4: Crystal structure of γ-Ga ₂ O ₃ which is represented by an equivalent crystal structure of MgAl ₂ O ₄	15
Figure 3.5: Crystal Structure of δ-Ga ₂ O ₃ represented by an analogous crystal structure of In ₂ O ₃	16
Figure 3.6: ε-Ga ₂ O ₃ represented by an equivalent crystal structure of AlFeO ₃	17
Figure 3.7: Crystal structure of hematite unit cell.	20
Figure 4.1: Schematic diagram of X-ray interacting with a crystalline material.....	23
Figure 4.2: SEM working mechanism.....	25
Figure 4.3: Principle of EDS.	26
Figure 4.4: Basic functioning of an XPS system.	27
Figure 4.5: Fundamental working principle of XANES.	29
Figure 4.6: Raman spectroscopy setup.....	30
Figure 4.7: Potentiostat electric circuit diagram.	33
Figure 5.1: XRD patterns of GFO compounds as a function of T _{sint} . All of the GFO compounds crystallize in a monoclinic β phase of Ga ₂ O ₃ . It is evident that the peak intensity increases with increasing T _{sint}	37
Figure 5.2: Density variation of the GFO compounds with T _{sint} . It is evident that the density increases with increasing T _{sint}	38

Figure 5.3: Raman shifts of differently sintered GFO compounds.....	42
Figure 5.4: SEM images of GFO materials as a function of T_{sint} . Coalescence of grains occurs with increasing T_{sint}	45
Figure 5.5: EDS spectrum of the GFO material sintered at 1200 °C. The respective X-ray peaks due to Ga, Fe, and O atoms are as labeled.....	47
Figure 5.6: Elemental mapping images of GFO compounds synthesized at different T_{sint} . The corresponding SEM images are also shown. Chemical uniformity of the GFO samples is evident from the images.....	48
Figure 5.7: Survey spectra of GFO compounds at various sintering temperature.....	51
Figure 5.8: High resolution XPS spectra of (a) Ga 2p (b) O 1s (c) Fe 2p.....	52
Figure 5.9: Comparison of the real part of the dielectric constant of GFO materials synthesized at different T_{sint} . The frequency dispersion of the dielectric constant is shown.....	55
Figure 5.10: Comparison of the imaginary part of the dielectric constant of GFO materials prepared at different T_{sint}	56
Figure 5.11: Comparison of the loss tangent of GFO materials prepared at different T_{sint}	56
Figure 5.12: Variation of the real part of the dielectric constant of GFO materials prepared at different T_{sint} . The experimental and simulation data are shown. The dispersion behavior (experimental data) fits the modified Debye model (simulation data) function (see the text for the description).....	57
Figure 5.13: $\ln[(\epsilon'_{\omega} - \epsilon'_{\infty}) / (\epsilon'_{\omega} - \epsilon'_{\infty})]$ versus $\ln \omega$ plots of GFO materials. The spreading factor and relaxation time were calculated by fitting the curves.....	58

Figure 5.14: Temperature-dependent dielectric constant ϵ' (T) of GFO materials as a function of the sintering temperature. The data shown are obtained at a constant frequency of 1 MHz. It is evident that ϵ' (T) increases with increasing T_{sint}	60
Figure 6.1: XRD pattern of GFO compounds.	63
Figure 6.2: Variation of the theoretical density (ρ_{XRD}) of GFO compounds with Fe content. The unit cell volume values were determined from the XRD measurements.....	64
Figure 6.3: XRD patterns of GFO compounds. Rietveld structural refinement of XRD patterns is also presented. The experimental and calculated XRD patterns after the refinement are shown. Good agreement between the experimental and calculated XRD patterns can be noted.....	66
Figure 6.4: SEM data of $\text{Ga}_{(2-x)}\text{Fe}_x\text{O}_3$ compounds.....	70
Figure 6.5: Atomic ratio of constituent elements of GFO compounds obtained from EDS.	71
Figure 6.6: Elemental mapping of representative GFO compounds (Top $x=0.00$ and Bottom $x=0.30$, respectively). The data indicate the uniform distribution of the constituent elements. ...	72
Figure 6.7: XPS survey scans of selected GFO compositions sintered at 1200 °C for 6 hrs.....	74
Figure 6.8: High resolution XPS spectra of GFO ($0.00 \leq x \leq 0.30$) compounds (a) Ga 2p, and (b) O 1s.	75
Figure 6.9: Deconvoluted high resolution XPS spectra of Fe 2p region of GFO compounds.	76
Figure 6.10: XANES of (a) Ga L-edge, (b) O K-edge, (c) Fe L-edge, and (d) representative crystal structure of Ga_2O_3 with tetrahedral and octahedral coordination positions. Ga1 and Ga2 denote the tetrahedral and octahedral lattice sites in pure Ga_2O_3 compound, respectively. Oxygen atoms at their respective positions are represented by red circles.	81
Figure 6.11: (a) Frequency-dependent real part of dielectric constant, and (b) frequency dependent dissipation factor ($\tan \delta$) of GFO compounds.....	83

Figure 6.12: Variation of real part of the dielectric constant of GFO compounds with frequency. The dispersion behavior in all these plots fits to the modified Debye function.	85
Figure 6.13: Variation of $\ln[(\epsilon'_0 - \epsilon'_\omega)/(\epsilon'_\omega - \epsilon'_\infty)]$ vs $\ln \omega$ for GFO compounds at room temperature.	86
Figure 6.14: Variation of dielectric constant (ϵ') with temperature at different frequencies of the GFO compounds. (a) $x= 0.00$, (b) $x= 0.15$, (c) $x= 0.20$, and (d) $x= 0.30$	88
Figure 6.15: Variation of $\tan \delta$ with temperature at different frequencies of the GFO compounds. (a) $x= 0.00$, (b) $x= 0.15$, (c) $x= 0.20$, and (d) $x= 0.30$	89
Figure 7.1: (a) Optical absorption spectra of GFO. (b) Enlarged profile representing the intensity variation of peak associated with Fe^{3+} - Fe^{3+} double-excitation process (Inset: relative intensity of Fe-induced double-excitation edge vs Fe content).	92
Figure 7.2: Band gap variation with Fe content. Significant reduction in band gap in GFO compounds is evident.....	93
Figure 7.3: Schematic energy diagram of intrinsic and Fe-doped Ga_2O_3	93
Figure 7.4: Electrochemical characterization of the doped and undoped Ga_2O_3 . (a) Polarization curves obtained at a 20 mVs^{-1} scan rate and (b) Tafel slopes for $x= 0.15$ - and 0.30 -doped samples.	97
Figure 7.5: Hypothetical schematic showing the band positions in the conduction band for intrinsic and Fe-doped compounds.	97

Chapter 1: Introduction

Current world energy sector heavily relies on energy generated from the fossil fuel. The demand for fossil fuel-based energy production is ever increasing. The graphical presentation in Figure 1.1 demonstrates the projection by International Energy Agency (IEA) on different sources of energy production until 2040¹ and it is quite clear from the graph that the renewable source-based energy production is increasing gradually. Combustion of fossil fuel generates hazardous emissions such as NO_x, CO, CH₄, CO₂, SO₂ etc. which have environmental as well as health concerns. Furthermore, these gases contribute to the global warming. Non-fossil fuel based clean energy system has gained enormous interest from both academic and industrial sectors as a result of global warming which is the biggest threat to our existing world.

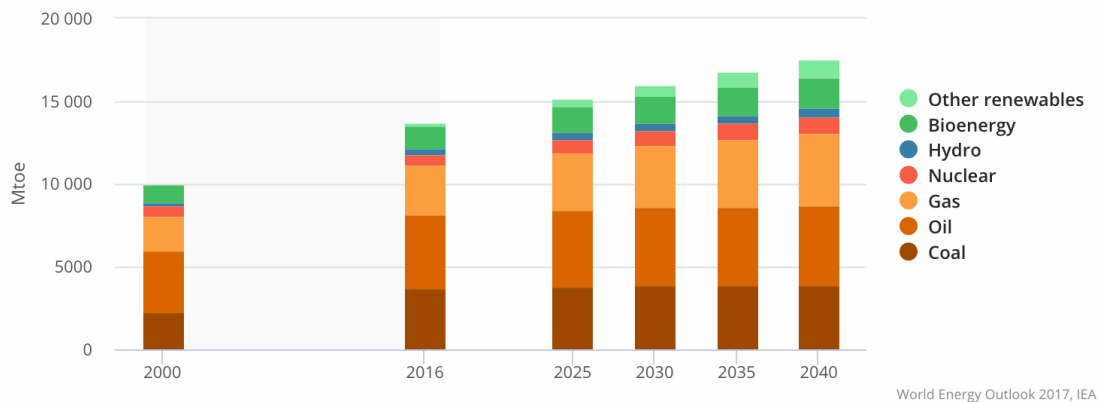


Figure 1.1: Projection of energy production by IEA.

Energy conversion technologies associated with different electrochemical reactions such as oxygen reduction reaction (ORR), hydrogen evolution reaction (HER), and oxygen evolution reaction (OER) have been recognized as efficient means in the energy conversion and storage technologies.²⁻⁶ However, electrode materials play a pivotal role in order to design high efficiency energy conversion systems that include fuel cell, water splitting devices, and metal-air batteries to generate hydrogen and oxygen.⁷⁻⁹ Currently, extensive research has been undertaken to develop

multifunctional diversified electrode materials for the aforementioned systems.¹⁰⁻¹¹ Hydrogen produced from HER in water splitting process can be used in proton exchange membrane-based fuel cell (PEMFC) as a clean fuel for corresponding anodic reaction (hydrogen oxidation reaction). Similarly, ORR is a significant cathodic reaction in PEMFC, where oxygen gets reduced as a result of water formation, so there has been a huge demand for a very active electrode material to meet the demand of the situation i.e. to integrate HER, ORR, and OER in order to develop a viable energy technology. Platinum (Pt) and Ir/Ru based materials are used for this purpose as state-of-the-art catalysts, but the cost of these materials is quite high as well as they are less durable and abundant in natural resources which limit their extensive application in industry.¹² Current efforts are devoted in developing a cost-effective multifunctional electrocatalyst materials with superior properties which can be made of less expensive high abundance natural material resources. Catalyst performance generally depends on the number of active sites that can be introduced through doping of active elements. However, interstitial defects can also act as active sites combined with enhanced surface area due to porous nature of the material system. Currently, researchers are devoting time in order to formulate a metal oxide based electrocatalyst for HER and ORR with good conductivity by introducing doping of carbonaceous elements, nitrogen, sulfur, and metallic backbones such as Pt/Ni/Mn,¹³⁻¹⁹ but the design of these metal oxides are very important considering several factors like harnessing maximum catalytic efficiency, specific surface area and structural porosity. It is reported that nanotubular shape,²⁰ 3D foam-like structure,²¹ and ordered mesoporous architecture,²² are the viable designs for this purpose. Electrospinning in addition with thermal treatment is currently being used for large scale catalyst fabrication. Being one of the versatile techniques, it has several advantages such as it can synthesize nanofibers with high specific surface area, controllable 3D architecture.

Electrospinning also has the ability of blending additives in situ. As a result, electrospinning technique has emerged as the most successful technique for the production of transition metal oxide nanofibers with mesoporous architecture for both HER and ORR.²³⁻²⁸ Other than electrospinning technique, solid state chemical reaction route can also be found useful for the fabrication of transition metal doped nanostructured electrocatalyst.

Catalytic activity of β -Ga₂O₃ whether synthesized by electrospinning process or solid-state reaction route, can be enhanced by fabricating nanoarchitecture and spongy porous-like structure. It is reported that nanofibers of gallium oxide (β -Ga₂O₃) synthesized by electrospinning process, showed electrocatalytic activity as a bifunctional material for both HER and ORR. β -Ga₂O₃ has a wide band gap (4.9 eV) range with very high breakdown potential of \sim 8 MV/cm, and because of these salient features, β -Ga₂O₃ has emerged as a superior material in the semiconducting industry as well as in power device applications.²⁹ β -Ga₂O₃ has ample amount of moderate Lewis acid sites on the surface which can influence its catalytic behavior.³⁰

Chapter 2: Motivation and Significance of the Project

While β -Ga₂O₃ can be fabricated in thin film and bulk forms, doping of various elements in thin film and bulk β -Ga₂O₃ has been attempted to tailor the functional properties.³¹ In order to alter electronic structure and derive new and enhanced properties, doping and alloying with selectively chosen elements is an efficient and proven method. For instance, it has been reported that the Sn and Cr doped β -Ga₂O₃ nanowires exhibit excellent luminescence properties suitable for display device applications.³² Metal doped Ga₂O₃ has been found to be attractive and exhibits superior catalytic activity for application in energy-harvesting devices. Enhanced catalytic activity has been observed in Ga₂O₃ by the approach of metal ion dopants such as Ni, Zn and Pb.³³⁻³⁵ However, the attention paid toward the optical, optoelectronic and catalytic properties of Fe-doped β -Ga₂O₃ is meager. Therefore, the present work was performed to fill this knowledge gap and also to explore the unexpected property realization (if possible) in Fe-doped β -Ga₂O₃.

Our focus and challenging goal of the present work is toward the synthesis and optimization of iron (Fe)-doped Ga₂O₃ compounds. However, as a first step for optimization of sintering temperature to obtain high-quality Fe-doped Ga₂O₃ compounds, we considered the selected composition of Ga_{1.9}Fe_{0.1}O₃. The impetus for the work on Fe-doped Ga₂O₃ (Ga_{1.9}Fe_{0.1}O₃, referred to as GFO) is as follows. To improve the Ga₂O₃ functionality with metal incorporation, the use of isovalent and/or multivalent ion(s) opens the possibility of designing materials for many strategic applications.³⁶⁻⁴² For instance, the emerging concept of hybrid Ga₂O₃ nanomaterials is found to be attractive for contemporary applications in lithium-ion batteries, transparent conductive oxides, and photoluminescence.⁴³ In addition, some of the approaches open up new possibilities for cost-effective large-area green electronics, which are used for energy-harvesting devices. Doping other metals in Ga₂O₃ has proven to be quite useful in the design of electrodes for

enhanced photocatalytic activity.^{33-34,39} While these emerging applications are appealing and many methods of the chemical and physical synthesis of compounds are available, it is imperative to choose and optimize the processing conditions needed to reach the desired properties. Most importantly, a better understanding of the influence of thermochemical synthetic conditions, the fundamentals of associated chemical kinetics and crystal growth, and, finally, control over the phase and chemistry is quite important.

2.1 RESEARCH OBJECTIVES

The principal hypothesis that constitutes the background for this dissertation work is to establish a structure property correlation and performance evaluation of Fe doped gallium oxide ceramic material for optical and electrocatalytic applications. The main objective of this research work is, therefore, to design, fabricate, and set a basis for fundamental understanding of the effect of Fe doping into β -Ga₂O₃ specifically on its structure, properties and phenomena. The specific tasks and objectives pertinent to the undertaken research work are discussed below briefly.

2.1.1 Fabrication of Iron (Fe) Doped Ga₂O₃ Compounds

The primary objective of this research work is to fabricate high-quality intrinsic and Fe doped Ga₂O₃ bulk ceramic compounds employing solid state chemical reaction method. The goal is to investigate the structure property correlation of the fabricated compounds and their different properties for application in the field of optoelectronics and electrocatalysis. Inclusion of specific transition-metal ion in Ga₂O₃ is expected to show magnetic and magnetoelectronic properties, which might be useful for integration into other future applications.⁴⁴ Therefore, from a fundamental as well as an applied perspective, it is interesting and highly beneficial to derive a better understanding of the underlying science of the Fe doping into Ga₂O₃ to develop and design materials for industrial applications. The aforementioned properties and phenomena mainly

depend on the microstructural and interfacial chemistry, which, in turn, are sensitive to the processing conditions and associated chemical synthesis. Furthermore, the physical and chemical properties and preparation methods of nanosized powder particles are significantly different from the bulk materials.⁴⁵⁻⁴⁶ Also, optimization of the sintering process is of the utmost importance in order to achieve the best possible density and to obtain better chemical, physical, and electrical, properties of the oxides. It is beneficial to start the process with the smallest possible size particle because the higher surface energy associated with the small precursor particle will act as the driving force for the sintering process.⁴⁷⁻⁵⁰ However, unfortunately, there is no substantial literature available until now on the impact of the firing conditions for synthesizing GFO compounds. Therefore, the work presented here and specifically filling this fundamental knowledge gap in synthesizing such GFO compounds is expected to significantly contribute to the fundamental science of metal-doping effects in Ga₂O₃-based compounds.

2.1.2 Optimization of Synthesis Conditions

Optimizing the fabrication condition in order to achieve desired structure, morphology, electronic, optical, and catalytic properties, is of paramount importance. The impact of synthesis conditions such as proper mixing of the precursor powders with the binders, maintaining exact furnace temperature for calcination and sintering, duration of calcination and sintering, and partial pressure of the reactive gases inside the hot furnace atmosphere dictate the ultimate crystal structure, grain size, band gap, capacitance, resistivity, and related properties.

2.1.3 Establishing Structure-Property Correlation

Deriving a structure-property relationship is quite helpful in order to achieve an in-depth analysis of the transition metal doped Ga₂O₃ ceramic compounds for optical and electrocatalytic applications. The influence of synthesis parameters on the structure and property will be discussed

in detail. Special heed will be given towards the metal doping technique to introduce, modify and/or enhance the optical, and electrocatalytic properties as well as overall performance of these doped compounds. Furthermore, a comprehensive understanding of the structure-property relationship based on optimization of the calcination and sintering environments may provide a roadmap to the design and processing of Ga₂O₃ based materials for applications in catalysis, electronics, magneto-electronics, optoelectronics, energy storage, and conversion.

2.1.4. Evaluation of Practical Application Potential

Tuning the optical and optoelectronic properties of Ga₂O₃ has gained great attention due to their potential integration into several technological applications, which include solar blind photo detectors, photo-catalysis, luminescent phosphors, and photovoltaics. Ga₂O₃ valance band edge is found to be located at -7.75 eV vs vacuum, hence it can provide photo-generated charges with high oxidizing potentials which makes it useful for photocatalytic applications.³⁴ In fact, Ga₂O₃ has been reported to be an excellent water splitting photocatalyst for the generation of hydrogen. However, the main drawback associated with photocatalytic applications of Ga₂O₃ is its wide band gap (~ 5 eV), which limits their functionality due to UV-only absorption. Thus, despite its greatest potential, in a broader context, the photocatalytic applications of this material are considerably limited because it fails to generate sufficient electron-hole pairs upon solar light illumination. Different approaches have been adopted in order to enhance the photocatalytic activity of Ga₂O₃ based materials. Doping with suitable ions is one of the most popular methods, where the photocatalytic properties of β -Ga₂O₃ significantly altered by dopants.

During last few decades, hydrogen (H₂) has been advocated as a clean and sustainable source of energy and is considered as an ideal candidate to meet the future energy requirements. Among different techniques available, electrocatalytic water splitting is considered the most

economical and viable process. Electrocatalysts minimize the energy requirement for water splitting and, in this regard, platinum (Pt) shows the best result. But the high price and low abundance of Pt limit its extensive use. As an alternative, sulfides, phosphides and oxide-based materials have already been explored as an electrocatalyst. In the present work, for the first time, it is reported that the iron (Fe) doping facilitated selectivity across a wide spectral range and, specifically, the red-shifted optical band gap, and the electrocatalytic behavior of the transition metal doped Ga₂O₃ ceramics.

Chapter 3: Literature Review

3.1. GALLIUM OXIDE

Gallium oxide (Ga_2O_3) is a well-known transparent conductive oxide (TCO). Oxides of In, Zn, Sn, Cd, Cu, Mg metals also belong to this group.⁵¹ Lecoq de Boisbaudran⁵² discovered elemental gallium and its compounds in 1875. The early literatures have very few basic studies on Ga_2O_3 . Wide-band-gap oxides such as ZrO_2 , Y_2O_3 , HfO_2 , La_2O_3 , Ga_2O_3 , and GeO_2 have been the focus of much attention in recent years because of their wide range of technological applications in photocatalysis, chemical sensing, electronics, photonics, electro-optics, optoelectronics, and magnetoelectronics.⁵³⁻⁵⁷ Gallium oxide (Ga_2O_3), one among the wideband-gap oxides, has drawn the attention of the scientific and research community for its fascinating physical, chemical, and electronic properties, which can be readily utilized in numerous technological applications. Ga_2O_3 with a band gap (E_g) of ~ 5 eV is an ideal candidate for utilization in the fields of electronics,⁵⁸⁻⁵⁹ optoelectronics,^{36, 60} spintronics,^{44, 61} gas sensing,⁶²⁻⁶³ and ultraviolet photodetection.^{33, 64}

Ga_2O_3 exhibits several polymorphs; however, thermally stable β - Ga_2O_3 is the most popular for numerous industrial applications.³⁷ Intrinsic β - Ga_2O_3 is an insulating oxide. The electrical conductivity of Ga_2O_3 can, however, be tuned, and n-type semiconducting behavior can be realized by selective metal-ion doping. Ionization of the oxygen vacancies in Ga_2O_3 is the source of electrons, but the resulting conductivity of Ga_2O_3 upon doping is still not clear and a subject of much debate.³⁸⁻³⁹ On the other hand, intrinsic and doped Ga_2O_3 materials have been the subject of intense research in recent years because of their ability for the efficient use and tolerance of the hostile environments of high pressure and temperature (≥ 500 °C) in chemical sensing and catalysis.⁴⁰ Intrinsic and doped Ga_2O_3 materials have emerged as the most efficient sensing materials, particularly for oxygen sensing at higher temperatures.^{41, 62-63}

In view of fascinating properties and potential technological applications in diverse fields, Ga₂O₃ has been studied extensively. Several research groups have paid attention to tune their structural and physical properties by various means, such as elemental doping, adopting different processing methods, and fabricating thin films using different techniques.⁶⁵⁻⁶⁶ Specifically, in order to further improve the functionality and performance of Ga₂O₃, doping using either isovalent and/or multivalent ion(s) has been considered in the literature.⁶⁷ There are only a few theoretical/experimental studies which discuss about possible defects and effect of these defects on n-type conductivity of Ga₂O₃ upon doping of transition metals.

Effect on n-type conductivity by doping of transition metals such as W, Mo, Re, and Nb in Ga₂O₃ is discussed based on formation energies using first-principles calculations.⁶⁸ All these impurities or dopants can be incorporated at Ga sites in inequivalent crystallographic sites, with preferentially in octahedral sites. In contrast to Fe, Mo, and Re act as deep donors, whereas tetrahedral sites of W and Nb act as shallow donors with a difference in formation energies. Zn and Cu act as acceptors, these dopants increase hole concentrations in intrinsic Ga₂O₃.⁶⁹ It has been demonstrated that doping of Ga₂O₃ with tungsten (W) and titanium (Ti) provides enhanced ability to obtain tunable and controlled optical properties.⁷⁰⁻⁷¹ Additionally, Oleksak et al. have demonstrated that W-doped Ga₂O₃ thin films can form dense low-k dielectric materials, where the relative W content can significantly alter the dielectric constant.⁷² The Ga₂O₃ nanowires doped with Li or In shown enhanced luminescence for application in display devices.^{65, 73} The enhanced photocatalytic activity, which may be useful in a wide variety of energy-harvesting devices, has been reported for transition metal ion-doped Ga₂O₃ and Ga₂O₃ hybrid materials.⁶⁶

It is well known and evident that the nature and amount of foreign metal ions will dictate the resulting properties and phenomena of Ga₂O₃.⁶⁷ Therefore, it will be of great interest to study

the doping of isovalent/aliovalent ions at Ga sites in Ga₂O₃ crystal to investigate the effect of such metal ions on structural, physical, chemical, and electronic properties of the resulting materials. Specifically, from fundamental as well as applied perspective, it is highly beneficial to derive a better understanding of the underlying science of the transition metal ion doping into Ga₂O₃ to design materials for electrical and optical device applications. The Shannon ionic radii Ga and Fe closely match with each other; Ga³⁺ -0.62 Å (octahedral coordination), 0.47 Å (tetrahedral coordination) and Fe³⁺ -0.64 Å (octahedral coordination), 0.49 Å (tetrahedral coordination).⁷⁴⁻⁷⁵ It is reasonably assumed that Fe³⁺ can be substituted to Ga sites and can replace Ga³⁺ from both octahedral and tetrahedral positions in stoichiometric proportion. However, isovalent Fe³⁺ may induce some degree of structural disorder and lattice strain, which can significantly modify the electrical and dielectric properties in comparison to those of intrinsic β-Ga₂O₃. Also, the physical and chemical properties of the doped Ga₂O₃ are sensitive to the microstructure and chemistry, which in turn depends on the synthesis process and conditions employed.

3.1.1 Crystal Structure of Gallium Oxide

As mentioned before that Ga₂O₃ exhibits five different polymorphs such as α, β, γ, δ, and ε. Among these phases, thermodynamically, β-Ga₂O₃ is the most stable oxide.³⁷ The melting point of β-Ga₂O₃ is very high (1780 °C), which makes this material interesting and suitable for high-temperature electrochemical and electromechanical applications.^{66, 72, 76-77} β-Ga₂O₃ crystallizes in a base-centered monoclinic (space group C2/m) crystal structure (Figure 3.3), where O ions are in a distorted cubic packing arrangement and Ga³⁺ occupies distorted tetrahedral and octahedral sites.^{43, 73} The lattice parameters of β-Ga₂O₃ are a = 12.22 Å, b = 3.04 Å, c = 5.80 Å, and β = 103.83°. ^{69, 78-79} Heating GaO(OH) in the air between 450 and 550 °C can synthesize all of these polymorphs as depicted in the Figure 3.1.

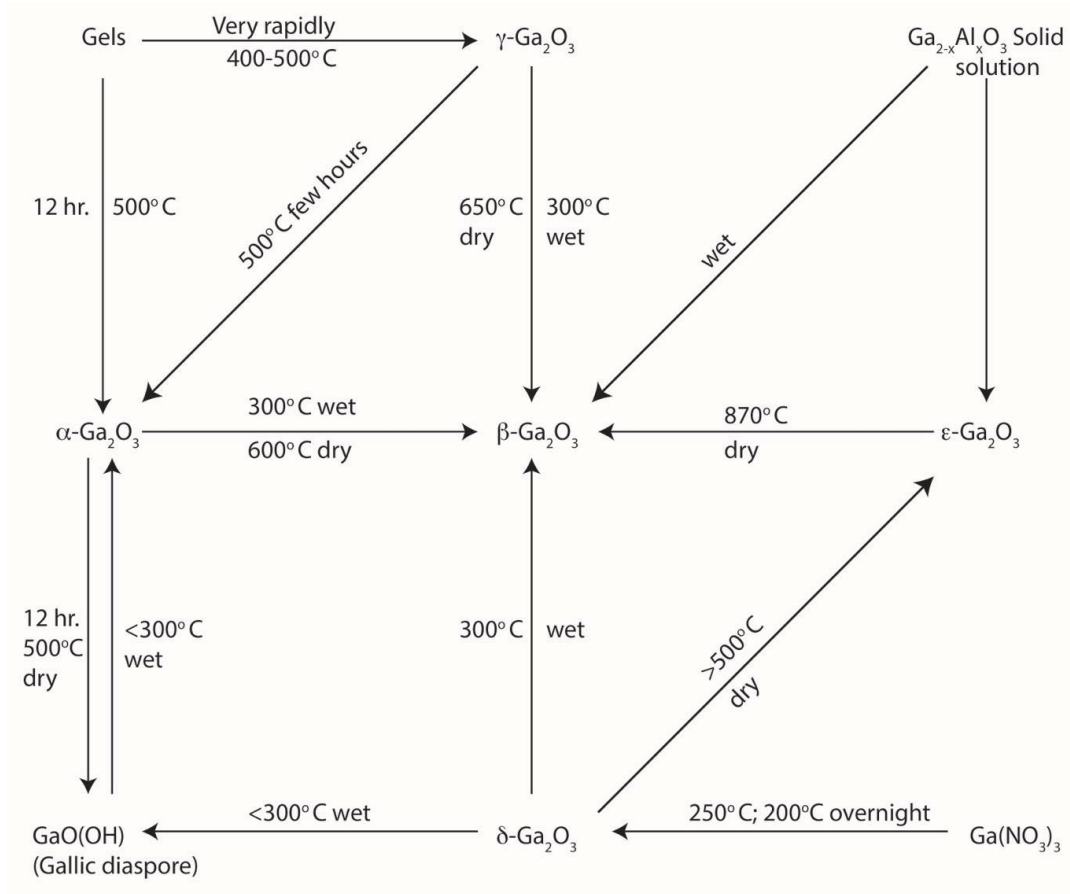


Figure 3.1: Synthesizing route of Ga₂O₃ polymorphs.

α-Ga₂O₃

Both α -Ga₂O₃ and corundum (Al₂O₃) have similar crystal structure (i.e. rhombohedral structure) as both originate from the same group in the periodic table (Group IIIA).⁸⁰⁻⁸¹ The associated space group with this structure is $R\bar{3}c$. The lattice parameters which were calculated experimentally, are $a = 4.98 \text{ \AA}$ and $c = 13.43 \text{ \AA}$.⁸² The crystal structure of α -Ga₂O₃ is depicted in Figure 3.2. Corundum substrate can be used to grow heteroepitaxial thin film of α -Ga₂O₃ as both have the similar crystal symmetry. The inter-ionic distance (between two Ga³⁺) in α -Ga₂O₃ are substantially shorter than in the case of β -phase.⁸³ In α -Ga₂O₃, gallium ions sit in the octahedral sites (two-third occupancy of the total sites) whereas the oxygen ions are configured in hexagonal close packed structure. He et al.⁸⁴ calculated the theoretical band gap of α -Ga₂O₃. α -Ga₂O₃

registered comparatively higher refractive index as well as the reflectance in comparison to the β phase but, the effective mass of electrons is higher for the later. α - Ga_2O_3 is a potential candidate for photocatalytic application as it has the highest band gap among all the polymorphs. Ultrasonic mist chemical vapor deposition (USCVD) technique is the most common route for synthesizing α - Ga_2O_3 as this key technology is a safe and simple, as well as economic and environmentally friendly.^{81, 85}

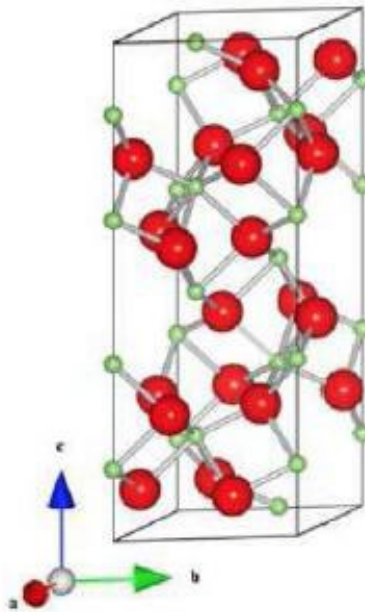


Figure 3.2: Crystal structure of α - Ga_2O_3 .

β - Ga_2O_3

β - Ga_2O_3 is the most studied and stable phase (until its melting point 1900 °C) amongst all Ga_2O_3 polymorphs. Other polymorphs of Ga_2O_3 are metastable and eventually transform to β - Ga_2O_3 if heat treated above 800 °C.⁸⁶ β - Ga_2O_3 has versatile application area. β - Ga_2O_3 crystallizes in monoclinic crystal symmetry having $C2/m$ space group which is shown in Figure 3.3. The standard lattice parameter values obtained from the experimental calculations are $a= 12.23 \text{ \AA}$, $b= 3.04 \text{ \AA}$, $c= 5.80 \text{ \AA}$ and $\beta= 103.7^\circ$.^{83, 87} Ga ions in β - Ga_2O_3 coordinated themselves in both

tetrahedral and octahedral sites unlike $\alpha\text{-Ga}_2\text{O}_3$ where Ga^{3+} are only octahedrally coordinated. It is important to mention that change in coordination geometry in the lattice in general has significant impacts on structural and physical properties and as a result it affects the coveted application areas.

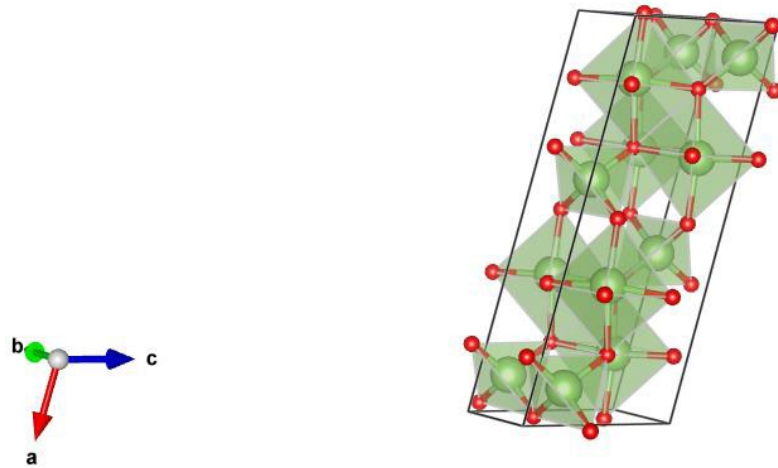


Figure 3.3: Crystal structure of $\beta\text{-Ga}_2\text{O}_3$.

$\beta\text{-Ga}_2\text{O}_3$ is a poor thermal conductor because of crystalline anisotropy and the very same reason is responsible for orientation specific thermal conductivity of $\beta\text{-Ga}_2\text{O}_3$; [010] direction registered the highest thermal conductivity, whereas lowest thermal conductivity was recorded along [100] direction at all temperatures.⁸⁸ $\beta\text{-Ga}_2\text{O}_3$ is well-suited for application as a transparent conducting oxide throughout the ultraviolet (UV) spectrum region.⁸⁹⁻⁹⁰ $\beta\text{-Ga}_2\text{O}_3$ has a direct band gap of ~ 4.9 eV as well as high theoretical breakdown electric field (~ 8 MV/cm).⁹¹⁻⁹² These features are paving the way for $\beta\text{-Ga}_2\text{O}_3$ as a potential candidate for high power electronics.⁹²

$\gamma\text{-Ga}_2\text{O}_3$

$\gamma\text{-Ga}_2\text{O}_3$ is the less known polymorph amongst all which is why it is not very common in research community owing to its poor crystalline nature. It crystallizes in defective cubic spinel-type structure (MgAl_2O_4 type or simply AB_2O_4) with $Fd\bar{3}m$ space group having lattice parameter of a cubic structure ($a = 8.23$ Å).⁹³ Figure 3.4 shows the equivalent crystallographic configuration

of $\gamma\text{-Ga}_2\text{O}_3$ by depicting MgAl_2O_4 crystal structure. By introducing Ga-ion defects in primitive cells employing first principle calculations, it has been proven that 14 inequivalent crystallographic configurations are possible. The primitive cells consisted of 6 tetrahedral cationic sites, 12 octahedral cationic sites, and 24 oxygen sites.⁹⁴ There was no clear preference set for the defect location whether the introduced Ga^{3+} will sit in tetrahedral or octahedral sites.⁹⁴

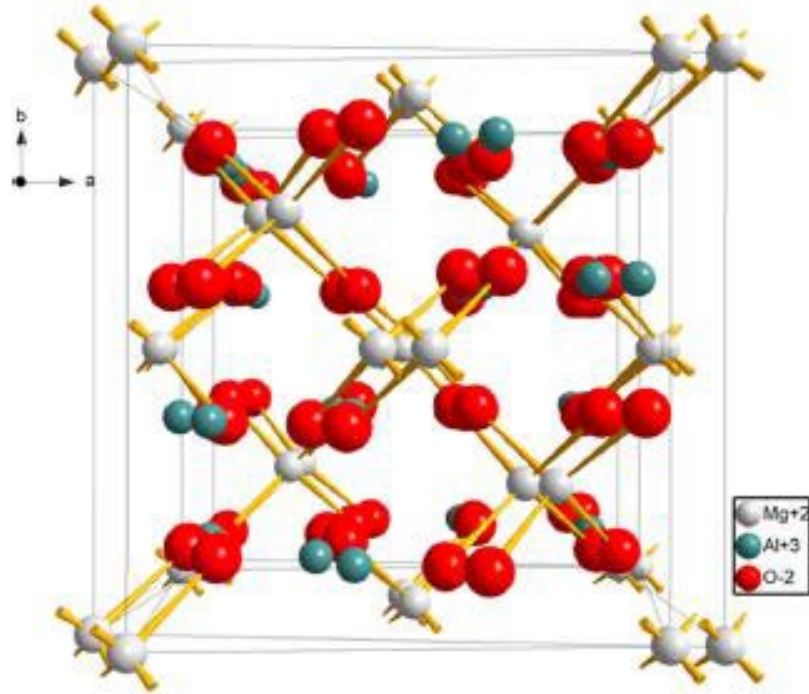


Figure 3.4: Crystal structure of $\gamma\text{-Ga}_2\text{O}_3$ which is represented by an equivalent crystal structure of MgAl_2O_4 .

$\delta\text{-Ga}_2\text{O}_3$

$\delta\text{-Ga}_2\text{O}_3$ has body-centered cubic crystal structure with $Ia\bar{3}$ space group.⁹⁵ Roy et al.⁹⁵ being the first to synthesize $\delta\text{-Ga}_2\text{O}_3$, brought Infront of the research community in the year of 1952. The lattice parameter of $\delta\text{-Ga}_2\text{O}_3$ mentioned by Roy et al. was $a= 10.0 \text{ \AA}$.⁹⁵ The $\delta\text{-Ga}_2\text{O}_3$ crystal structure which is quite similar to bixbyite crystal structure such as In_2O_3 and Mn_2O_3 is depicted in Figure 3.5 by an analogous crystal symmetry.⁴³

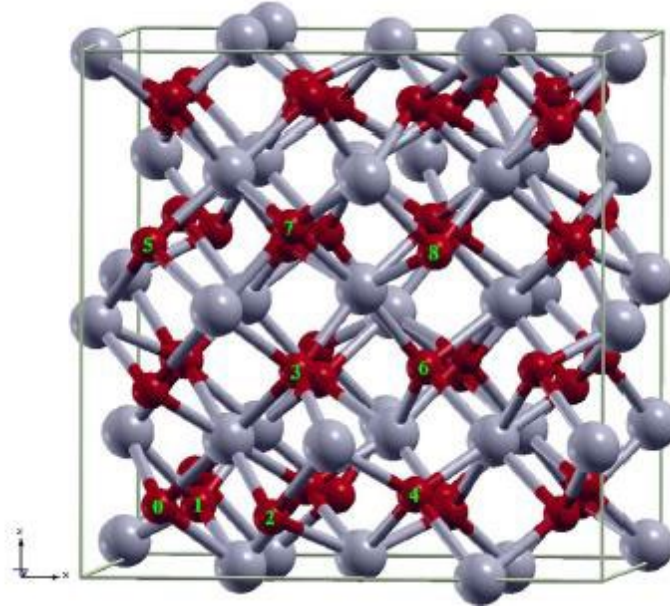


Figure 3.5: Crystal Structure of δ -Ga₂O₃ represented by an analogous crystal structure of In₂O₃.

ϵ -Ga₂O₃

The crystal structure of ϵ -Ga₂O₃ is not well established among the research community. It was reported that ϵ -Ga₂O₃ can be synthesized from δ -Ga₂O₃ when δ -Ga₂O₃ is heated above 500 °C.⁹⁵ ϵ -Ga₂O₃ crystal structure can be synthesized from Sn-doped highly conductive Ga₂O₃ films synthesized via pulsed laser deposition (PLD) route at a temperature above 475 °C. which was taken granted for ϵ -Ga₂O₃ but raised suspicion.⁹⁶ Considering the aforementioned condition, ϵ -Ga₂O₃ crystallizes in orthorhombic crystal symmetry with *Pna*21 space group. The lattice parameters calculated for ϵ -Ga₂O₃ has $a= 5.12$ Å, $b= 8.79$ Å, and $c= 9.41$ Å.⁹⁷ Figure 3.6 represents an analogous crystal structure of ϵ -Ga₂O₃ by depicting AlFeO₃ crystal structure.

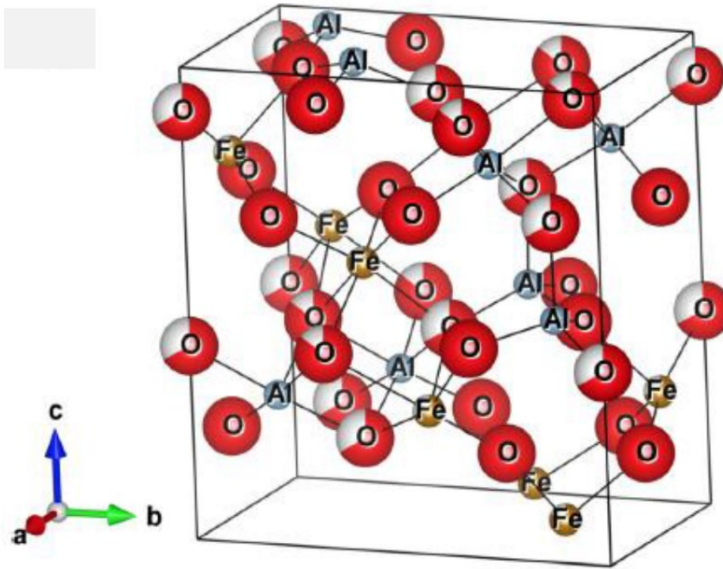


Figure 3.6: ϵ - Ga_2O_3 represented by an equivalent crystal structure of AlFeO_3 .

3.1.2 Gallium Oxide Crystal Growth and Hybrid Oxide Synthesis Techniques

Ga_2O_3 bulk crystals can be synthesized by melt growth techniques, whereas solid-state chemical synthesis processing can be employed to obtain doped compounds of Ga_2O_3 (i.e., hybrid oxides).

Melt Growth

As a viable technology melt growth is a very common among different crystal growth techniques in order to produce single crystals of any material. Considering the growth rate, scalability, and crystal quality, melt growth is the most suitable method to grow Ga_2O_3 crystals.⁴³ In an oxidizing environment, Ga_2O_3 melts completely at a temperature above 1820 °C; but when it is heated in an oxygen deficient atmosphere, Ga_2O_3 decomposes to form lower volatile oxides.⁴³

Various melt growth techniques used to grow Ga_2O_3 crystals, are listed below:

- Verneuil Method
- Floating Zone (FZ) Method
- Czochralski (CZ) Method

- Edge-defined Film-fed Growth (EFG) Method
- Vertical Bridgman Method

Solid-State Synthesis Method

The solid-state synthesis method or solid-state reaction route is widely considered for the preparation of polycrystalline solids. The precursors used in this technique should be solid materials. This is basically a high temperature (at temperatures above 1000 °C) synthesis route as solid materials do not react at room temperature given sufficient time due to high activation energy required for the reaction kinetics. The feasibility and reaction rate is determined by many factors such as structural properties of the precursor materials, reaction conditions, reactivity of the raw materials, surface area of the solids, and the thermodynamic free energy change associated with the reaction, etc.⁹⁸ The experimental procedure mainly has two steps namely, mixing of the reagents and the heat treatment.

3.1.3 Application of β -Ga₂O₃

Electrocatalytic Properties of β -Ga₂O₃

Since decades, platinum is used in the fuel cell as an electrode material; but an ongoing search for a cost-effective as well as efficient electrode material for fuel cell that can replace platinum, has become the center of interest for unconventional energy source-based power systems. Transition/post-transition metal oxide-based catalysts are tried so far in this context for the efficient conversion of energy, mainly oxygen reduction reaction (ORR), oxygen evolution reaction (OER), and hydrogen evolution reaction (HER). It is reported somewhere that electrospun β -Ga₂O₃ nanofibers which is a post-transition metal oxide, is an efficient bifunctional catalyst material. Ion transport is mainly facilitated by the highly porous architecture of these spongy nanofibers. This new catalyst registered similar efficiency like the Pt/C catalyst. The ORR onset

potential for this β - Ga_2O_3 nanofibers catalyst was 0.84 V (vs RHE) and for HER, the onset potential was -0.34 V (vs RHE); but the current density was clearly superior to the Pt/C catalyst. This salient feature is a result of unique morphology associated with large surface area and without doping. Generally, doping induces many defects in a near perfect structure which helps to increase the ionic transport which is mainly responsible for this performance.

3.2 IRON(III) OXIDE

Iron(III) oxide also known as ferric oxide (Fe_2O_3) is an inorganic compound. It can be obtained from hematite mineral following extractive metallurgical routes. Fe_2O_3 is one of the three oxides of iron. The other two oxides are iron(II) oxide (i.e., FeO) and iron(II,III) oxide (i.e., Fe_3O_4) which can be found in magnetite mineral. FeO is the rarest oxide among three. Iron(III) oxide mainly has two polymorphs namely, α - Fe_2O_3 and γ - Fe_2O_3 . While α -phase has rhombohedral corundum structure, γ -phase has cubic crystal symmetry. The magnetic properties of α -phase can be influenced by several factors, among them particle size is significant. γ -phase is metastable and converted to α -phase if it is heated at high temperature. γ - Fe_2O_3 is ferromagnetic, however ultrafine particles (>10 nm) of γ - Fe_2O_3 is superparamagnetic. α - Fe_2O_3 finds application in photoanode for solar water oxidation; iron(III) oxide is also used in magnetic recordings and for medicinal purposes.⁹⁹ Figure 3.7 shows a crystal structure of hematite unit cell.

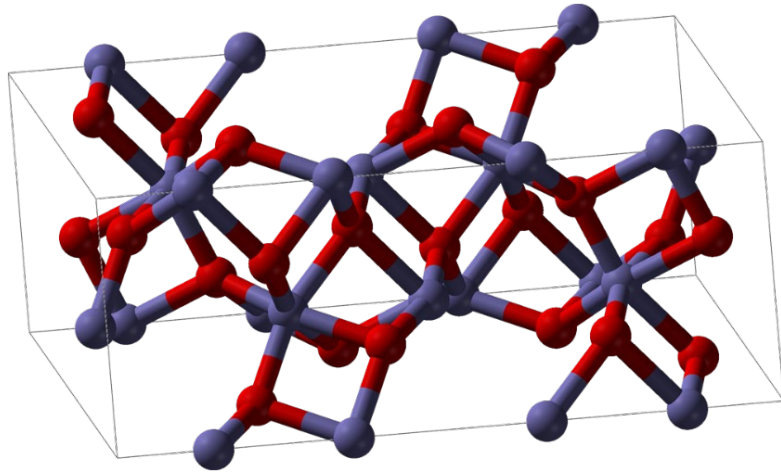


Figure 3.7: Crystal structure of hematite unit cell.

Chapter 4: Materials and Methods

4.1 MATERIALS

The precursor materials such as Ga_2O_3 and Fe_2O_3 were procured from Sigma Aldrich and Noah Technologies Corporation, respectively. The purity of Ga_2O_3 was $\geq 99.99\%$ trace metals basis and that of Fe_2O_3 was 99.9% pure and particle size < 3 microns average.

4.2 SYNTHESIS TECHNIQUE

$\text{Ga}_{2-x}\text{Fe}_x\text{O}_3$ (GFO, $0.00 \leq x \leq 0.30$) compounds were synthesized from high pure precursor materials (i.e., Ga_2O_3 and Fe_2O_3) through a conventional solid-state chemical reaction route. In order to obtain phase pure GFO compounds, initially the precursor materials were weighed in stoichiometric proportion in accordance with specific concentration. The stoichiometrically weighed powders were ground in an agate mortar to obtain homogeneously mixed compound using ethanol as a wetting media and polyvinyl alcohol (PVA) as a binder. In order to obtain single phase GFO compounds calcination of homogeneously mixed powders were done in a muffle furnace at 1100°C for 6 h with a ramp rate of $10^\circ\text{C}/\text{min}$ (both heating and cooling). The calcined powders were again ground to reach ultrafine particles with narrow particle size distribution, which helps to improve the sintered density of the green pellets. Uniaxial hydraulic press was used to prepare circular green pellets of about 8 mm diameter and 1 mm thickness by applying 5 ton load for 4-5 minutes. The as-prepared pellets were sintered at 1200°C for 6 h in the same muffle furnace to fabricate final pellets with superior density.

However prior to above, in order to optimize the structural properties, the GFO compounds were synthesized for a particular concentration ($x=0.10$) by varying the calcination and sintering temperature while keeping the calcination and sintering time constant for 6 h. Calcination was

performed at different temperatures ranging from 800 to 1100 °C; after that, the green pellets were sintered in the same furnace at different temperatures, $T_{sint} = 900\text{--}1200$ °C.

4.3 EXPERIMENTAL METHODS

Different analytical tools and techniques have been employed in order to characterize the physical and chemical properties of Fe-doped Ga₂O₃ (GFO) compounds such as X-ray Diffraction (XRD), X-ray Photoelectron Spectroscopy (XPS), UV-Vis Spectroscopy, Scanning Electron Microscopy associated with Energy-dispersive X-ray spectrometry (SEM-EDS), X-ray Absorption Near Edge Structure (XANES), Raman Spectroscopy and electrochemical analysis. These techniques helped us to characterize the synthesized compounds in order to achieve optimized properties for their intended applications in required fields and also allowed us to draw a behavioral map of the doped compounds which was needed to achieve the research goal.

4.3.1 Crystal Structure and Surface Morphology

X-ray Diffraction (XRD)

In traditional XRD, a monochromatic X-ray is emitted and directed towards the sample (placed on a sample holder) surface. As a result, atoms from the sample's surface and inner crystal planes cause the X-ray to diffract. The resulting scattered X-ray then undergoes either constructive or destructive interferences based on the crystal structure and plane orientations. A detector collects the diffracted X-ray at various angles obviously satisfying the Bragg's law which is shown below to identify the crystal unit cell.

$$n\lambda=2d\sin\theta \quad (\text{Eq. 4.1})$$

where, n is an integer, λ is the wavelength of X-ray, d is the interplanar spacing and θ is the Bragg's angle. Figure 4.1 depicts the graphic representation of X-ray interacting with a crystalline material.

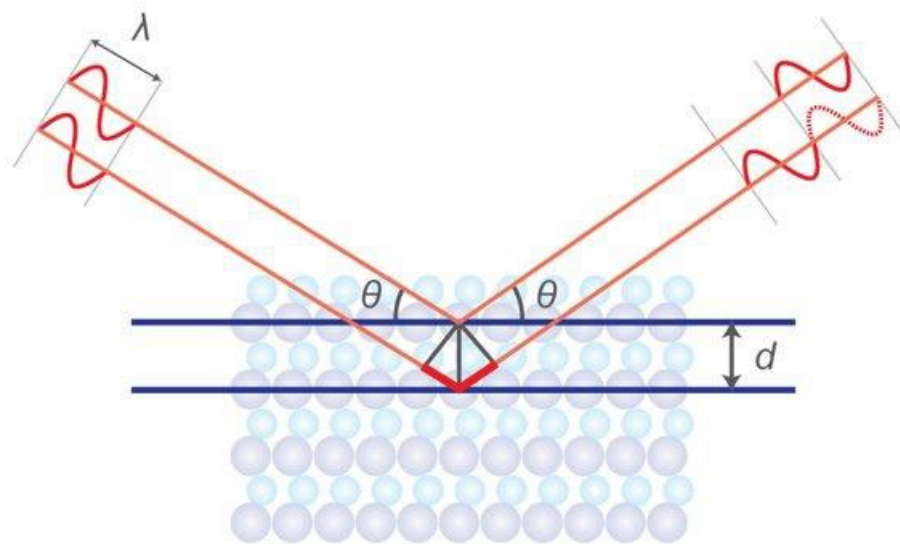


Figure 4.1: Schematic diagram of X-ray interacting with a crystalline material.

The phase purity and crystal structure of synthesized GFO compounds were studied using a Bruker D8 Discover X-ray diffractometer (Source: Cu K_{α} , $\lambda = 1.5406 \text{ \AA}$). The lattice constants (a, b, c), unit cell volume (V) and theoretical density (ρ_{th}) were calculated from the X-ray diffraction (XRD) data. The effective density (ρ_{eff}) was measured employing Archimedes' principle (ASTM B962) and relative porosity was determined using both ρ_{th} and ρ_{eff} . The magnitude of error while calculating the lattice constants is about 0.0004 \AA which is negligible. The following equations (eq. 4.2–4.5) are employed for cell parameters, unit cell volume, and density calculations:

$$1/d^2 = 1/\sin^2\beta (h^2/a^2 + k^2\sin^2\beta/b^2 + l^2/c^2 - 2hl\cos\beta/ac) \quad (\text{Eq. 4.2})$$

$$V = abc\sin\beta \quad (\text{Eq. 4.3})$$

$$\rho_{th} = nM/NV \quad (\text{Eq. 4.4})$$

$$\text{Relative Porosity} = [(\rho_{th} - \rho_{eff})/\rho_{th}]100\% \quad (\text{Eq. 4.5})$$

where, M is the molecular weight, N is the Avogadro number, n is the number of atoms per unit cell (here, $n = 2$), and V is the unit cell volume.

Rigaku Benchtop powder X-ray diffractometer (Mini Flex II) was used to reconfirm the phase purity and the crystal structure of synthesized GFO compounds employing Rietveld refinement. Scanning parameters were: $10^\circ - 80^\circ$ (2θ range), step size – 0.02° and Scan rate – $0.6^\circ/\text{min}$. Structural refinement of selected compositions was carried out using full proof software package.¹⁰⁰

Scanning Electron Microscope (SEM)

SEM employs a very focused beam of electrons to reveal the surface morphology of the specimen. The high energy electrons which are emitted from an electron gun, directly focused on the sample by some magnetic lens arrangements in order to scan the surface. Generally, images are generated by a rastering process. SEM can furnish detailed images of the specimens at different magnifications. Best resolution of the sample images can be obtained by varying the electron incident current and voltage. The acquired images were analyzed using the Image J software package,¹⁰¹ which allows us to measure the individual grain size of the specimen almost accurately. Surface morphology of the GFO samples was studied using a Hitachi S-4800 field emission scanning electron microscope (SEM) operating in secondary electron imaging mode at an applied source voltage of 20 kV. Prior to imaging, samples were coated with gold to make the surface conductive and avoid the charging effect. Secondary electron mode was used throughout the sample study as this mode is beneficial for inspecting the surface topography. Figure 4.2 depicts the working mechanism of a SEM.

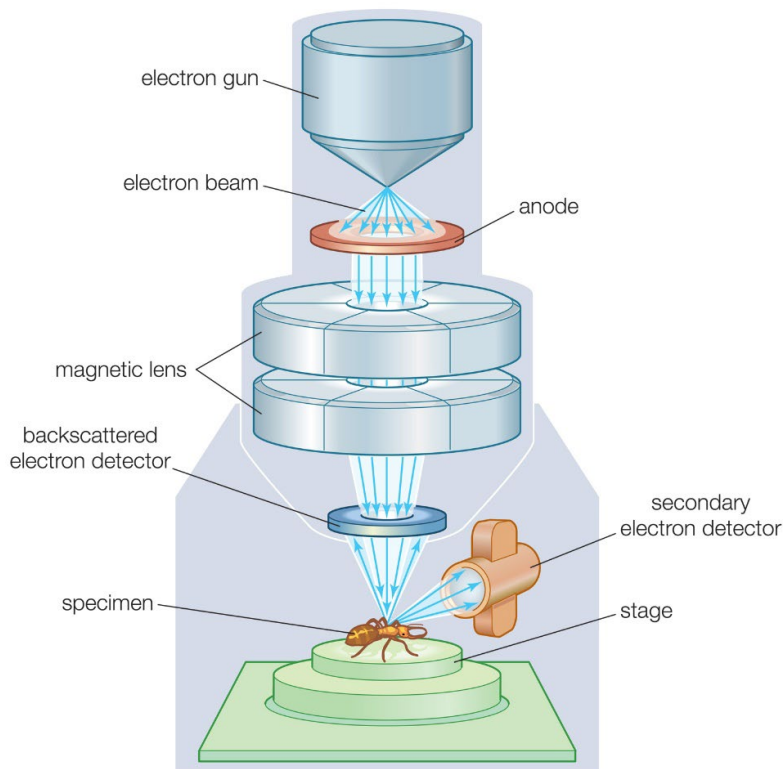


Figure 4.2: SEM working mechanism.

4.3.2 Chemical Analysis

Energy-Dispersive X-ray Spectrometry (EDS)

Energy-dispersive X-ray spectroscopy (EDS), also known as energy dispersive X-ray analysis (EDXA) or energy dispersive X-ray microanalysis (EDXMA), is an analytical technique which is typically used for the chemical characterization or elemental analysis of a sample. It basically depends on an interaction between a source of X-ray excitation and a sample. The characterization technique can be explained by considering a fundamental concept that each element has a distinctive atomic structure which allows a unique set of peaks on its electromagnetic emission spectrum. The principle of EDS is depicted in Figure 4.3. The EDS spectra were collected to confirm the stoichiometry of synthesized compounds. In addition, elemental mapping was carried out for the samples to observe the constituent elemental

distribution. The samples for SEM and EDS analyses were prepared by attaching the GFO pellets on carbon tape, which was pasted on an aluminum grid for better connectivity.

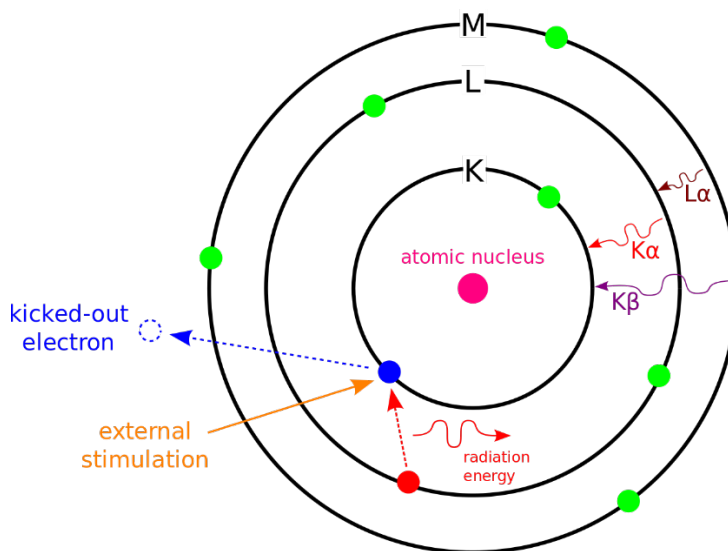


Figure 4.3: Principle of EDS.

X-ray Photoelectron Spectroscopy (XPS)

XPS is a highly surface sensitive technique generally employed to evaluate the surface chemistry of a sample. This technique quantifies the chemical data of the substrate surface using inelastic X-ray scattering phenomena. The high energy X-ray interacts with the surface atoms of the sample, which results in electron emission. This phenomenon is known as the photoelectric effect. The kinetic energy of the emitted electron is measured following the equation mentioned below:

$$KE = h\nu - BE - \Phi \quad (\text{Eq. 4.6})$$

where, KE is the kinetic energy of the electrons, h is Planck's constant, ν is frequency, BE is binding energy and Φ is the spectrometer work function. However, if the photon energy is less than the work function, there will be no emission of electrons from the orbitals. The kinetic energy of these emitted electrons is equivalent to the difference between the incident photon energy and binding energy of the electron, so the kinetic energy can be used to ascertain the concentration of

the constituent elements on the sample surface, as each element possess a unique set of core level electron configuration. XPS can also indicate the chemical state of a particular element in the sample by recording the variations in elemental binding energy or chemical shift(s). Figure 4.4 shows the basic functioning of an XPS system.¹⁰²

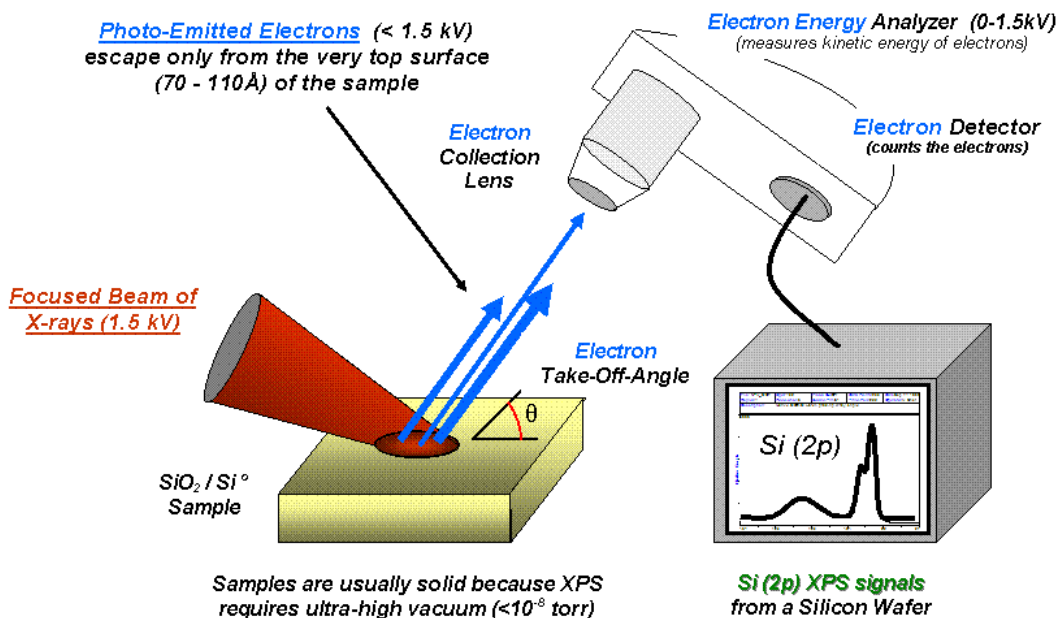


Figure 4.4: Basic functioning of an XPS system.

X-ray photoelectron spectroscopy (XPS) spectra of GFO compounds were collected employing Kratos Axis Ultra DLD spectrometer using high-performance Al K_α monochromatic X-ray source (1486.6 eV) and a high-resolution hemispherical analyzer. The X-ray source was set at 150 W. Emitted photoelectrons were collected using detector which is aligned normally to the sample surface. Data were collected in a 700 × 300 μm² area with a pass energy of 40 eV, which produced a full width half-maxima (FWHM) of 0.59 eV for the Ag 3d_{5/2} core level of a standard Ag sample. Charge neutralization was obtained with low-energy electrons (< 3.8 eV) as these ceramic pellets are highly insulating. The pellets were placed on the XPS stubs with the help of

double-sided Cu tapes and the same Cu tape, connecting the sample surface and the Cu stubs, was used in order to reduce and/or eliminate the charging issues. Data were analyzed by employing CasaXPS software using Gaussian/Lorentzian (GL(30)) line shape and Shirley background correction.¹⁰³⁻¹⁰⁴ The binding energy of carbon (C 1s) at 284.8 eV was used as the charge reference. Survey scans were performed at pass energy of 160 eV, while high-resolution scans were carried out at a pass energy of 40 eV. Survey scans were collected over the binding energy (B.E.) range of 0-1400- (-)5 eV. The step size for the survey and high-resolution scans were 0.5 and 0.1 eV, respectively. Though both Ga2p and Ga 3d spectra were collected but, Ga 2p spectra is presented in order to avoid the interference of Ga 3d peaks with the O 2s peak. Ultra-high vacuum level in the range of 1×10^{-9} Torr was maintained throughout the tests. Precaution has been taken in order to minimize the effect of adventitious carbon adsorption on the sample surface during sample transfer. Estimation error was taken ± 0.01 at.% for calculating the concentration of various constituent elements, i.e., Ga, Fe and O. Three different areas were scanned for each sample to maintain good statistical index.

X-ray Absorption Near-Edge Structure (XANES)

X-ray absorption near edge structure (XANES) which is also known as near edge X-ray absorption fine structure (NEXAFS), is a typical absorption spectroscopy. This characterization technique which is a complementary technique to XPS, is generally used to study the features in the X-ray absorption spectra (XAS) of condensed matter. Photo-absorption cross section for electronic transitions from an atomic core level to final states triggers the resulting spectra. The energy range for this technique is between 50–100 eV above the selected atomic core level ionization energy. It is important to mention here that the interatomic distance between the absorbing atom and its first neighbour atoms is smaller than the wavelength of the photoelectron.

Figure 4.5 depicts the fundamental mechanism associated with XANES. XANES is more efficient in determining the changes at local geometries and electronic structure of compounds. XANES is a very sensitive technique, which can determine changes in coordination geometry and oxidation states of constituent elements of the complex chemical compounds.¹⁰⁵⁻¹⁰⁶

The XANES spectra of sintered GFO powders were collected at beamline 6.3.1.2 of the advanced light source (ALS) at Lawrence Berkeley National Laboratory (LBNL) in total electron yield mode (TEY). To collect the patterns, the specimen powders were pressed into In foil and fixed onto a Cu sample pack using adhesive carbon tape. The analysis chamber pressure was maintained below 1×10^{-9} Torr during the measurements. Calibration standards were furnished by ALS mounted within the X-ray absorption spectroscopy instrument chamber for accurate measurement of the energy positions. Ga L-edge, O K-edge, and Fe L-edge were recorded for all the GFO samples. Reference Ga L-edge, Fe L-edge, and O K-edge spectra were also collected from high purity (>99.9%) Ga_2O_3 and Fe_2O_3 standard powder samples for calibration.

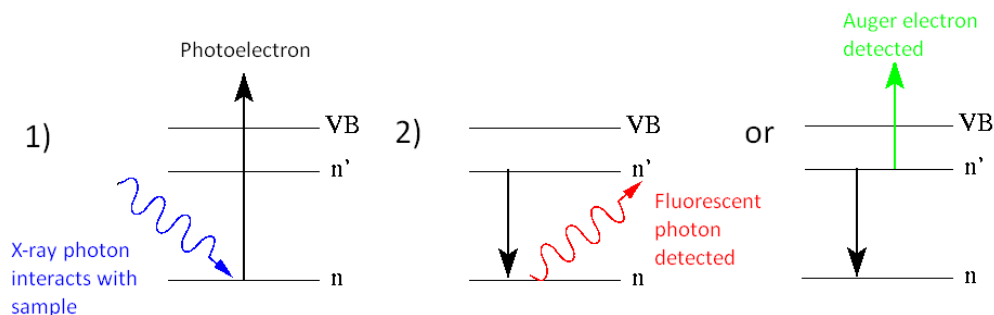


Figure 4.5: Fundamental working principle of XANES.

Raman Spectroscopy

Raman spectroscopy which is named after famous Indian physicist C.V. Raman is mainly used to study the vibrational modes of molecules. Raman spectroscopy is generally used to get information on structural fingerprint by which a molecule can be identified. It depends on inelastic

scattering of photons which is known as Raman scattering. A laser source (either of visible, near infrared, or near ultraviolet range) is used to generate monochromatic light. The resulting laser light interacts with the sample molecular vibrations, phonons or other excitations present in the system and as a result the laser photon energy shifts up or down. This deviation of the laser photon energy provides information about the different vibrational modes in the system. Infrared spectroscopy serves as a complementary technique to Raman spectroscopy.¹⁰⁷ Figure 4.6 is the graphical representation of a typical setup for a dispersive Raman spectroscopy. Raman spectroscopic studies were performed on an InVia Micro RAMAN (Renishaw) spectrophotometer with 532 nm laser excitation.

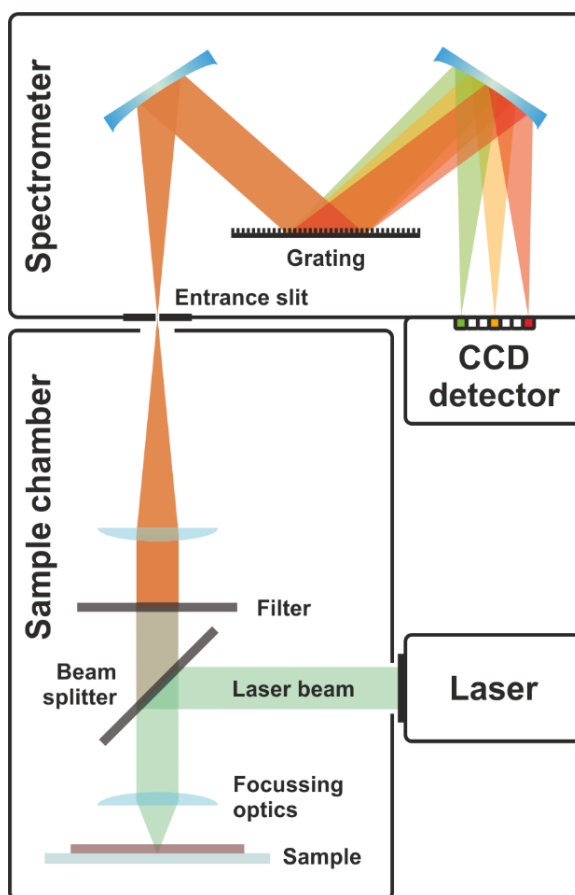


Figure 4.6: Raman spectroscopy setup.

4.3.3 Dielectric Properties

Dielectric measurements were performed using a HP precision LCR meter. LCR meter which is a typical electronic test equipment, is generally used to measure the capacitance (C), inductance (L) and resistance (R) of an electronic item. Simpler versions of this instrument involves the measurement of impedance which is then converted to the corresponding capacitance or inductance value in monitor display. Reasonably accurate readings can be yielded if the capacitor or inductor component under examination does not show up significant resistance. More advanced designs available in the market can be able to measure true inductance or capacitance. This instrument is also equipped to measure the equivalent series resistance of capacitors and the Q factor of inductive components.

Prior to the measurements, samples were fine polished and coated with silver paste on both sides. Silver-coated pellets were cured at 90 °C for 2 h to make sure the proper functioning of the electrodes. For all the samples, capacitance and dielectric dissipation ($\tan \delta$) data were collected to calculate the real (ϵ') and imaginary (ϵ'') parts of the dielectric constant. Data are collected in the frequency range of 90 Hz to 1 MHz at 1 V input ac signal amplitude at room temperature. High temperature measurements were performed at 1 KHz, 10 KHz, 100 KHz, and 1 MHz, respectively, employing a temperature-controlled furnace. The temperature was varied from 30 to 500 °C. Standard calibration and precautions were taken to remove any stray capacitance and contact resistance before each measurement. The experiments were performed in a repetitive manner in order to take statistical errors into consideration.

4.3.4 Spectral Selectivity - Optical Absorption

Optical absorption edge of the synthesized GFO compounds were studied using Ultraviolet–visible spectroscopy or ultraviolet–visible spectrophotometry (UV–Vis or UV/Vis).

This indicates absorption spectroscopy or reflectance spectroscopy involving the ultraviolet (partly) and the adjacent visible (full) spectral regions. The absorption or reflectance in the visible range has a direct impact on the perceived color of the chemicals involved. Atoms and molecules undergo electronic transitions when illuminated in this electromagnetic spectrum region. Absorption spectroscopy is a complementary characterization technique to fluorescence spectroscopy. While, absorption spectroscopy deals with transitions from the ground state to the excited state, fluorescence spectroscopy indicates transitions from the excited state to the ground state.

Optical absorption edge is associated with charge transfer from valance band to conduction band, which originally depends on overall electronic band structure of a particular compound. Though X-ray diffraction analysis showed the evidence for elemental substitution in parent phase, however optical absorption spectra can provide deeper insights into elemental substitution in the same. Hence, we have collected absorption spectra of GFO compounds using UV-Vis spectrophotometer (PerkinElmer, Model: Lambda 1050). Sintered GFO pellets were used for these measurements.

4.3.5 Electrocatalytic Activity Studies

A potentiostat was used to get a deeper insight into the electrocatalytic activity of the selected GFO compounds. A potentiostat is an electronic hardware with a three electrode cell setup and mostly employed to run electroanalytical experiments. The working principle of a potentiostat is that the potential of the working electrode is kept constant with respect to the reference electrode by tuning the current at an auxiliary electrode. A simplified electrical circuit which is described in terms of simple op amps, is depicted in Figure 4.7.

To evaluate the effect of doping on the electrocatalytic activity of the doped and undoped samples, their activity towards the Hydrogen Evolution Reaction (HER) was analyzed. In order to do this, a three-electrode system where the sample is the working electrode, Ag/AgCl the reference electrode and platinum as the counter electrode was formulated in presence of 0.5 M H₂SO₄ aq. electrolyte. The preparation of the working electrode was done by mixing the bulk powder samples with 80 μ L of 5 wt% Nafion 117 solution (Sigma-Aldrich) and drop-casting 20 μ L of the completely mixed solution onto a freshly polished glassy carbon working electrode. Subsequently, the redox properties were studied using a linear sweep voltammetry (CHI 6273E potentiostat) with scan rate of 20 mV s⁻¹ over a voltage range of 0 to -1.3 V.

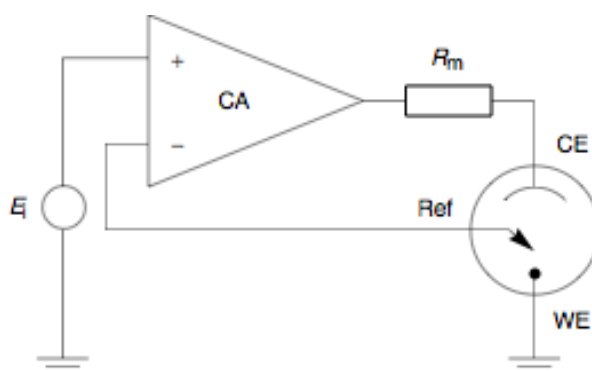


Figure 4.7: Potentiostat electric circuit diagram.

Chapter 5: Effect of Sintering Temperature-Optimization of Synthesis Conditions

5.1 CRYSTAL STRUCTURE AND SURFACE MORPHOLOGY

The XRD patterns of the GFO compounds sintered under variable processing temperature for constant amount of Fe doping concentration (i.e., $x = 0.10$) are shown in Figure 5.1. The peaks are indexed using JCPDS 00-041-1103 for β -Ga₂O₃.¹⁰⁸ The data shown are for GFO samples sintered at variable T_{sint} . The XRD data and peak assignment (Figure 5.1) clearly indicate that GFO crystallizes in a monoclinic β phase. It is evident from the XRD data that there is no secondary phase formation at all T_{sint} values. It can be noted that the peak intensity increases with increasing T_{sint} . In addition, although not significant, a slight positive shift of the peak position with increasing T_{sint} can be noted. The first observation, i.e., a peak intensity increases with increasing T_{sint} , indicates enhanced crystallinity of the GFO materials. Peak shifting can occur only when stress is introduced into the crystal structures of the GFO compounds. Therefore, the slight positive peak shift with increasing T_{sint} indicates a reduction in the interplanar distance between the crystal planes. This, in turn, induces some amount of strain in the crystal, which may be due to Fe doping or excess thermal energy. Furthermore, the XRD data indicate that doped Fe might preferentially occupy the substitutional atomic positions within Ga₂O₃ because no extra peak is observed due to Fe doping.⁷⁴ However, this is only a speculation based on the XRD observations and also considering the ionic radius difference in the Ga³⁺ and Fe³⁺ ions. The ionic radius of Ga³⁺ is 0.62 Å, and that of Fe³⁺ is 0.64 Å.¹⁰⁹ The lattice constant values for different samples along with density and porosity measurements are listed in Table 5.1. The effective density (ρ_{eff}) was calculated by employing Archimedes 'principle (ASTM B962). Using the XRD data, the lattice constants (a, b, and c), unit cell volume (V), and theoretical density (ρ_{th}) were determined and the relative porosity was calculated from ρ_{th} and ρ_{eff} employing equations (eq. 4.2-4.5).

It is evident from Table 5.1 that increasing T_{sint} significantly influences the relative density and porosity of the materials. The variation in the density with the sintering temperature is shown in Figure 5.2. The GFO samples sintered at 900 °C show relatively lower density compared to samples sintered at higher temperatures. While the density improves significantly with T_{sint} , there is no appreciable change in the density for $T_{\text{sint}} = 1100\text{--}1200$ °C. Inhomogeneity, incomplete phase formation, incomplete or partial sintering, or the presence of porosity might be the reasons for the observed low density of the GFO compounds at lower T_{sint} . Furthermore, the presence of porosity or atomic-scale defects is unavoidable in high-temperature chemical synthesis processes. With increasing sintering temperature, cavities vanish, and the samples become denser. The evidence for grain coalescence was provided by the electron microscopy analysis, as presented and discussed in subsequent sections. However, while an appropriate heat preservation temperature can optimize the sample density, a very high insulation temperature may result in a loss of parental oxide by evaporation, leading to a decrease in the density.¹¹⁰ This effect is quite prevalent in different oxides of molybdenum.¹¹¹⁻¹¹² Thus, from the XRD and density measurements, $T_{\text{sint}} = 1100\text{--}1200$ °C appears to be preferable to obtain relatively dense GFO compounds crystallized in a monoclinic β -phase.

Having understood the crystal structure and density of the GFO compounds, we now consider the effect of T_{sint} on the average crystallite size and micro-strain in the GFO compounds. The average crystallite size was calculated using the Scherrer formula:¹¹³

$$\beta_s = \lambda/D \cos \theta \quad (\text{Eq. 5.1})$$

where, D is the average crystallite size, λ is the Cu K_α radiation wavelength (1.5406 Å), θ is Bragg's angle, and β_s is the measured integral peak width. The integral width was obtained by multiplying the shape factor (1.06), which is dimensionless. A Gaussian profile is used for

measuring the full width at half maximum (FWHM) of the peak. The intense (002), (111), (-311), and (-712) reflection peaks were used in the peak broadening analysis to determine the average crystallite size. The crystallite size of the GFO compounds determined from these calculations is ~55 nm. Variation of the average crystallite size with T_{sint} is not significant; the crystallite size varied in the range of ~55–64 nm. The micro-strain in the GFO compounds was evaluated by the standard Williamson–Hall (W–H) method using a Gaussian profile fitting for FWHM calculations.¹¹³ The strain values increase gradually with increasing sintering temperature and then, finally, they remain constant at 0.17%. The average crystallite size and micro-strain approach their optimum values of 55 nm and 0.17%, respectively, at 1100–1200 °C. The optimized calcination temperature increases the specific surface area. Du et al. reported that the average particle size of 30 nm of gallium-doped zinc oxide calcined at 540 °C for 1.5 h showed better electrical properties.⁴⁶ The sintering ability depends on the particle size distribution range. The effective sintering of the compact occurs when the particles size distribution is narrow. The porosity present in the green compact also plays a crucial role in influencing the sintering ability. When the porosity is eliminated from a locally dense region, those particles will not further take part in sintering; this requires the porosity within the green compact to be of close size.⁴⁷

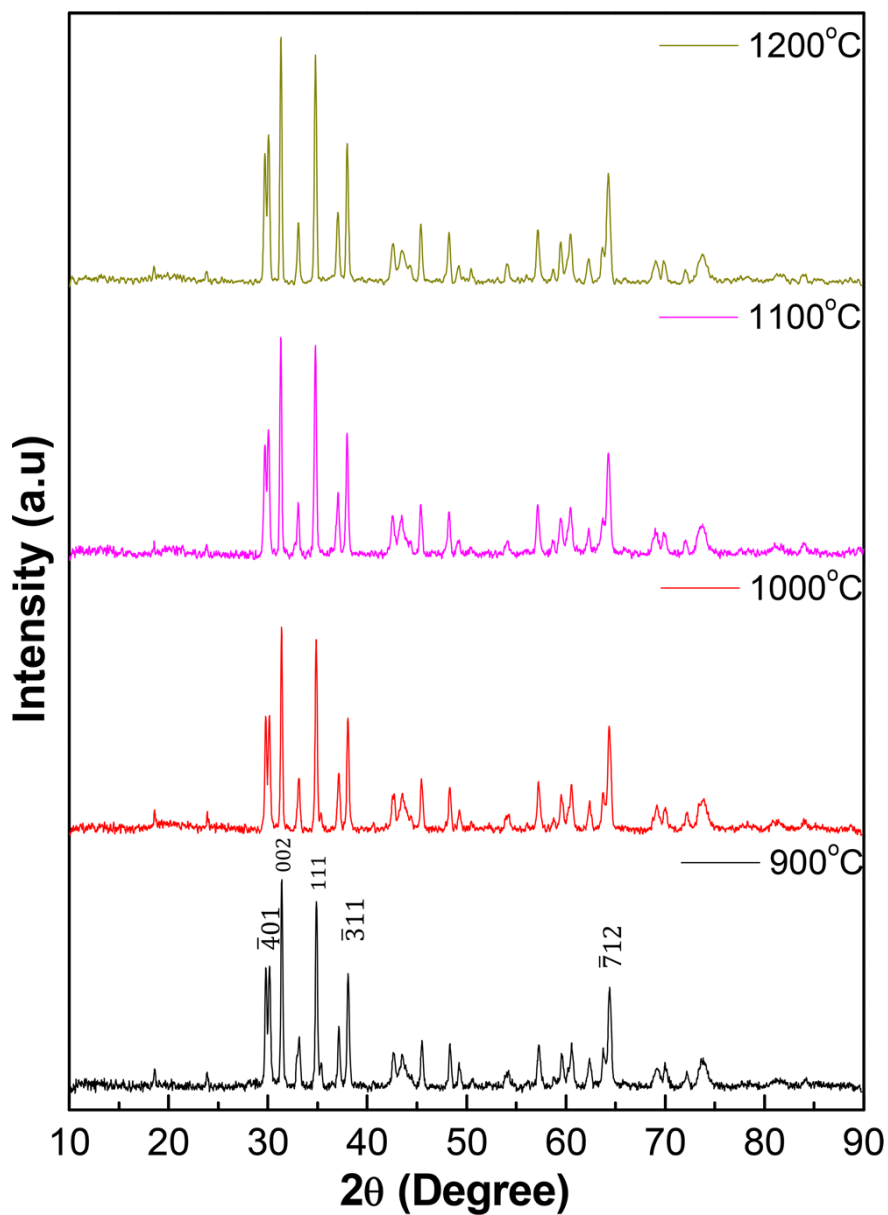


Figure 5.1: XRD patterns of GFO compounds as a function of T_{sint} . All of the GFO compounds crystallize in a monoclinic β phase of Ga_2O_3 . It is evident that the peak intensity increases with increasing T_{sint} .

Table 5.1: Lattice Parameter, Unit Cell Volume, Density and Relative Porosity of GFO Compounds for Different Sintering Conditions

Sintering Temperature T_{sint} ($^{\circ}\text{C}$)	Lattice Parameter (\AA)			β	Unit Cell Volume V (\AA^3)	Theoretical Density (ρ_{th}) (g/cm^3)	Effective Density (ρ_{eff}) (g/cm^3)	Relative Porosity (%)	
	a	b	c						
	900	12.625	3.040	5.957	107.69°	218.399	5.657	4.048	38.98
	1000	12.396	3.040	5.944	106.52°	217.923	5.661	3.902	32.43
1100	12.410	3.050	5.933	106.20°	217.996	5.667	3.825	31.18	
1200	12.415	3.050	5.931	106.08°	218.054	5.668	3.452	28.58	

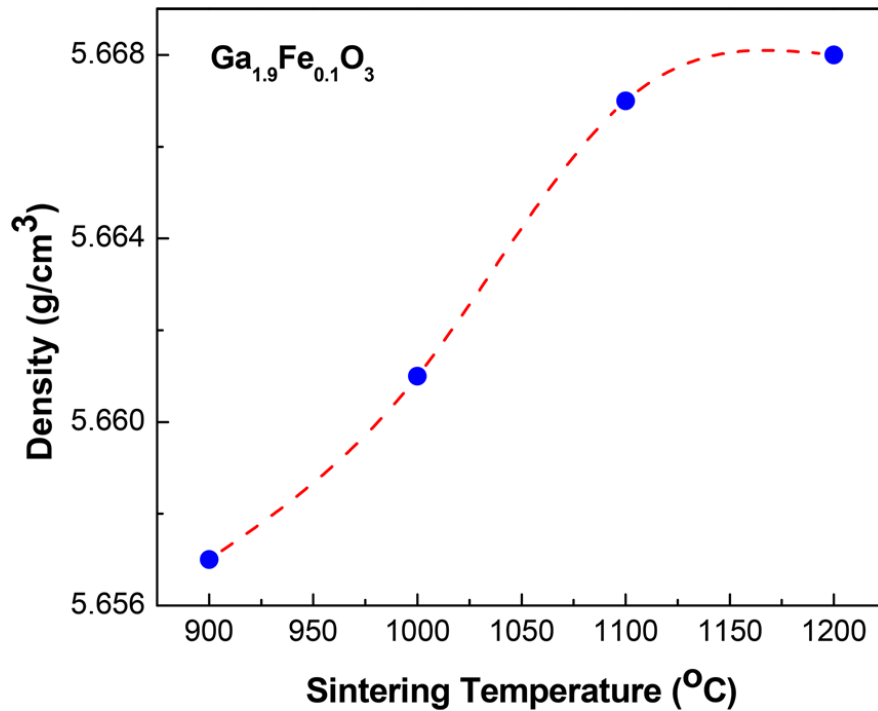


Figure 5.2: Density variation of the GFO compounds with T_{sint} . It is evident that the density increases with increasing T_{sint} .

The Raman spectroscopic data of Ga_{1.9}Fe_{0.1}O₃ ceramics are shown in Figure 5.3. It can be seen that the spectra exhibit several characteristics peaks, which are indicative of crystalline nature of the samples. Furthermore, the Raman scattering peak evolution with increasing T_{sint} is evident (Figure 5.3). The Raman spectra can be conveniently analyzed, based on the crystal structure and crystal symmetry considerations of Ga₂O₃, in order to understand the chemical quality and chemical bonding within Ga_{1.9}Fe_{0.1}O₃. The monoclinic β-Ga₂O₃ belongs to the space group C2/m/C32h. According to factor group analysis,¹¹⁴ the crystal modes can be classified according to:

$$\Gamma_{\text{opt}} = 10A_g + 5B_g + 4A_u + 8B_u \quad (\text{Eq. 5.2})$$

where, symmetry A_g and B_g phonon modes are Raman active while phonon modes with A_u and B_u symmetry are infrared active. Thus, a total of 15 Raman modes and 12 infrared active modes are predicted for β-Ga₂O₃.¹¹⁴⁻¹¹⁵ The Raman scattering peaks observed in the present work and their mode assignments are presented in Table 5.2. The data obtained for Ga_{1.9}Fe_{0.1}O₃ sintered at various T_{sint} are presented and compared with that of bulk Ga₂O₃. The Raman-active modes of Ga₂O₃ can be classified into three groups: high-frequency stretching and bending of GaO₄ tetrahedra (~770–500 cm⁻¹), mid-frequency deformation of Ga₂O₆ octahedra (~480–310 cm⁻¹), and low-frequency libration and translation (below 200 cm⁻¹) of tetrahedra-octahedra chains.¹¹⁵

The Raman peaks observed for Ga_{1.9}Fe_{0.1}O₃ ceramics sintered at T_{sint}= 1200 °C at 143, 168, 202, 345, 475, 652, and 763 cm⁻¹ correspond to B_g(2), A_g(2), A_g(3), A_g(5), A_g(7)/B_g(4), A_g(9)/B_g(5), and A_g(10) phonon modes, respectively.¹¹⁶ The bands at lower frequencies are assigned to the librations and translations of chains. The bands at 413, 345, 320 cm⁻¹ are assigned to the deformation of octahedron.¹¹⁶ The bands at 763, 652, 629, 475 cm⁻¹ are derived from the

stretching and bending of tetrahedron.¹¹⁶ The peak positions and mode assignments are in good agreement with those reported for β -Ga₂O₃ bulk. In addition, these observations and Raman mode assignments of the peaks are also in agreement with those reported for β -Ga₂O₃ thin films and nanowires.¹¹⁴⁻¹¹⁷

The combined effect of Fe doping and processing conditions (T_{sint}) on the structural quality and chemical bonding in Ga_{1.9}Fe_{0.1}O₃ ceramics can be understood as follows. With Fe content, the Raman active modes of Ga_{1.9}Fe_{0.1}O₃ ceramics have a clear shift (see, Table 5.2). In addition, the Raman scattering peaks in the spectra also exhibit a line broadening (Figure 5.3) for Ga_{1.9}Fe_{0.1}O₃ ceramics. However, this is more dominant at lower T_{sint} . The broadening of the Raman peaks is clearly seen at $T_{\text{sint}}= 900$ °C; the peaks continue to be broader until $T_{\text{sint}}= 1100$ °C, at which point the peaks become sharp. Also, this peak broadening is particularly true for the Raman modes in the low-to-mid spectral range between 300 and 500 cm⁻¹, which is due to Fe atoms entering into the crystal lattice of Ga₂O₃ to form the Ga_{1.9}Fe_{0.1}O₃ ceramics. Such peak broadening in Raman modes due to dopant effects was also noted in β (GaAl)₂O₃ films, where the broadening of Raman modes was particularly dominant in the mid-spectral range with Al-doping.¹¹⁷ The peak around 1400 cm⁻¹ is vanishing as the sintering temperature has been increased which is shown by dotted circling in Figure 5.3. Wang et al. reported that, with the increase of Al content, the Raman active modes of (AlGa)₂O₃ films exhibited a right shift coupled with a line broadening, especially at higher Al content.¹¹⁷ This peak broadening of Raman modes in the 310-480 cm⁻¹ range was attributed to the more Al atoms entering into the crystal lattice of Ga₂O₃ to form ternary solid solution.¹¹⁷ However, the broadening observed in this case of Fe is not significant compared to Al in Ga₂O₃ due to the reason that Fe doping concentration is very less as well as ionic radii mismatch between Ga³⁺ and Fe³⁺ is very small.^{74, 118-120}

The Raman spectroscopic data and analyses are in corroboration with our previous XRD and SEM results, which were discussed quite extensively in our previous work.⁷⁴ However, in the context of understanding the importance of present work, we describe the salient features here. Phase purity of all the synthesized GFO compounds were confirmed from X-ray diffraction (XRD) patterns.⁷⁴ XRD data, high resolution scans as well as refinement procedures revealed that all the GFO compounds were phase pure without any secondary phases.^{74,119} For the specific composition in question i.e., $\text{Ga}_{1.9}\text{Fe}_{0.1}\text{O}_3$, it is evident from the XRD data that there is no secondary phase formation at any of the T_{sint} values. However, although not significant, a slight positive shift of the peak position with increasing T_{sint} can be noted. Thus, increasing T_{sint} induces a reduction in the interplanar distance between the crystal planes. This in turn induces some amount of strain in the crystal which may be due to Fe doping or excess thermal energy.⁷⁴ The effect of T_{sint} was not very significant; grain size varied in the range of ~55-64 nm with T_{sint} . However, the strain values increased gradually with increasing sintering temperature. The major effect of T_{sint} is the drastic decrease in porosity, which approaches minimum when the optimum $T_{\text{sint}}=1200^\circ\text{C}$ is used for synthesis of $\text{Ga}_{1.9}\text{Fe}_{0.1}\text{O}_3$ samples.⁷⁴ Also, because of the difference in the ionic radii of Fe^{3+} and Ga^{3+} and Fe^{3+} (0.64 Å) has smaller ionic radius than Ga^{3+} (0.76 Å), so iron doping will facilitate the formation of smaller nuclei during synthesis process. Incorporation of Fe in Ga_2O_3 may inhibit the grain growth during sintering process.⁷⁴

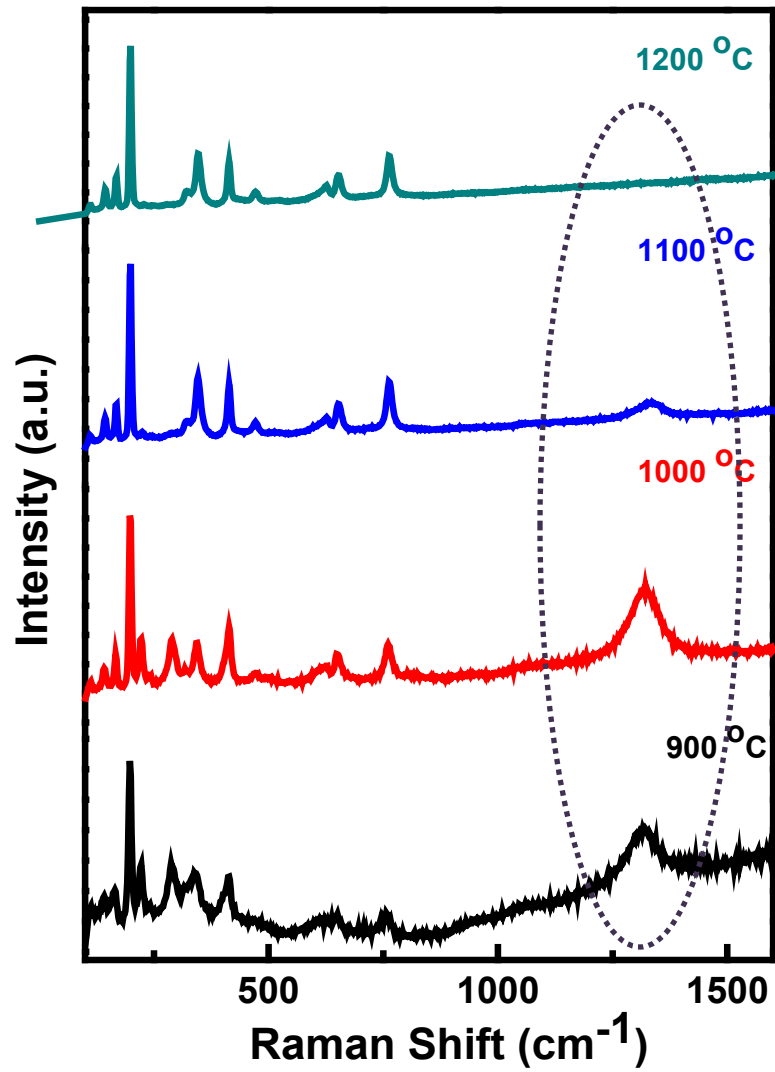


Figure 5.3: Raman shifts of differently sintered GFO compounds.

Table 5.2: Raman data for Ga_{1.9}Fe_{0.1}O₃ ceramics at various T_{sint}. The data of Ga_{1.9}Fe_{0.1}O₃ ceramics is compared with that of bulk Ga₂O₃

Serial No.	Mode Symmetry	Rao et al. ¹¹⁶		This Work (Sintering Temperature) (°C)							
		Bulk Empirical Calculation (cm ⁻¹)	Bulk Experimental Data (cm ⁻¹)	900 (cm ⁻¹)	Frequency Shift (cm ⁻¹)	1000 (cm ⁻¹)	Frequency Shift (cm ⁻¹)	1100 (cm ⁻¹)	Frequency Shift (cm ⁻¹)	1200 (cm ⁻¹)	Frequency Shift (cm ⁻¹)
1	A _Z	104	-	-	-	-	-	-	-	-	-
2	B _Z	113	-	112	-	112	-	112	-	-	-
3	B _Z	150	144	140	-4	143	-1	143	-1	140	-4
4	A _Z	166	169	165	-4	165	-4	168	-1	168	-1
5	A _Z	207	200	196	-4	196	-4	202	+2	199	-4
6	A _Z	317	317	-	-	317	0	320	+3	317	0
7	A _Z	348	344	342	-2	345	+1	345	+1	343	-1
8	B _Z	356	-	-	-	-	-	-	-	-	-
9	A _Z	414	416	413	-3	413	-3	413	-3	412	-4
10	A _Z	469	472	-	-	472	0	-	-	472	0
11	B _Z	474	-	-	-	-	-	475	+1	-	-
12	A _Z	601	629	611	-18	-	-	-	-	-	-
13	B _Z	624	-	-	-	627	-	627	-	622	-
14	A _Z	635	654	652	-2	649	-5	652	-2	655	+1
15	A _Z	732	767	754	-13	760	-7	763	-4	763	-4

The SEM images of the GFO compounds are presented in Figure 5.4. It is clear from the images that the sintering temperature influences the final microstructure to a greater extent. The sintering temperature induced grain growth, and grain coalescence can be seen in these images. The porosity level is quite higher in low-temperature sintered samples; however, the porosity decreases as T_{sint} approaches the optimum at T_{sint} = 1200 °C. It is evident from the images that, although the particle sizes remained almost the same for all samples, the coalescence degree increased with increasing T_{sint}. The average particle size values obtained from the SEM micrographs employing ImageJ analysis are tabulated in Table 5.3. The smaller particles observed in the 900, 1000, and 1100 °C samples are no longer present in the 1200 °C sample. The apparent larger particles seen in the 1200 °C sample are due to coalescence of the smaller particles.

As the heat preservation temperature goes up, grains receive more energy. In this scenario, integration and annexation phenomena between grains become obvious. As a result of these, most of the voids and/or holes present in the material disappear, leading to continuous grain growth.¹¹⁰ Atuchin et al. and Lim et al. have also mentioned similar kinds of behavior.¹²¹ Beside this, Fe-doped into gallium oxide could also be the reason behind the observed microstructural variation. Fe doping may facilitate the formation of smaller nuclei during the synthesis process and inhibit grain growth during the sintering process. Fe^{3+} may act as a kinetic barrier for grain displacement and segregation throughout the microstructure, preventing further grain growth.⁴⁷⁻⁴⁸ Although most of the Fe^{3+} ions will occupy substitutional lattice positions, some fractions can sit in the defect chemistry and/or in the interstitial positions and inhibit the grain growth process. Grain growth mainly takes place by the free movement of the grain boundaries or if one grain consumes another. It follows the procedure of recovery and recrystallization in metals, but it is quite similar in the case of ceramics and minerals. The internal energy that is associated with the interfacial area must be released or reduced in the whole procedure. Thus, the final microstructure of the GFO material is influenced by the combined effect of sintering conditions and Fe content doped into GFO.

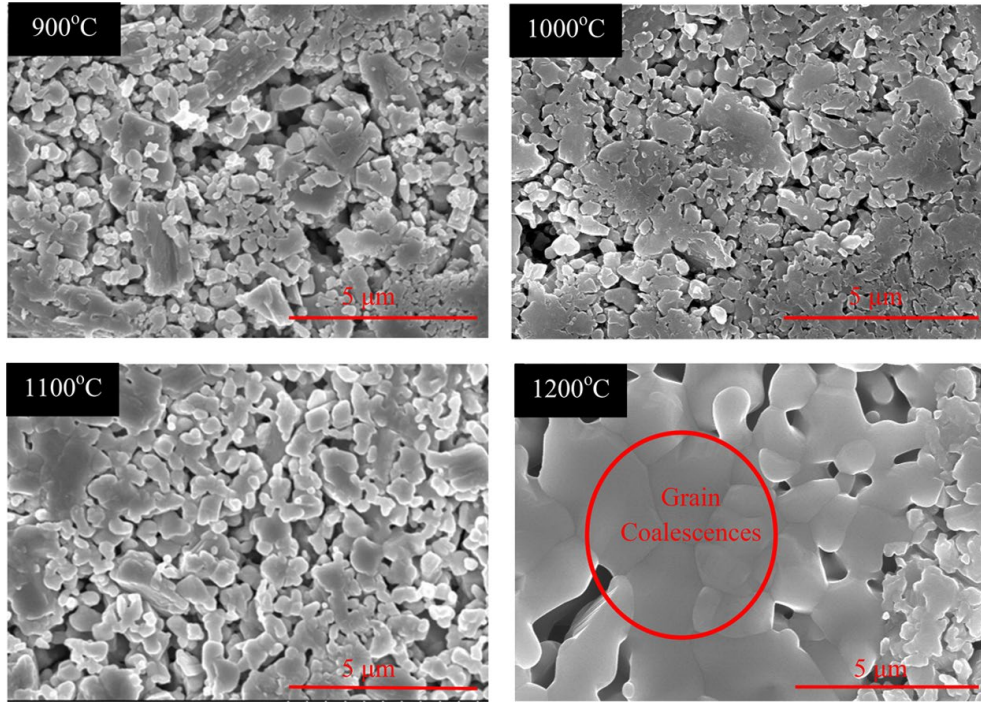


Figure 5.4: SEM images of GFO materials as a function of T_{sint} . Coalescence of grains occurs with increasing T_{sint} .

Table 5.3: Average Particle Size Measured from SEM Micrograph

Sintering Temperature (°C)	Average Particle Size (μm)
900	0.90±0.35
1000	0.93±0.29
1100	0.99±0.30
1200	2.10±1.06

5.2 CHEMICAL ANALYSIS

5.2.1 Energy-Dispersive X-ray Spectroscopy (EDS)

The EDS studies indicate that the GFO materials obtained under different firing conditions are stoichiometric and homogeneous with uniform distribution of constituent elements. The EDS data of GFO are presented in Figures 5.5 and 5.6, respectively. The typical EDS spectrum of a

GFO sample is shown in Figure 5.5. The characteristic X-ray peaks from Ga, Fe, and O atoms are evident in the EDS spectrum (Figure 5.5). The peaks are representative of Ga K_α, Ga K_β, Fe K_α, Fe K_β, and O K_α at their respective energy positions, consolidating the presence of Ga, Fe, and O atoms in the compound. Being a qualitative analytical tool, the EDS data can be used to confirm the chemical quality of the GFO compounds synthesized. Also, the EDS elemental data (composition in atom %) listed in Table 5.4 indicates that the doped ceramic compound maintains a proper atomic ratio during doping between the parental compound (Ga) and the dopant (Fe), having the chemical formula Ga_(2-x)Fe_xO₃ for all of the sintered samples.

The elemental mapping images of GFO samples are shown in Figure 5.6. The mapping images of Ga K, O K, and Fe K obtained for samples at different T_{sint} are presented. These mapping images clearly reveal the uniform elemental distribution. It is evident from these images that Fe doping into gallium oxide is homogeneous in terms of the distribution of the constituent atoms across the microstructure. Therefore, we can safely conclude that sintering at various temperatures did not establish a concentration gradient of a particular element, but rather it helped to obtain a homogeneous microstructure with uniform distribution of the elements. However, similar to SEM imaging analysis, based on the color contrast of the respective mapping images, it can be claimed that the samples become more compact with increasing T_{sint}. This is more prominent, as revealed in the mapping of Fe K for the sample sintered at 1200 °C.

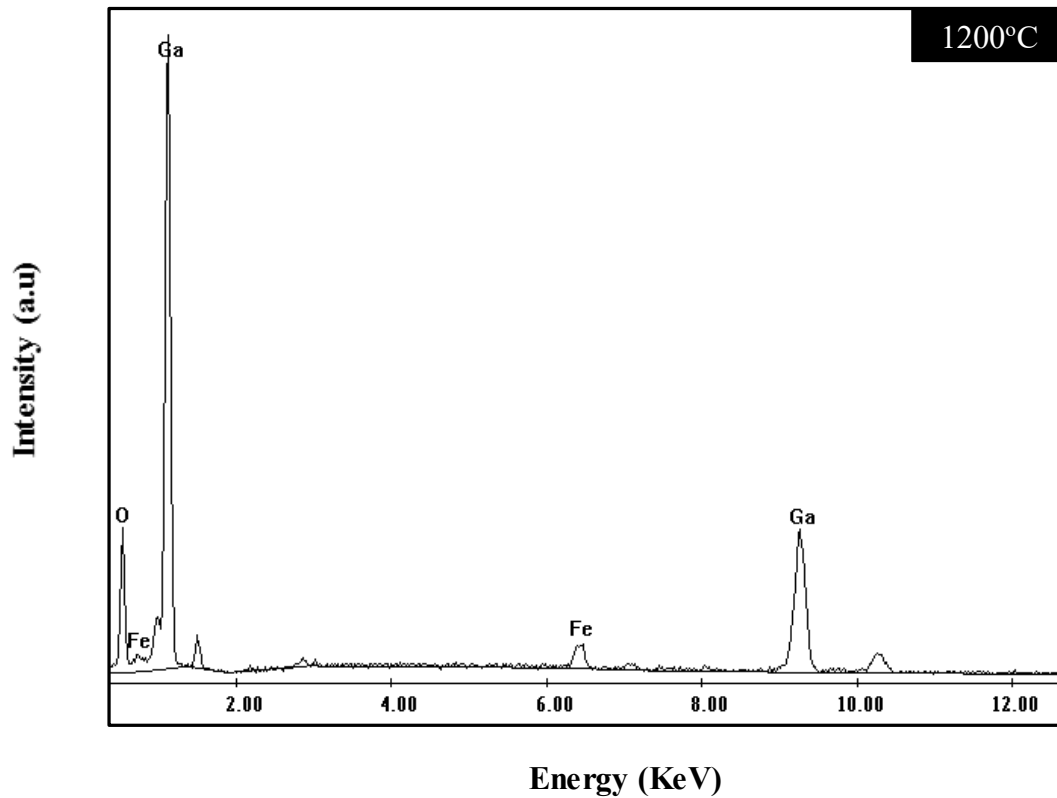


Figure 5.5: EDS spectrum of the GFO material sintered at 1200 °C. The respective X-ray peaks due to Ga, Fe, and O atoms are as labeled.

Table 5.4: Elemental Composition Data from EDS

Sintering Temperature (°C)	Ga (at.%)	Fe (at.%)	O (at.%)
900	56.12	3.29	40.60
1000	55.25	3.89	40.86
1100	57.01	3.73	39.26
1200	56.38	3.45	40.17

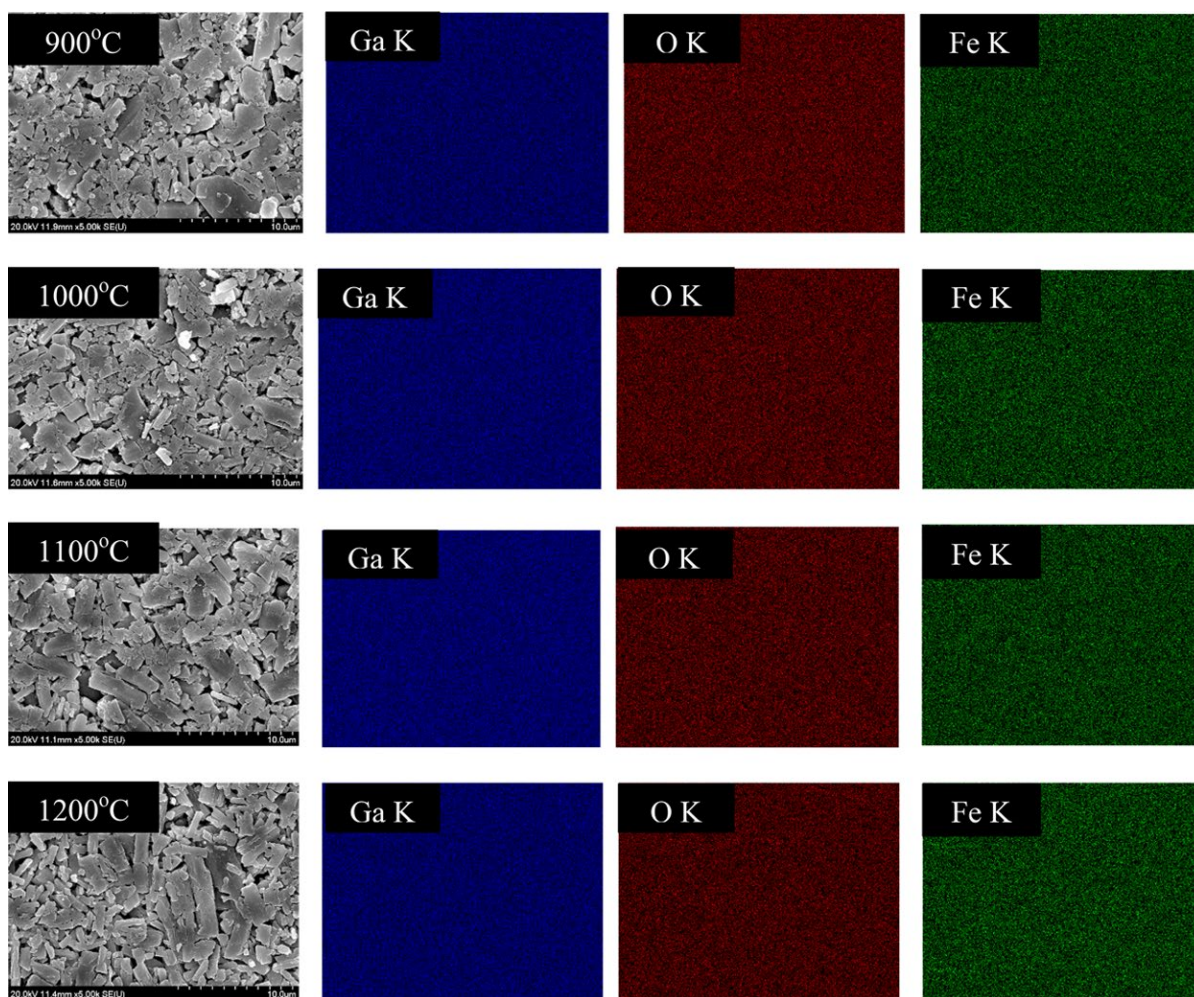


Figure 5.6: Elemental mapping images of GFO compounds synthesized at different T_{sint} . The corresponding SEM images are also shown. Chemical uniformity of the GFO samples is evident from the images.

5.2.2 X-ray Photoelectron Spectroscopy (XPS)

The XPS survey and deconvoluted core level spectra (Ga 2p, Fe 2p and O 1s) of $\text{Ga}_{1.9}\text{Fe}_{0.1}\text{O}_3$ compounds are shown in Figure 5.7 and 5.8, respectively. The Ga 2p and O 1s peaks are labelled in the survey spectra, but Fe concentration is so less that it can't be observed throughout the spectra, though high resolution XPS spectra evidenced the presence of Fe. The peak assignments were done after comparing with the binding energy (BE) following the standard NIST database.¹²² The Ga 2p region (Figure 5.8(a)) combination of Ga 2p doublet i.e., the Ga 2p_{3/2} and Ga 2p_{1/2} peaks, which are located about at BEs of 1117.34 and 1144.17 eV, respectively. For the

pure Ga metal, the location of Ga 2p_{3/2} is around 1116.50.¹²² Compared to the Ga metallic state, the observed Ga 2p_{3/2} peak shows almost 1 eV positive shift corroborating that all the Ga exists in the oxidation states. Ga 3d peak was also recorded (not shown) at a BE of 20.3 eV. This exhibited positive shift in the BE of Ga 2p_{3/2} peak is owing to the redistribution of the electronic charge, as Ga stabilized as Ga₂O₃ in the GFO compounds. The Ga 2p XPS data, which are consistent with the reported values in the literature for Ga₂O₃, validates the claim that Ga ions exist in the highest valence states (i.e., Ga³⁺) in all the GFO compounds.⁶⁵

Figure 5.8(b) depicts the HR XPS spectra of Fe 2p region. The deconvoluted spectra of Fe 2p region clearly reveals that Fe exhibits mixed valance state (i.e., Fe³⁺ at 711 eV and Fe²⁺ at 708.7 eV) for 1100 °C and 1200 °C sintered samples whereas single valance state (i.e., Fe³⁺) of Fe exists for rest of the sintered samples.¹²² It can be related to the varying diffusion rate associated with the electronic flux as sintering temperature approaches the optimized condition. This will help to achieve many unique as well as important characteristic properties such as magnetic, spintronic, and optical etc. out of the GFO compounds as a result of jumping and sharing of electronic clouds between these two valance states.

The O 1s peak (Figure 5.8(c)), at a BE of 530.87 eV, is the characteristic feature of Ga-O bond.^{119, 123-124} The O 1s peak is not symmetric for all the sintered compounds. The HR core level spectra fitting mainly results in three components representing different chemical states. The most intense peak centered at B.E. of 530.25 eV is the characteristic peak of oxygen bonded to Fe within the GFO compound.^{119, 124} The third component located at higher BE (i.e., 532 eV), attributing to either carbonyl (oxygen bonded to carbon) or hydroxyl (oxygen bonded to hydrogen) groups, which were adsorbed on the sample surface as impurities during sample handling, appear as a shoulder contribution with minor intensities.⁶⁵ It can be noticed from O 1s spectra (Figure 5.8(c))

that as the sintering temperature approaches optimized condition the contributions from Ga_2O_3 and iron oxides are levelling off. In 900, 1000 and 1100 °C sintered samples the iron oxide contribution is quite higher than the Ga_2O_3 . This has happened because the precursor iron (III) oxide powder used for preparing these GFO compounds, was not well diffused through the system and dispersed mainly around the surface due to inefficient firing condition. Moreover, being a surface sensitive technique, XPS easily catches those iron oxide signals and as a result the iron oxide intensity came up as higher than the Ga_2O_3 . With increasing sintering temperature, these excess undissolved iron (III) oxide compacts on the surface diffused through the bulk and intensity of iron oxide came down subsequently.

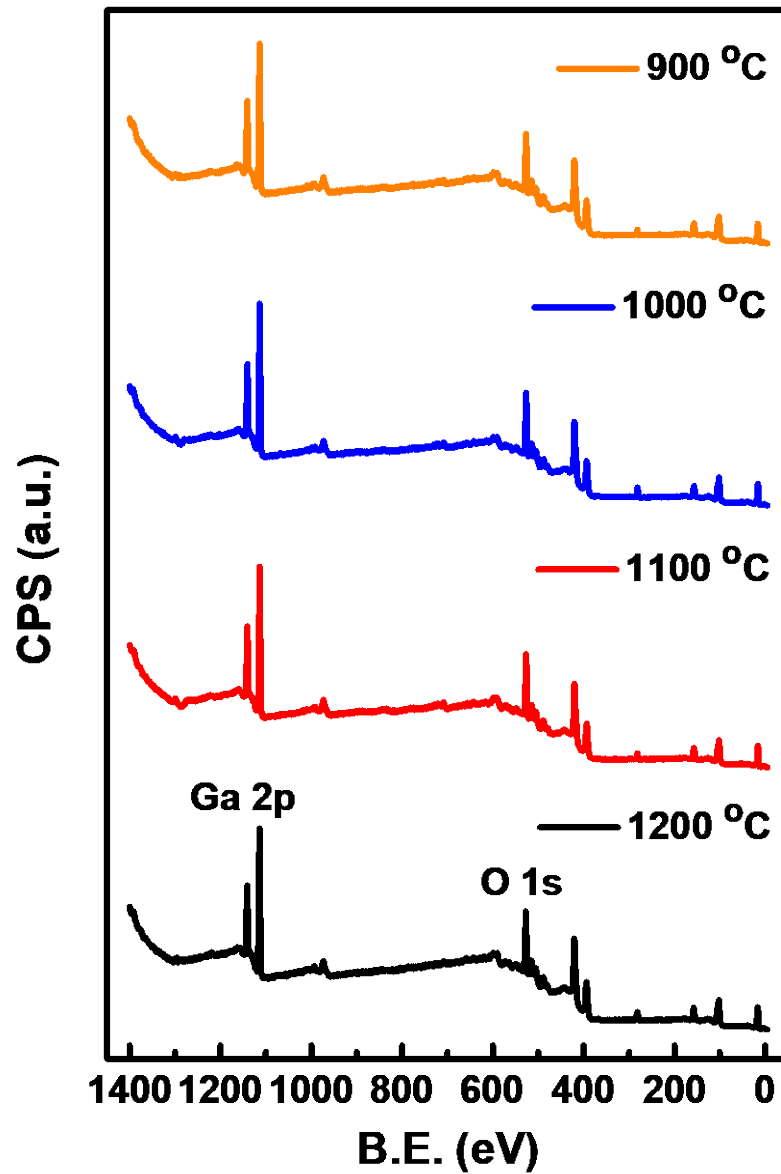


Figure 5.7: Survey spectra of GFO compounds at various sintering temperature.

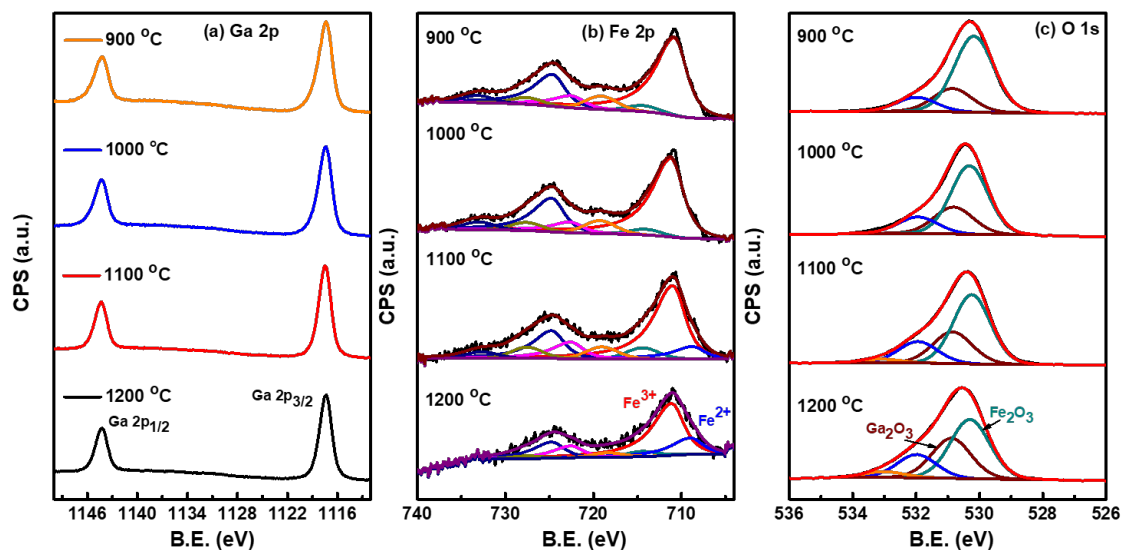


Figure 5.8: High resolution XPS spectra of (a) Ga 2p (b) O 1s (c) Fe 2p.

As temperature is closed to the optimized condition, Fe starts diffusing from the surface to the bulk and helps to achieve a uniform elemental dispersion throughout the sample. XPS study also proves that the main constituent elements present in the GFO compounds are nearly stoichiometric. XPS study revealed that the samples show mixed or single valence states depending on the sintering condition. Moreover, stoichiometry of the constituent elements is verified employing the XPS analysis.

5.3 DIELECTRIC PROPERTIES

The results obtained from dielectric property measurements on the differently sintered GFO samples are shown in Figures 5.9-5.11. The real (ϵ') and imaginary(ϵ'') parts of the dielectric constant and loss tangent ($\tan \delta$) for GFO are shown in Figures 5.9-5.11, respectively. It is evident that (Figure 5.9) the dielectric constant is very high at lower frequencies and then starts to decrease with increasing frequency. The associated high dielectric loss (Figure 5.11) at low frequency might be due to the mobile charge carriers, direct-current conductance, and defects present in the samples.¹²⁵ The mobility of free charge carriers increases the conductivity, which, in turn,

increases dielectric losses due to charge leakage.¹²⁶ Perhaps, the differences in the microstructure and grain size may account for the observed differences in the dielectric behavior of these GFO materials synthesized at various T_{sint} . Note that ϵ' increases with decreasing grain size;¹²⁷ in fact, the samples sintered at 1200 °C registered higher ϵ' values than others. Charge accumulation at the interfaces especially at the grain boundaries increases the ϵ' value. Whereas grains are semi-conductive, grain boundaries act as highly insulating layers. When the grain size is decreased, the grain boundary area will only increase, giving more resistance to the charge mobility and thereby reducing the conductivity. From the density consideration, the 1200 °C sintered sample registered higher density among the other samples; also, it has less porosity and defect concentration because of its compact-ness. Because of its lower porosity and atomic defects, the charge loss through leakage will be minimal, and it is able to store huge amounts of charge. Although the 1200 °C sintered sample has comparatively higher particle size in some regions, it also has some microstructural area consisting of particles that are more or less similar in size to the rest of the samples. Among the two mechanisms described above, the second mechanism is more dominant in nature in this case.

Figure 5.12 represents the measured and simulated frequency dependences of ϵ' . Debye's model has been employed to simulate the experimental data and dispersion behavior, in addition to confirming the validity of such a model in accounting for the dielectric behavior. It is noticed that the dielectric constant decreases with increasing frequency; however, the decrease is rapid at lower frequencies but much slower at higher frequencies. This is because, at higher frequency regions, the species that contribute to the polarization phenomenon fall behind the applied voltage. Variation of the dielectric constant values with the frequency is an example of dispersion due to Maxwell–Wagner¹²⁵ type polarization, which agrees with the Koops phenomenological theory.¹²⁸

The dispersion behavior of this kind can be explained based on the contribution of various polarization sources.¹²⁹ The higher values of ϵ' at lower frequencies are mainly due to polarization of the interface and grain boundaries.¹³⁰ However, there is a high possibility that intrinsic factors like ionic, electronic, and space charge polarization can contribute to this fact. The ϵ' value decreases in the high frequency region due to less directional polarization. However, electronic charge carriers show strong localized behavior in a heavily polarized crystal system by electron-phonon coupling.¹³¹ This kind of dielectric phenomenon is obvious in materials having microstructural characteristics of dielectric and conductive phases. Because multiple ions (Ga, Fe, and O) are involved in the relaxation process, the modified Debye model was used to simulate the experimental data and observed dispersion behavior. In this model, ϵ' follows the relationship:

$$\epsilon'(\omega) = \epsilon'_{\infty} + \left[\frac{\epsilon'_0 - \epsilon'_{\infty}}{1 + (\omega\tau)^{2(1-\alpha)}} \right] \quad (\text{Eq. 5.3})$$

where, $\epsilon'(\omega)$ denotes the complex permittivity and $\epsilon'_0 - \epsilon'_{\infty}$ is the dielectric relaxation strength, with ϵ'_0 being the static (lowest frequency permittivity; 90 Hz in our case) and ϵ'_{∞} the permittivity at the highest frequency (1 MHz). τ is the Debye average relaxation time, α is the spreading factor of the actual relaxation time about the mean value, and the angular frequency (ω) of the field is expressed as $\omega = 2\pi f$, where f is the linear frequency of the applied field with a signal of 1 V.

The spreading factors of the GFO samples were obtained by employing a Cole-Cole plot.⁴⁷ However, in our modified method, the real part of the dielectric constant was taken rather than the complex part, and an integrated graph was plotted for $\ln[(\epsilon'_0 - \epsilon'_{\omega})/(\epsilon'_{\omega} - \epsilon'_{\infty})]$ versus $\ln \omega$ for all of the samples. A linear regression was performed to calculate the slope (Figure 5.13) and to determine the spreading factor α . The calculated values of the spreading factor (α) and relaxation time (τ) for GFO samples are documented in Table 5.5. These calculated values of τ and α were used to match the experimentally obtained values of ϵ' with the calculated values by fitting to

Debye's model (eq. 5.3), as shown in Figure 5.12. It is clear from Figure 5.12 that the experimental and calculated data are consistent with each other particularly at the higher-frequency region. Thus, the validity of the model is confirmed by asserting the likelihood of more than one ion contributing to the relaxation process.

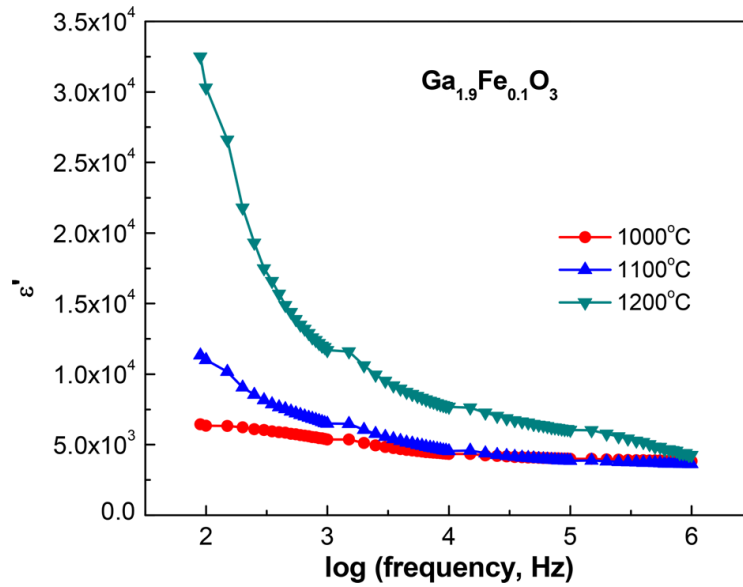


Figure 5.9: Comparison of the real part of the dielectric constant of GFO materials synthesized at different $T_{\text{ sint.}}$. The frequency dispersion of the dielectric constant is shown.

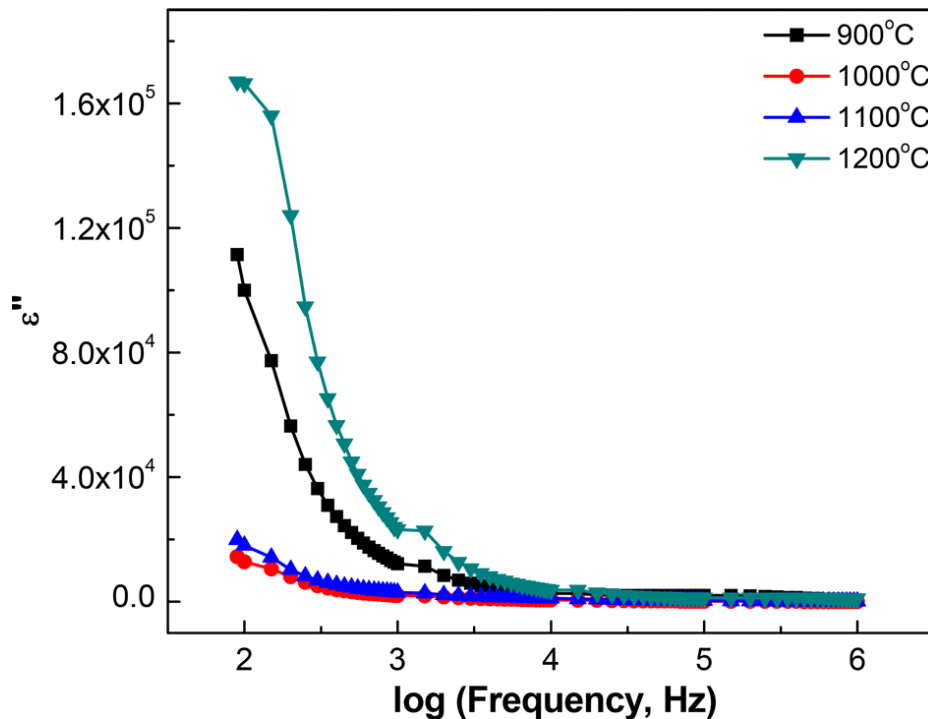


Figure 5.10: Comparison of the imaginary part of the dielectric constant of GFO materials prepared at different $T_{\text{ sint.}}$

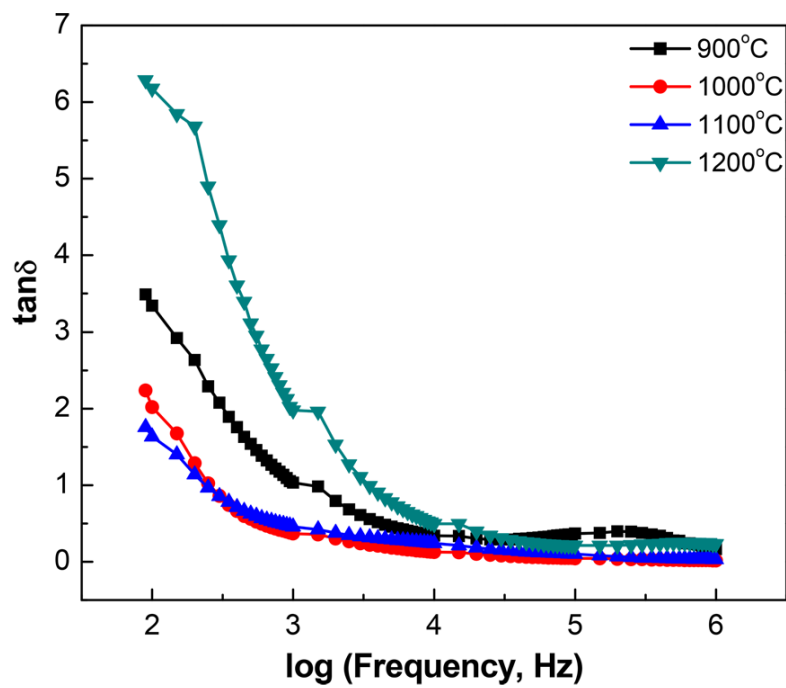


Figure 5.11: Comparison of the loss tangent of GFO materials prepared at different $T_{\text{ sint.}}$

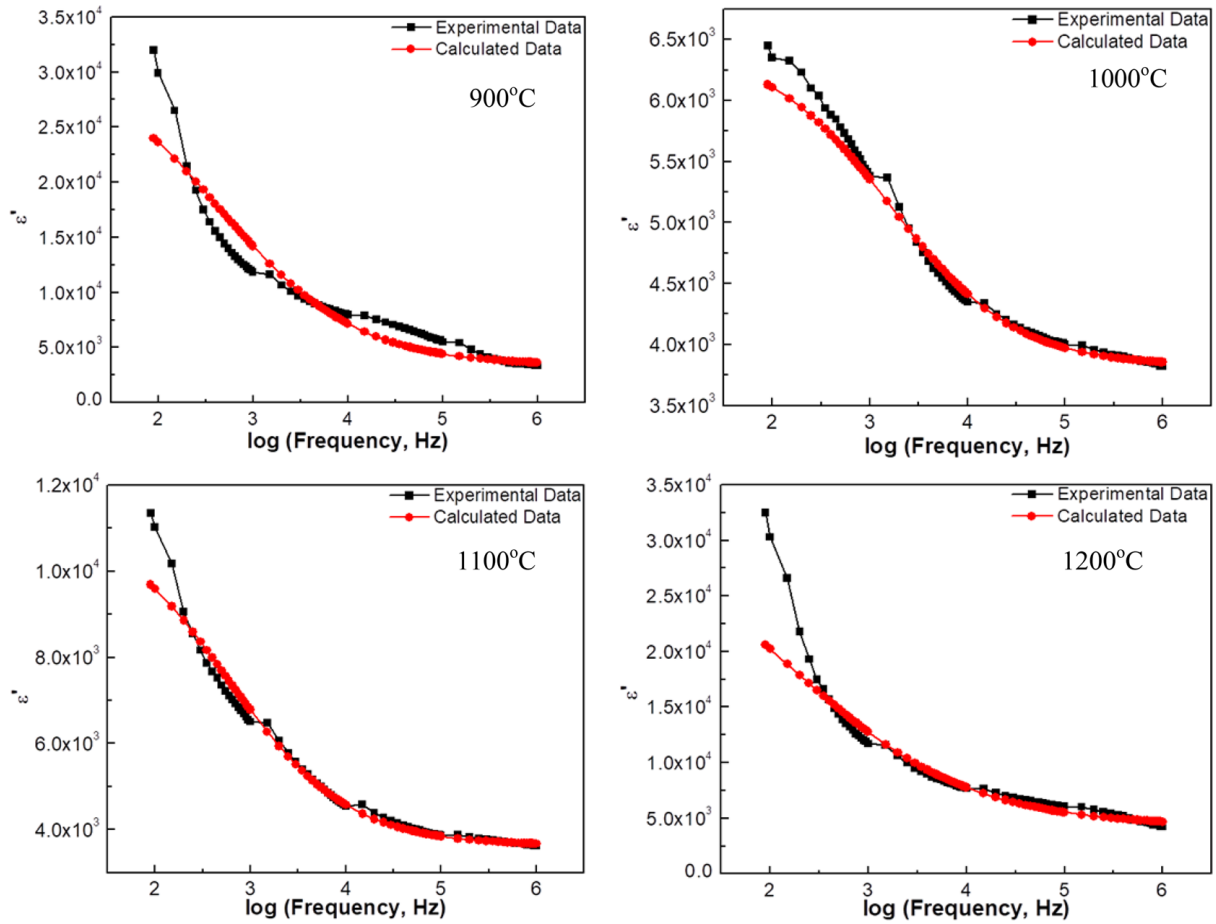


Figure 5.12: Variation of the real part of the dielectric constant of GFO materials prepared at different T_{sint} . The experimental and simulation data are shown. The dispersion behavior (experimental data) fits the modified Debye model (simulation data) function (see the text for the description).

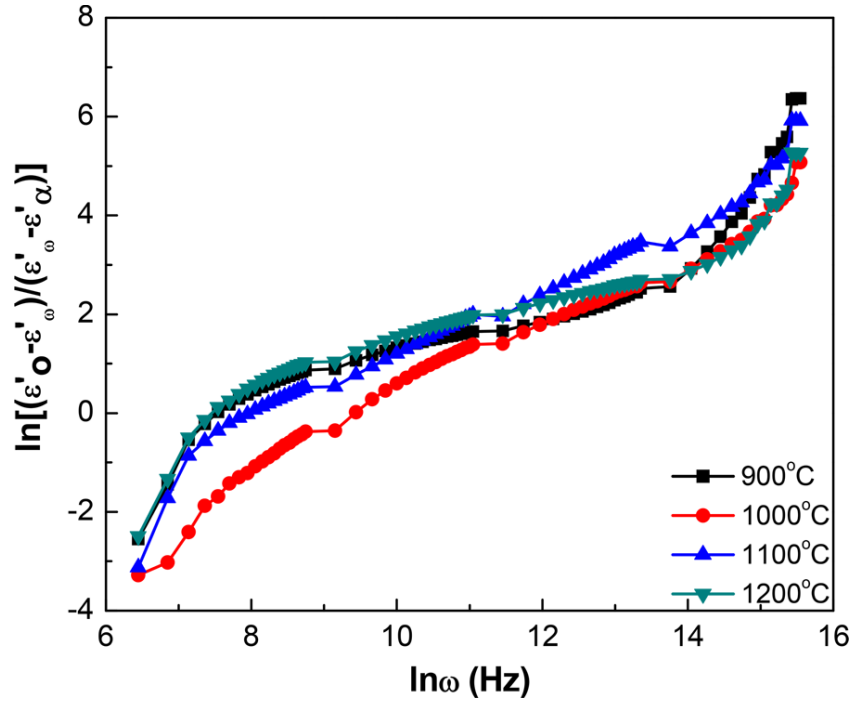


Figure 5.13: $\ln[(\epsilon'_0 - \epsilon'_\omega)/(\epsilon'_\omega - \epsilon'_\infty)]$ versus $\ln \omega$ plots of GFO materials. The spreading factor and relaxation time were calculated by fitting the curves.

Table 5.5: Calculated Values of the Spreading Factor (α) and Relaxation Time (τ) of GFO Compounds at Different T_{sint}

Sintering Temperature (T_{sint}) (°C)	Spreading Factor α	Relaxation Time τ (s)
900	0.699	0.000362
1000	0.658	0.000097
1100	0.654	0.000272
1200	0.759	0.000920

Finally, to validate the temperature stability of GFO materials, the temperature dependence of ϵ' of GFO materials was studied. Temperature-dependent ϵ' plots of GFO compounds are presented in Figure 5.14 as a function of the sintering temperature. It is evident from the plots that some of the samples show two dielectric relaxation peaks. There is a shift of dielectric maxima

toward higher temperature with decreasing T_{sint} . GFO samples sintered at 1200 °C show the highest dielectric constant values. The first dielectric relaxation can be noted in the temperature range of 350-450 °C, while the second relaxation peak appears at ~500 °C. Also, the dielectric constant values increase monotonically with the temperature for all of the GFO samples sintered at various T_{sint} . The very high or giant dielectric permittivity observed might be due to the charge injection, illumination, or temperature itself.¹³¹ At the lower-frequency range, all types of polarizing sources, i.e., ionic, electronic, dipolar, and space charge, contribute to the higher values of ϵ' . This might be due to the fact that, at higher frequency, polarization decreases as electron hopping lags behind the alternating current (ac) of the externally applied field.

The dielectric relaxation mechanism of ceramic materials is determined by several factors such as the synthesis method, microstructural and atomic defects (e.g., porosity and Schottky and Frenkel defects), temperature, associated electromagnetic field, ionic substitution, relative percentages of grain and grain boundary, interfacial area, etc.¹³⁰ The GFO crystallites are surrounded by grain boundaries and voids. Grain boundaries are rich in defect concentration, which may cause the trapping of free carriers, layer depletion, and band bending.¹³² Thus, the low-temperature dielectric relaxation occurs mainly because of the interfacial polarization caused by the charge carriers. The strong interaction between the lattice and charge carriers and the formation of a highly insulating grain boundary are the reasons behind the single relaxation behavior. At high temperature, space-charge polarization occurring at the grain boundaries associated with high-temperature oxygen vacancies contributes to the relaxation behavior.¹³³ The Fe doping in Ga_2O_3 with increasing sintering temperature increased the interionic distance, and that is evident from the higher values of the spreading factor and mean relaxation time (Table 5.5). A high bond length or large interionic distance increases the hopping distance for the GFO compound, which, in turn,

increases the α and τ values. The charge carrier's mobility and hopping rate increase at high temperatures because of sufficient availability of the thermal activation energy. Thus, the positive temperature shift of relaxation maxima can be attributed to the thermally activated relaxation process. This type of peak shifting appears when the jumping frequency of the localized electrons is almost the same as the frequency of an externally applied ac signal. The Rezlescu model claims that this relaxation peak appears as a combined effect of both p-type and n-type charge carriers.¹³⁴ Charge carriers cannot adapt to the fast-changing field as we go from lower to higher frequency, decreasing the polarization. So, higher thermal energy, i.e., higher temperature, is needed to show maxima at the higher-frequency level.

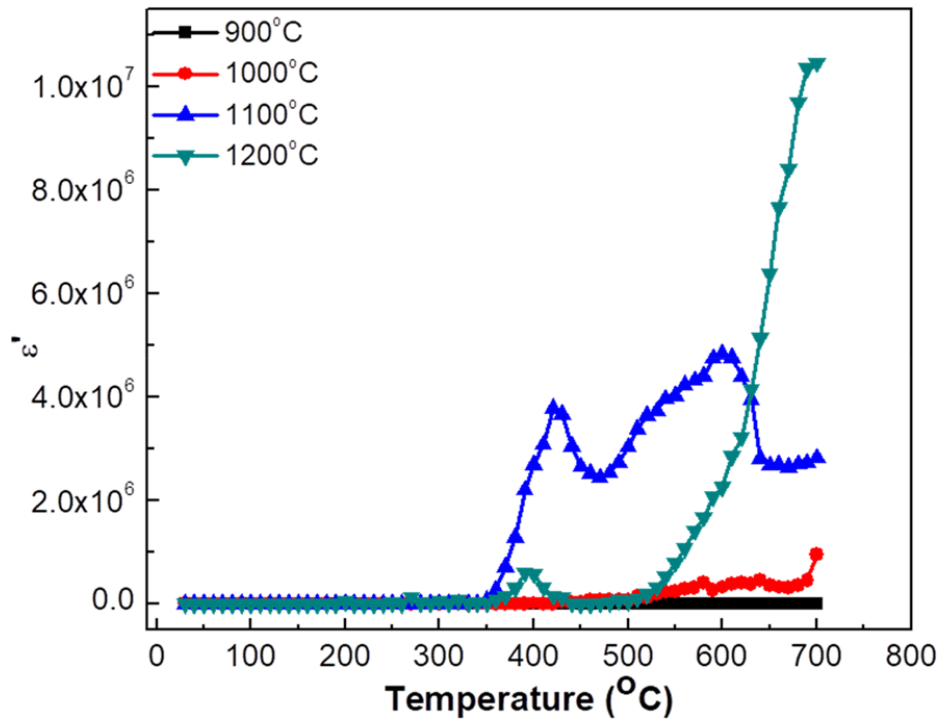


Figure 5.14: Temperature-dependent dielectric constant ϵ' (T) of GFO materials as a function of the sintering temperature. The data shown are obtained at a constant frequency of 1 MHz. It is evident that ϵ' (T) increases with increasing T_{sint} .

Chapter 6: Effect of Variable Fe Concentration- GFO Compounds at Optimized Sintering Condition

6.1 CRYSTAL STRUCTURE AND SURFACE MORPHOLOGY

Figure 6.1 shows the XRD patterns of selected GFO compounds where the calcination and sintering temperatures were kept constant at 1100 and 1200 °C, respectively and doping (Fe) concentration was varied from $x=0.00-0.30$. There is no discernible difference noticed for differently doped GFO compounds. The XRD patterns clearly indicate that the intrinsic Ga₂O₃ and GFO compounds crystallize in monoclinic phase with C2/m space group ((JCPDS #00-041-1103)).¹⁰⁸ The peaks and their respective positions are as indexed in Figure 6.1. The XRD patterns confirm the phase purity of the GFO compounds, where no sign of secondary phase is even at a relatively higher Fe content. As anticipated, a clear solid solution is formed because of close ionic radii of Ga³⁺ and Fe³⁺ in both tetrahedral and octahedral coordination.

The unit cell parameters of pure Ga₂O₃ and GFO compounds were calculated by the procedure outlined in previous section. The cell parameter values of GFO compounds are summarized in Table 6.1. The unit cell parameters of intrinsic Ga₂O₃ are in agreement with the literature.¹³⁵ Along with the cell parameters of GFO solid solutions, the data obtained on physical properties are also presented in Table 6.1. Effective density (ρ_{eff}) of the GFO samples was calculated employing Archimedes principle (ASTM B962). Relative porosity was calculated by comparing theoretical density (ρ_{XRD}) and ρ_{eff} .⁷⁴ It is evident (Table 6.1) that the cell parameters increase with increasing Fe content because of slightly higher ionic radius of Fe³⁺ compared to Ga³⁺. Also, because of the thermal processing of the compounds, lattice distortion might have taken place because of the difference in thermal expansion co-efficient. We can observe that, with increasing iron concentration, the lattice constant mismatch between the intrinsic Ga₂O₃ and GFO

compounds increases slightly. It is known that intrinsic Ga_2O_3 has inherent oxygen vacancies and atomic oxygen can be introduced in the pellets from the furnace atmosphere at high processing temperatures.⁷⁴ This atomic oxygen then converts into the molecular oxygen, which remains in the GFO defect structure, causing lattice distortion which may lead to slight increment in the unit cell parameter and consequently peak angle shifts in XRD pattern. Figure 6.2 shows the variation of theoretical density (ρ_{XRD}) with increasing Fe concentration. The measured effective density (Table 6.1) of the pellets is lower than the theoretical density. These lower values of the effective density (ρ_{eff}) depend on many factors such as duration of sintering process and presence of porosity and/or atomic scale defects, which is unavoidable in this kind of high-temperature ceramic synthesis process.^{106, 108} The calculated relative porosity is more or less same for all the pellets and is around 36% except for pure Ga_2O_3 which is 26.55%.

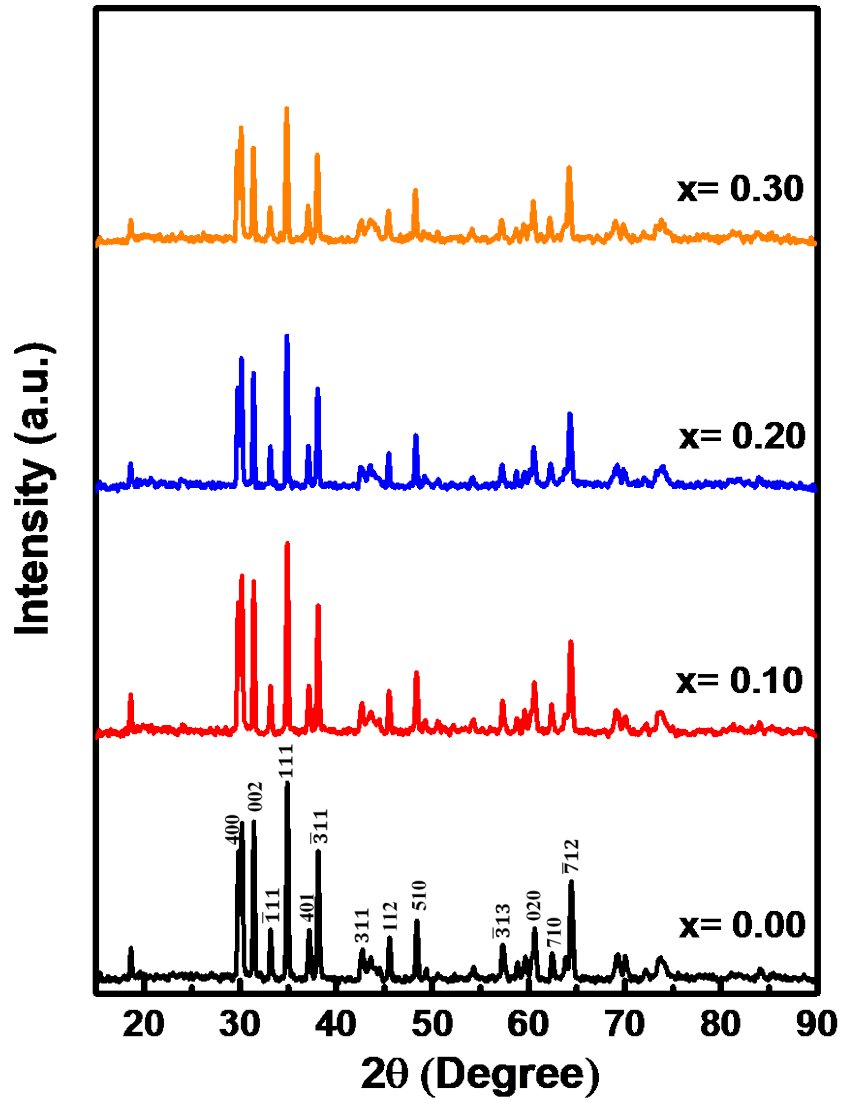


Figure 6.1: XRD pattern of GFO compounds.

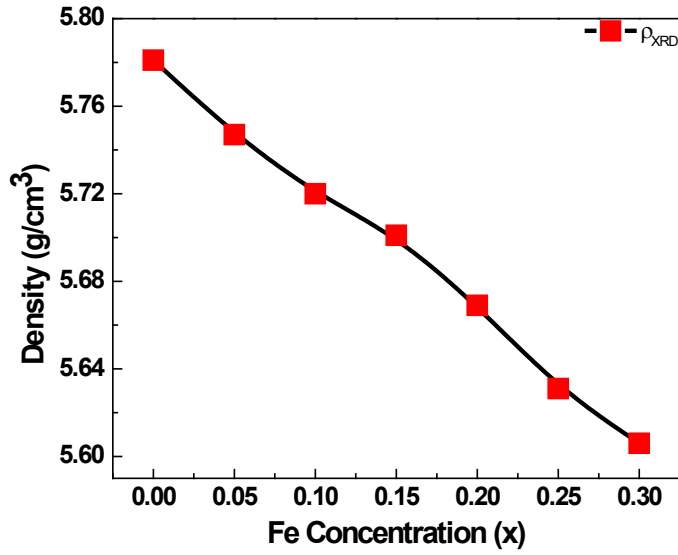


Figure 6.2: Variation of the theoretical density (ρ_{XRD}) of GFO compounds with Fe content. The unit cell volume values were determined from the XRD measurements.

Table 6.1: Lattice Constant, Unit Cell Volume, Density, and Relative Porosity of GFO Compounds

Dopant Concentration (x)	Lattice Parameter (Å)			Unit Cell Volume V (Å ³)	Theoretical Density ρ_{th} (g/cm ³)	Effective Density ρ_{eff} (g/cm ³)	Relative Porosity (%)
	a	b	c				
	0.00	12.405	3.052				
0.05	12.396	3.053	5.893	215.320	5.717	3.741	34.56
0.10	12.410	3.053	5.892	215.478	5.709	3.656	35.96
0.15	12.415	3.056	5.896	215.929	5.701	3.629	36.34
0.20	12.429	3.056	5.901	216.329	5.669	3.624	36.07
0.25	12.450	3.057	5.910	216.946	5.631	3.590	36.25
0.30	12.452	3.059	5.909	217.116	5.606	3.570	36.32

The variation of average crystallite size with Fe concentration was in the range of 57–62 nm. Thus, there is no considerable change in crystallite sizes with varying Fe concentration.

Structure Refinement: High-resolution XRD scans were used to perform the Rietveld refinement. The purpose of the detailed XRD high-resolution scans and refinement analyses was to better understand the Fe site occupancy and structural distortions (if any) in the parent lattice of β -Ga₂O₃. X-ray diffraction data reveal that all of the compounds were phase-pure without any secondary phases. Figure 6.3 represents the refined X-ray diffraction patterns of selected GFO compounds. Rietveld refinement of diffraction patterns was carried out by considering the monoclinic crystal symmetry with a C2/m space group. Pseudo Voigt peak shape function has been used to refine experimental diffraction patterns. In all of the refined patterns, simulated and experimental pattern intensities were fitted with a minimal differential curve. The obtained goodness of fit (χ^2) for three selected compounds is 1.61 ($x = 0.00$), 1.49 ($x = 0.20$), and 1.12 ($x = 0.30$). Hence, the structural refinement data reveals that, even at a higher concentration of Fe ($x = 0.30$), GFO compounds stabilize in monoclinic crystal symmetry, which is similar to the intrinsic Ga₂O₃. The refined unit cell parameters are provided in Table 6.2. Refined cell parameters indicate a small increment in unit cell volume associated with small ionic radii difference between Fe³⁺ and Ga³⁺. The atomic coordinates obtained from the refinement procedure are listed in Table 6.3.

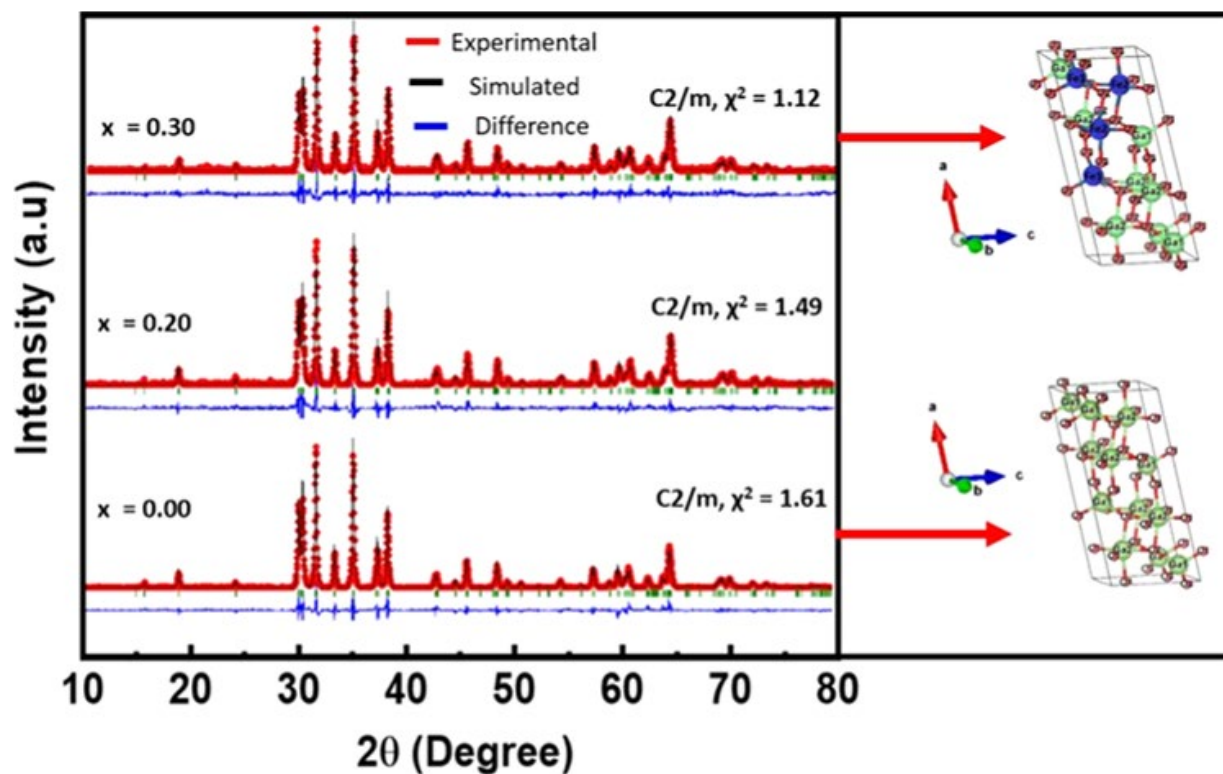


Figure 6.3: XRD patterns of GFO compounds. Rietveld structural refinement of XRD patterns is also presented. The experimental and calculated XRD patterns after the refinement are shown. Good agreement between the experimental and calculated XRD patterns can be noted.

Table 6.2: Unit Cell Parameters of GFO Compounds Obtained from Structural Refinement

Composition	Unit cell parameters				Unit cell Volume
	(x)	a (Å)	b (Å)	c (Å)	β (deg)
x = 0.00	12.2192	3.03951	5.80541	103.856	209.341
x = 0.20	12.2555	3.04532	5.81512	103.854	210.718
x = 0.30	12.2719	3.04791	5.82019	103.811	211.402

Table 6.3: Rietveld Structural Refinement Parameters Obtained for GFO Compounds

Fe concentration	Atoms	Atomic coordinates			U_{iso}
		X	Y	Z	
0.00	Ga1	0.09012	0.00000	0.79649	0.00162
	Ga2	0.15885	0.50000	0.30921	0.00471
	O1	0.15308	0.00000	0.10793	0.01013
	O2	0.17102	0.00000	0.56049	0.01013
	O3	-0.0079	0.50000	0.26514	0.01013
0.30	Ga1	0.0899	0.00000	0.7922(8)	1.00000
	Ga2	0.1577(3)	0.50000	0.3103(9)	0.01044
	O1	0.16051	0.00000	0.09246	-0.0828
	O2	0.17149	0.00000	0.56117	-0.0624
	O3	-0.00240	0.50000	0.25687	-0.0553
	Fe1	0.0899(3)	0.00000	0.7922(8)	0.00253
	Fe2	0.1577(3)	0.50000	0.3103(9)	0.00253

Figure 6.4 shows the SEM images of GFO compounds. Fe doping moderately changes the microstructure of intrinsic Ga_2O_3 . The rod-shaped particle morphology is observed in all the sintered samples. The rod-shaped morphology is the inherent characteristic of Ga_2O_3 , which is also reported by Shimura and Yoshida.⁶⁶ The particle coalescence can be seen in some cases predominantly in higher Fe content samples. The particle size reduction from 3.5 to $\sim 2.0 \mu m$ with increasing Fe content can be noticed. The particle size is measured by employing ImageJ software

analysis with at least 30 measurements per sample.¹⁰¹ An interesting phenomenon observed is the narrow particle size distribution with increasing Fe doping. Smooth and uniform distribution of the particles can be noticed in all images that is one of the characteristics of the high-temperature solid state synthesis process. Also, it is helpful in getting better final densification through the sintering process.

The rod-shaped particle feature seen throughout the microstructures of all the four GFO compounds correlates our observation with the XRD and lately with XANES studies, where it is mentioned that the doped Fe preferentially sits in the parental Ga sites by forming substitutional solid solutions and maintains the same crystal symmetry as of the intrinsic Ga_2O_3 . Thus, the salient characteristic features of the Ga_2O_3 can only be expected and seen in the SEM images rather than the features corresponding to the doped iron or iron oxide compounds. The apparent larger particles seen in the less iron containing samples might be due to the coalescence of the smaller particles. Integration and annexation phenomena between grains become obvious at the optimized processing condition. As a result of these, most of the voids and/or holes present in the material before were starting to disappear, paving the way for continuous grain growth.¹¹⁰ Atuchin et al. and Lim et al. have also observed similar behavior in Mo- and Ge-containing multicomponent oxide ceramics.^{57, 136} Fe doping in pure Ga_2O_3 might help in the formation of smaller nuclei and inhibit the grain growth during the synthesis and sintering process respectively. It might act as a kinetic barrier which prevents further grain displacement and segregation throughout the microstructure, thus reducing further grain growth.⁴⁷⁻⁴⁸ Although from the XRD and XANES studies it can be concluded that most of the doped Fe ions occupied the substitutional lattice positions of the parental Ga ions owing to their same ionic radii, some fractions can fit itself in the defect chemistry and/or in the interstitial lattice positions and impede the grain growth process.

Discussion on defects, specifically line or point defects in the limelight of SEM, is not totally possible because of the inherent low resolution of the SEM instruments. However, it is reliable to comment on the grain boundaries and qualitatively on the microscopic porosity of the micrographs. It is evident from the SEM images that some pores are present in each of the micrographs and it can be supported by our porosity calculations, though no typical characteristic grain boundary is omnipresent throughout the micrographs. From Table 6.1, it is obvious that the relative porosity percentage increases for the GFO compounds in comparison to the pure β - Ga_2O_3 by more or less 10%, but among the GFO compounds, it is almost constant ($\sim 36\%$). As mentioned before that, with increasing Fe concentration, the rod-shaped particles take narrow size distributions and probably this has helped to restrain the porosity level to a legitimate range. It can be assumed by the visual observation of the micrographs that higher Fe content GFO compounds have more compact structure. However, pure Ga_2O_3 micrograph has also evidenced a close-packed structure. This can be attributed to the Fe doping which might act as the grain growth inhibitor helped to obtain a narrow size distribution of the particles throughout the micrographs. In case of solid-state processing, porosity can act as a pinning phase and hinder grain growth. Liu and Patterson described elaborately on how porosity as a dispersed second phase in the main matrix can act as a grain growth inhibitor and help in achieving proper densification.¹³⁷ Porosity can be like interconnected channels or segregated upon separation based on the sintering conditions. It reduces the total energy of the grain boundary by getting attached to it and consequently slows down the grain boundary movement. Parameters such as effective surface area of pores, contact area between the pore and the grain boundary, grain boundary curvature, as well as the relative motion between the grain boundary and pore influence the above discussed phenomenon.¹³⁷

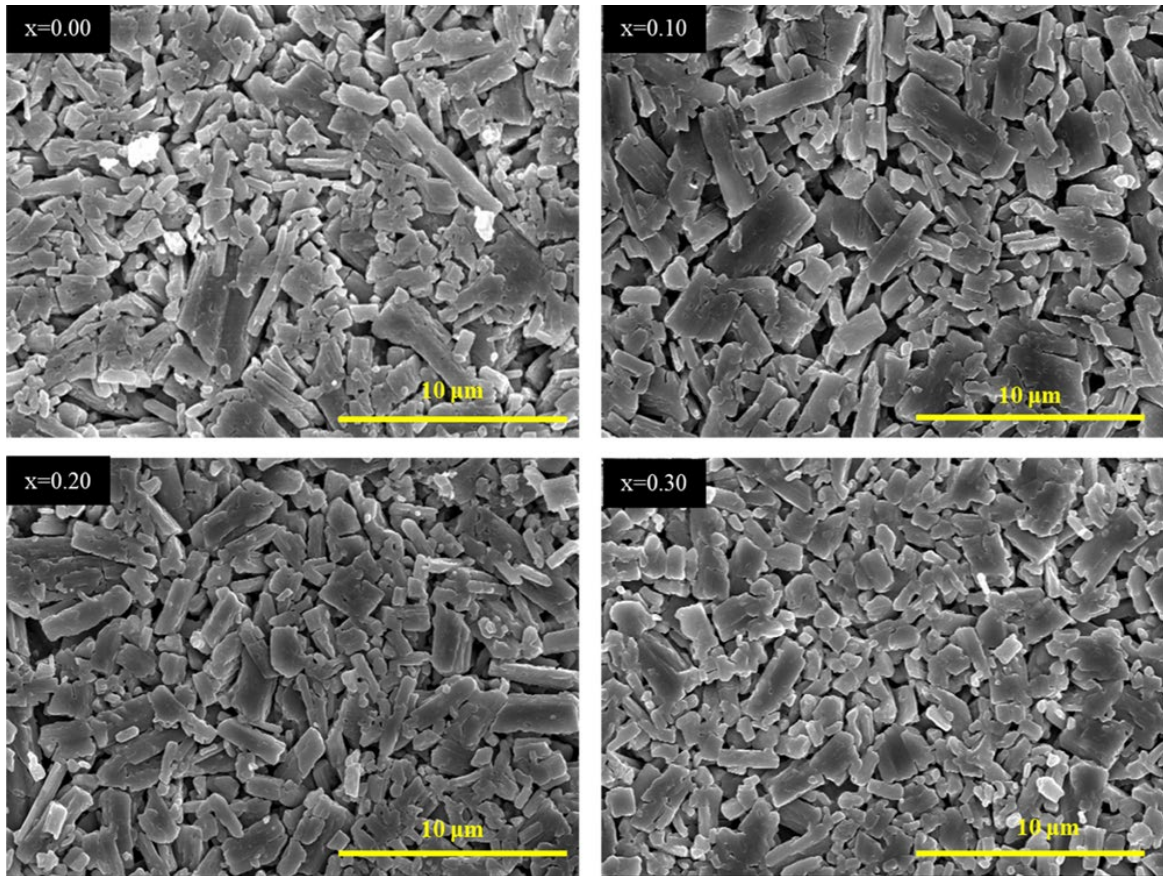


Figure 6.4: SEM data of $\text{Ga}_{(2-x)}\text{Fe}_x\text{O}_3$ compounds.

6.2 CHEMICAL ANALYSIS

6.2.1 Energy-Dispersive X-ray Spectrometry (EDS)

It is evident from the EDS data (Figure 6.5) that the dispersion of the constituent cations, that is, the ratio of Fe to Ga, is properly maintained closer to the theoretical atomic ratio despite the fact that the high temperature fabrication route is adopted to synthesize these samples. The EDS analysis of these samples confirms that, in sintered samples, the constituted elements are in stoichiometric proportion with respect to desired composition. We attribute this chemical quality of the GFO samples is due to proper mixing of the constituents during the preparation stages, precise maintenance of the furnace atmosphere by controlling the associated parameters, and exact densification obtained by employing the optimum firing conditions.⁷²

The elemental composition data collected from EDS are presented in Figure 6.5. It can be seen that the Ga content in GFO compounds decreases progressively with increasing Fe content. Figure 6.6 shows the elemental mapping of pure Ga_2O_3 and with highest Fe content ($x = 0.30$) GFO compound. It is evident from these images that the Fe-doped Ga_2O_3 compounds are homogeneous in terms of distribution of the principal constituent elements. The images report the increasing amount of iron which is noticeable from the image color contrast and the chemical homogeneity throughout the samples. Such chemical homogeneity is noted in all the GFO compounds.

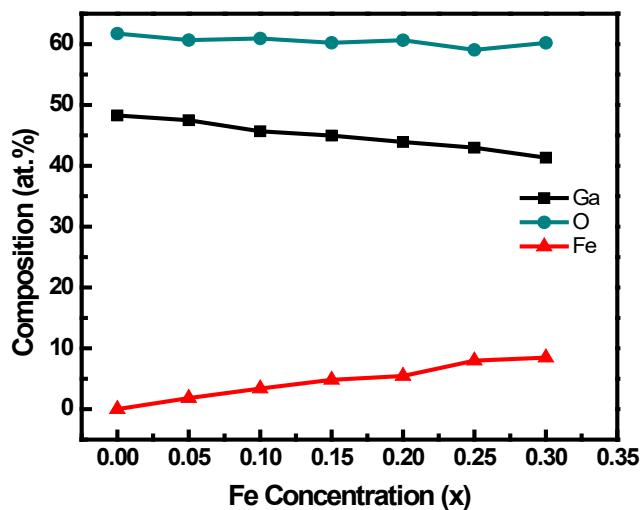


Figure 6.5: Atomic ratio of constituent elements of GFO compounds obtained from EDS.

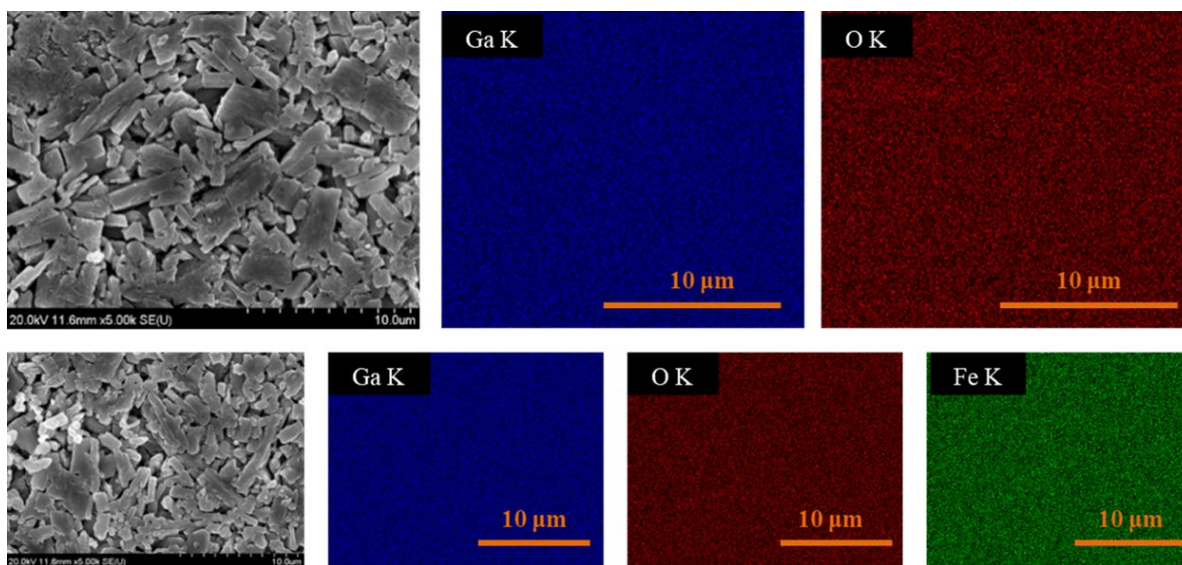


Figure 6.6: Elemental mapping of representative GFO compounds (Top $x=0.00$ and Bottom $x=0.30$, respectively). The data indicate the uniform distribution of the constituent elements.

6.2.2 X-ray Photoelectron Spectroscopy (XPS)

Being a surface sensitive characterization technique X-ray photoelectron spectroscopy (XPS) is employed to figure out the surface chemistry of the GFO compounds and the present chemical valence states of the constituent elements. The XPS survey scans of the selected compositions is represented in Figure 6.7. The survey scans indicate core level peaks of constituent elements such Ga, Fe, O, Ga LMM Auger peak, O KLL and C 1s. The C 1s peak, corresponding to the adventitious carbon adsorbed on the sample surface due to exposure to air during transferring the samples to the XPS load lock chamber. However, in surveys scans we could be able to observe Fe 2p peak in compounds with higher Fe concentration (in Figure 6.7 it is indicated as red dotted oval).

High resolution XPS spectra of Ga 2p and O 1s peaks are shown in Figure 6.8. The peak assignments and binding energy (BE) comparison are made following the NIST database. The Ga 2p region (Figure 6.8(a)) shows the high-resolution spectra of both Ga 2p_{3/2} and Ga 2p_{1/2} located

at ≈ 1117.6 and 1144.6 eV, respectively. The Ga $2p_{3/2}$ peak is located at a higher BE (1117.6 eV) in all the GFO samples compared to pure Ga metal which is located at 1117.0 eV.¹²² Compared to the Ga metallic state, the observed Ga $2p$ core level peaks exhibit a positive shift of 0.6 eV indicating that all the Ga exists in its oxide state. It has been widely reported that the Ga $2p$ core level peak exhibits a positive BE of 0.6 eV due to the redistribution of electronic charge leading to the formation of fully oxidized state (i.e., Ga^{3+}).⁶⁵ Thus, the Ga XPS data, which are consistent with the values reported for the Ga_2O_3 standard in the literature, confirms the existence of Ga ions in highest valance state.⁶⁵ The slight alteration in BE and peak intensity of Ga $2p$ peak with Fe doping may be due to the weakening of Ga-O bonds in Ga_2O_3 . This weakening causes a decrease in the electron density around the Ga ions.⁴²

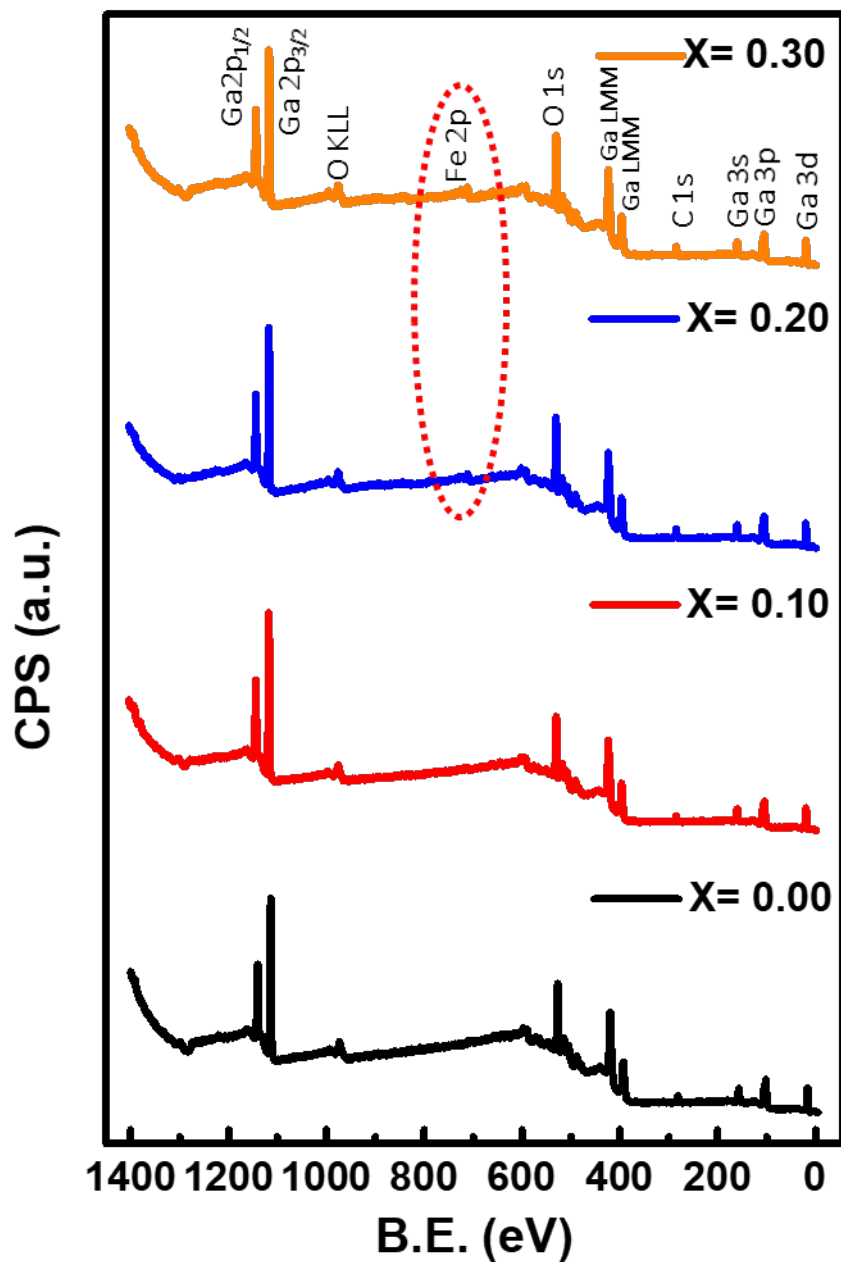


Figure 6.7: XPS survey scans of selected GFO compositions sintered at 1200 °C for 6 hrs.

The O 1s peak (Figure 6.8(b)) appears at a BE of 530.4 eV, which is a characteristic of Ga-O bond. This peak is very sensitive to the variation in chemical bonding.⁷³ It can be noted that this O 1s peak is not symmetric for all the GFO samples. The peak fitting of the O 1s core level peak results in at least two components representing the different chemical states or differently bonded oxygen. The most intense and main component, which is centered at a BE of 530.4 eV, is the

characteristic of oxygen bonded to Ga within the GFO compound. The O 1s peak for Fe₂O₃ and/or FeO becomes merged with the O 1s peak for Ga₂O₃ as most metal oxide peaks can be obtained in BE range of 530-531 eV. This has caused the O 1s peaks becoming slight broader in the Fe containing compounds. A second component, which appears as a shoulder contribution with minor intensity, is located at a higher BE of 532 eV. This component with minor intensity can be attributed to either carbonyl (oxygen bonded to carbon) or hydroxyl (oxygen bonded to hydrogen) groups, which were adsorbed onto the surface during sample handling.

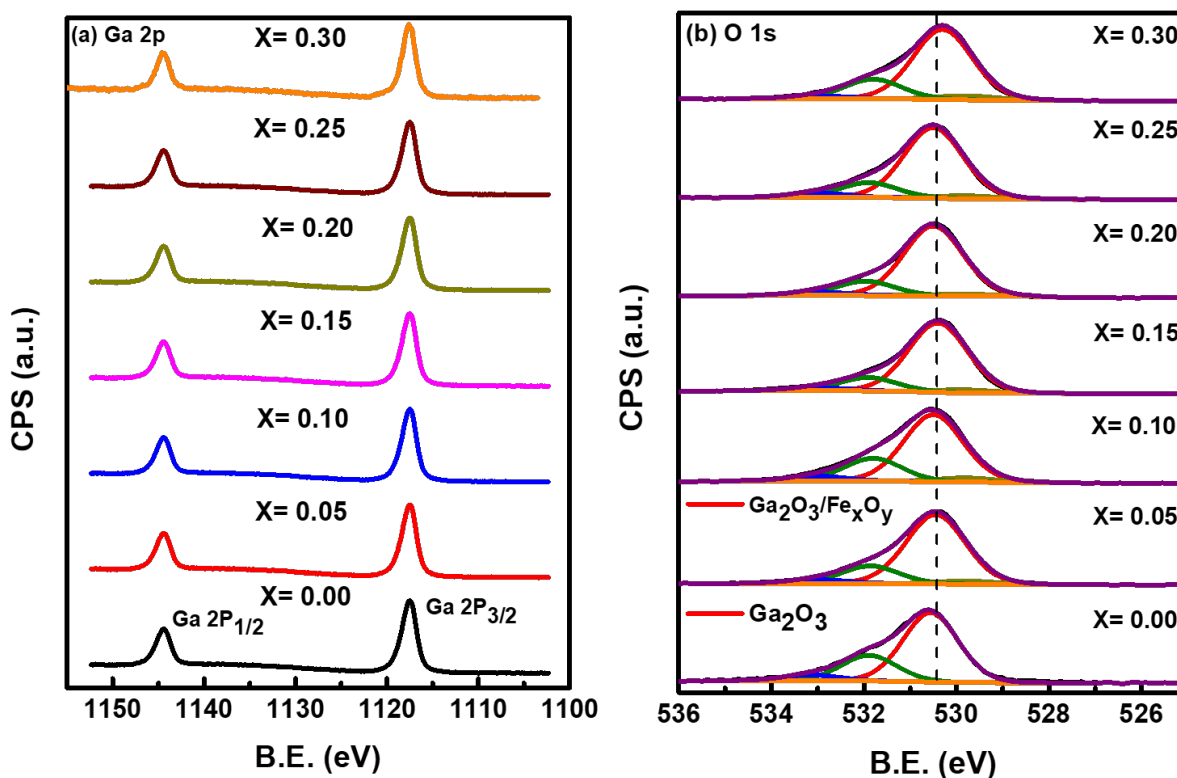


Figure 6.8: High resolution XPS spectra of GFO ($0.00 \leq x \leq 0.30$) compounds (a) Ga 2p, and (b) O 1s.

Figure 6.9 represents the high resolution XPS spectra of Fe 2p region. The deconvoluted spectra of Fe 2p_{3/2} peak clearly reveals that Fe exhibits mixed valance states (i.e., Fe³⁺ and Fe²⁺) in GFO samples with lower Fe content. However, Fe exhibits single valance state (i.e., Fe³⁺) in compounds with higher Fe content. It is mainly because of few reasons namely, considerable iron

content, fabrication method, furnace atmosphere, and to maintain the stoichiometry and charge neutrality. With increasing iron concentration in the GFO compounds intensity of Fe peak increases, whereas intensity of Ga peak decreases gradually. In addition, the shake-up satellite peak around 720 eV was observed in accordance with the literature, which is the characteristic feature of Fe^{3+} in $\alpha\text{-Fe}_2\text{O}_3$.¹³⁸⁻¹³⁹ However, the satellite peak is less pronounced in compounds with mixed valency state.

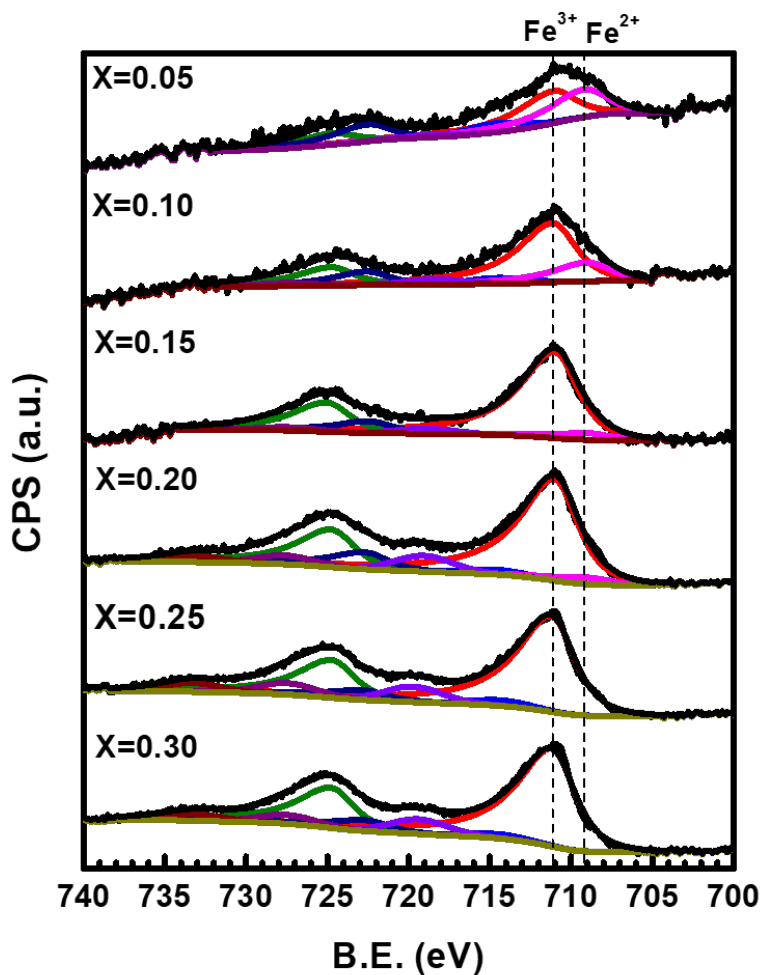


Figure 6.9: Deconvoluted high resolution XPS spectra of Fe 2p region of GFO compounds.

6.2.3 Local Structure and Bonding

The XANES data of GFO compounds with Ga_2O_3 structural figure are shown in Figure 6.10. The data shown in Figure 6.10(a)-(c) are the Ga L-edge, Fe L-edge, and O K-edge spectra, respectively, obtained as a function of variable Fe content. Figure 6.10(d) depicts the tetrahedral (Ga1) and octahedral (Ga2) coordination positions in the Ga_2O_3 structure. The as-received Ga_2O_3 and Fe_2O_3 powders were used as the reference samples. From this observation, it is evident that GFO compounds crystallized in beta monoclinic phase without any structural modification even at higher content of Fe. In intrinsic Ga_2O_3 , Ga^{3+} occupies both octahedral and tetrahedral lattice positions.⁶⁶ Ga L-edge spectra (Figure 6.10(a)) show two absorption peaks at around 1120 and 1128 eV. The first peak at 1120 eV arises due to octahedral coordination of Ga^{3+} (circled as O), whereas the second peak at 1128 eV is for tetrahedral coordination (circled as T). However, there is no considerable variation in Ga Ledge absorption spectra even at higher concentration of Fe, but small shift in absorption peaks attributed to change in bond length because of the slight ionic radii difference of Ga^{3+} and Fe^{3+} .

The O K-edge (Figure 6.10(b)) XANES spectra are different from the Ga L-edge XANES spectra for GFO compounds. Two peaks at around 535 and 542 eV can be observed for O K-edge, which is the characteristic of $\beta\text{-Ga}_2\text{O}_3$.⁷⁵ A broad diffused peak can be seen for Ga_2O_3 powder sample, which is absent in spectra of the GFO samples. This pre-edge feature can be attributed to the presence of $\epsilon\text{-Ga}_2\text{O}_3$, as commercial Ga_2O_3 powder generally is a mixture of $\epsilon\text{-Ga}_2\text{O}_3$ and $\beta\text{-Ga}_2\text{O}_3$.¹⁰⁶

The Fe L-edge (Figure 6.10(c)) spectra show one absorption band, that is, around 710 eV and the other absorption band, which is around 722 eV, is not shown here. The two absorption features are corresponding to L3-edge and L2-edge (circled in Figure 6.10(c) as for L3),

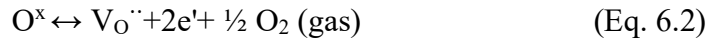
respectively, which are separated due to core-hole and 3d orbital interactions.⁷⁵ These absorption features are in good agreement with the literature of α -Fe₂O₃. Moreover, the splitting of L3-edge is due to crystal field splitting of 3d orbital interactions.^{75, 105}

The inherent defects in intrinsic β -Ga₂O₃ are the oxygen vacancies and Ga interstitials.^{39, 43} The defect concentration in intrinsic β -Ga₂O₃ is directly associated with the electron concentration, and a theoretical relation between the electron concentration and oxygen partial pressure has been established which is $[\acute{e}] \approx pO_2^{-1/4}$, where, $[\acute{e}]$ denotes the electron concentration and pO_2 indicates the partial pressure of oxygen.⁴³ Intrinsic gallium oxide has three different oxygen configurations and these configurations vary for different charged states. While one of the oxygen atoms is arranged in tetragonal configuration, the rests of the three are coordinated trigonally. Gallium also has two configurations namely tetrahedral and octahedral in β -Ga₂O₃ crystal system.^{43, 140} It is not clear that which site is more energetically favorable though some researchers favor the tetragonal site as the energetically lower site for maintaining the crystal symmetry.^{39, 141} Inherent defect concentration is so small in intrinsic β -Ga₂O₃ that introducing small amounts of foreign element can alter the defect chemistry.

It is argued that the negative charge defects have higher formation energy than the positive charge defects. The formation energy of the oxygen vacancies is lower than the gallium interstitials but often oxygen vacancies are considered as the deep donors (i.e., deep transition levels) and responsible for the n-type conductivity whereas other researchers cited that the charge carrying ability of the intrinsic β -Ga₂O₃ oxide is solely due to the defect complexes of hydrogen atom which is a shallow donor.^{140, 142} Being a direct band gap material, band structure of β -Ga₂O₃ exhibits a flat valence band, indicating a high concentration of holes which leads to the low hole mobility,

and this self-localization of holes became the main barrier in the fabrication of p-type β -Ga₂O₃ by doping foreign elements.¹⁴²

The formation energy of oxygen vacancies strongly depends on the chemical potential of oxygen and the fermi energy. The chemical potential of oxygen is not a fixed value and changes with the different ambient atmospheric conditions. The oxygen vacancies become the defects with lowest formation energy under oxygen deficient conditions and vice-versa. Defects associated with oxygen vacancies are more stable in their fully charged states.^{140, 142} For low monoclinic symmetry compounds, a large number of different point defects (e.g., Frenkel, anti-Frenkel and Schottky) have to be considered.¹⁴⁰ The associated equations for the inherent β -Ga₂O₃ defects are as follows:



where, Ga^x denotes the neutral Ga positions in Ga₂O₃ crystal, V_{Ga}^{'''} denotes the gallium vacancy, Ga_i^{'''} denotes the gallium interstitials, O^x denotes the neutral oxygen positions, V_O^{''} denotes the oxygen vacancy and e' denotes the electron. These defects play very significant role under high temperature conditions in association with lattice vibration and phonon dispersion. It has been found as a general behaviour that the negatively charged defects such as V_{Ga}^{'''} and O_i^{''} exhibited large positive relaxation volumes, whereas the positively charged defects such as Ga_i^{'''} and V_O^{''} exhibited negative and smaller relaxation volumes.¹⁴³

Density functional Theory (DFT) provides the formation energy of oxygen defects in β -Ga₂O₃ with a charge state is given by,^{142, 144}

$$E^f[V_O^q] = E_{tot}[V_O^q] - E_{tot}[Ga_2O_3] + \mu_O + q\epsilon_f \quad (\text{Eq. 6.3})$$

where, $E_{tot}[V_O^q]$ and $E_{tot}[Ga_2O_3]$ represent total energy of the supercell containing a vacancy in charge state q, and perfect crystal in the same unit cell, μ_O is chemical potential and ϵ_f fermi level

measured from top of valance band. According to DFT calculations, defect formation energies varies with fermi level; hence when fermi level is close to valance band, charged oxygen defects are dominant whereas, neutral defects are dominant as fermi level is moving up.

In GFO compounds, Fe does not form any intrinsic defect by itself, due to their close ionic radii on octahedral and tetrahedral sites and isovalent electron configuration; but Fe ions can also sit into the same interstitial defect sites as Ga^{3+} . So, this will maintain the almost same inherent defect structure of the intrinsic $\beta\text{-Ga}_2\text{O}_3$. Recent theoretical study reveals that Fe substituted on the octahedral Ga site (Fe_{GaII}) has high formation energy, whereas Fe substituted at tetrahedral site (Fe_{GaI}) exhibits a low formation energy. In both configurations, Fe acts as a deep acceptor level below the conduction band maximum.¹⁴⁴ Doping with transition metal specially Fe can introduce some new characteristic features such as spintronics, magnetic properties and optoelectronic applications by altering the band gap which is currently being studied.

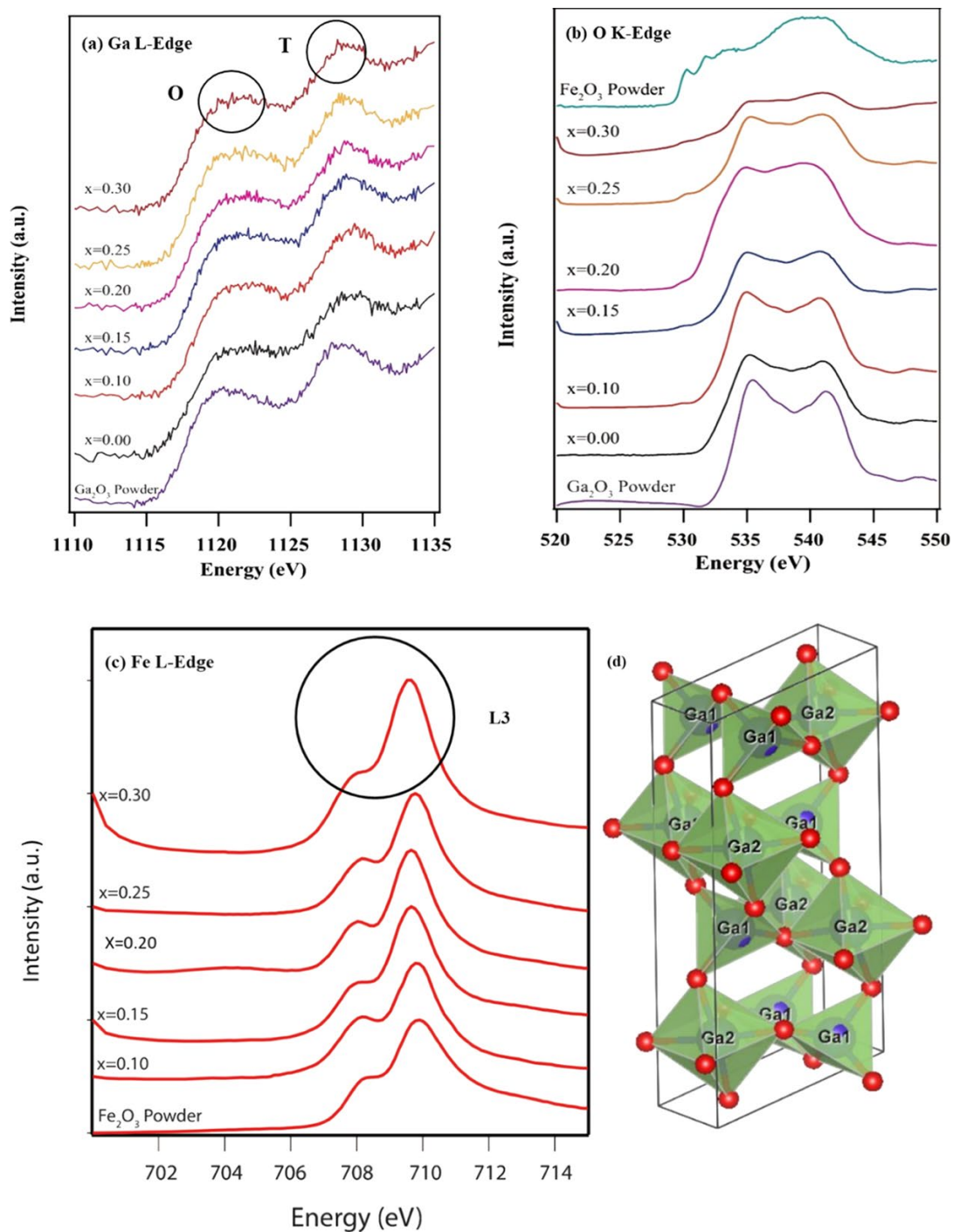


Figure 6.10: XANES of (a) Ga L-edge, (b) O K-edge, (c) Fe L-edge, and (d) representative crystal structure of Ga₂O₃ with tetrahedral and octahedral coordination positions. Ga1 and Ga2 denote the tetrahedral and octahedral lattice sites in pure Ga₂O₃ compound, respectively. Oxygen atoms at their respective positions are represented by red circles.

6.3 DIELECTRIC PROPERTIES

Figure 6.11 shows the real part (ϵ') of the dielectric constant (Figure 6.11(a)) and the dissipation factor ($\tan \delta$) (Figure 6.11(b)) as a function of frequency of the composition variation GFO compounds. The dispersion behavior of real part of the dielectric constant is the characteristic of traditional dielectric oxides. Dielectric materials exhibit high dielectric constant values at low frequencies, gradually decreases with increasing frequency. High dielectric constant at low frequencies is attributed to the extrinsic (space charge, grains, and grain boundaries) and the intrinsic contribution (ionic, dipolar, and electronic) to the dielectric polarization. Decrement of dielectric constant with increasing frequency is due to relaxation of extrinsic factors. However, predominantly, high dielectric constant at low frequencies might be attributed to the Maxwell-Wagner type of interfacial polarization.¹¹⁸

Dielectric factor ($\tan \delta$) represents the measurement of energy loss and is expressed as $\tan \delta = \epsilon''/\epsilon'$, where angle δ is the phase difference between applied electric field and current and ϵ'' is the imaginary part of the complex dielectric constant. Frequency dependence has profound influence on dielectric loss values.¹⁴⁵⁻¹⁴⁶ When polarization lags behind the applied alternating field, dielectric loss occurs. This mainly arises due to the influence of grain boundaries, impurities (e.g., doping), and crystalline defects. Density of ceramic materials also plays a key role in manipulating dielectric loss. The low-density ceramic material has high porosity which is responsible for low dielectric constant and higher loss. As the calculated relative porosity is quite similar for all the doped compounds, then it can be inferred that the role of defect chemistry upon doping is playing a significant role in determining the trend of dielectric loss data. Though it is confirmed from the XRD and XANES studies that most of the doped Fe occupied the parental lattice positions, but some of them can occupy the interstitial positions or the other defect sites.

Also, it is important to consider that the inherent defects for the intrinsic Ga_2O_3 are the interstitial Ga ions and O_2 vacancies. It is quite possible that for some specific doping concentration, the defect chemistry changes in the GFO compounds, which gives inconsistent dielectric loss data. The formation of the low dielectric phases and detachment of the loosely bound charges from the surface can also be the reasons. The dielectric loss for those particular GFO compounds is slightly higher in the low frequency region than the remaining compounds, but with increasing frequency, it can be observed that the loss components decrease exponentially as like the other compounds and tend to zero. With increasing iron doping (i.e., increasing impurity level) in Ga_2O_3 decreases this jumping tendency. This might be due to two reasons: first, due to the overpopulated charge carriers which lead to the strong interaction with the lattice and, secondly, due to the absence of major polarizing factors. It is evident from the graph (Figure 6.11(b)) that dielectric loss decreases with increasing frequency.

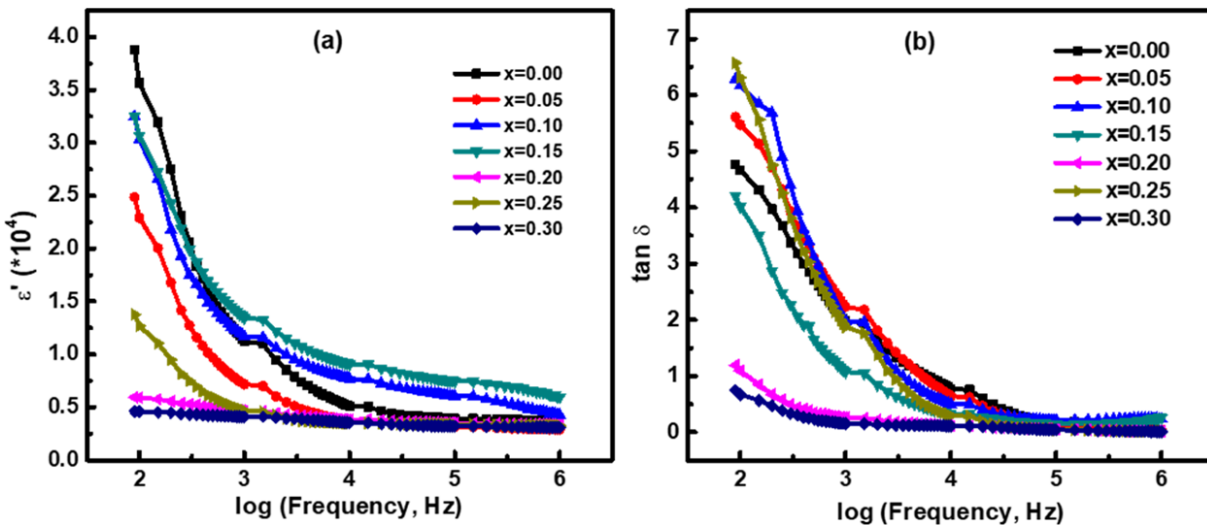


Figure 6.11: (a) Frequency-dependent real part of dielectric constant, and (b) frequency dependent dissipation factor ($\tan \delta$) of GFO compounds.

The modified Debye's model was used to simulate the experimentally measured dielectric constant because more than one ion (Ga^{3+} , Fe^{3+} , and O^{2-}) are involved in the relaxation process. Using this model, the observed dispersion in ϵ' is modeled according to eq. 5.3. Figure 6.12

compares the experimental and simulated values of frequency dependent real part of the dielectric constant (ϵ'). With the help of the Cole-Cole plot,¹⁴⁶ the spreading factor for GFO compounds was obtained. However, in our modified method, real part of the dielectric constant was considered rather than the complex part, and the graph shown in Figure 6.13 was plotted for $\ln[(\epsilon'_{\omega} - \epsilon'_{\infty}) / (\epsilon'_{\omega} - \epsilon'_{\infty})]$ versus $\ln \omega$ for all the compositions. A linear regression has been performed to calculate the slope of the lines and spreading factors “ α ” was obtained from these slopes of Figure 6.13. The estimated values of τ and α were used to correlate the experimentally obtained values of ϵ' with the calculated values by fitting the model, eq. 5.3, and the result is shown in Figure 6.12. It is evident in Figure 6.12 that the experimental and the calculated data are in good agreement that confirms the above-mentioned dielectric relaxation behavior of the samples obeying the modified Debye model.

We believe that, with increasing Fe concentration, there is a strong interaction between lattice and charge carriers. Doping Fe into Ga_2O_3 increases the interionic distance, as evidenced in structural characterization. This characteristic feature is also evident in dielectric properties, where the higher values of spreading factor and mean relaxation time with increasing Fe concentration account for increased interionic distance. Because of the higher bond length and/or interionic distance, electron hopping distance increases for Fe-doped Ga_2O_3 compounds, which, in turn, increases the α and τ values in comparison to those of intrinsic Ga_2O_3 . The spreading factor values for $x= 0.00$ and $x= 0.30$ are 0.579 and 0.602, respectively. The relaxation time and the spreading factor values for the remaining compounds are calculated for the sake of simulation but are not mentioned here. The enhanced dielectric constant of some GFO compounds in comparison to Ga_2O_3 is mainly due to the extra sources of polarization because of Fe doping. This theory can be explained by the hopping of electrons between several ions that is Fe^{2+} , Fe^{3+} , Ga^{3+} and O^{2-} . This hopping of electrons facilitates the local displacement of electrons in the direction of the applied field. The dipole of the electrons thus produced orientation polarization by aligning themselves in the direction of the applied field, which subsequently increased the dielectric constant values. Iron inclusion in the Ga_2O_3 crystal system is also responsible for the rise in atomic polarizability and

subsequent increment in dielectric constant. At the same time, charge accumulation at the grain boundary increased the interfacial polarization and the dielectric constant.

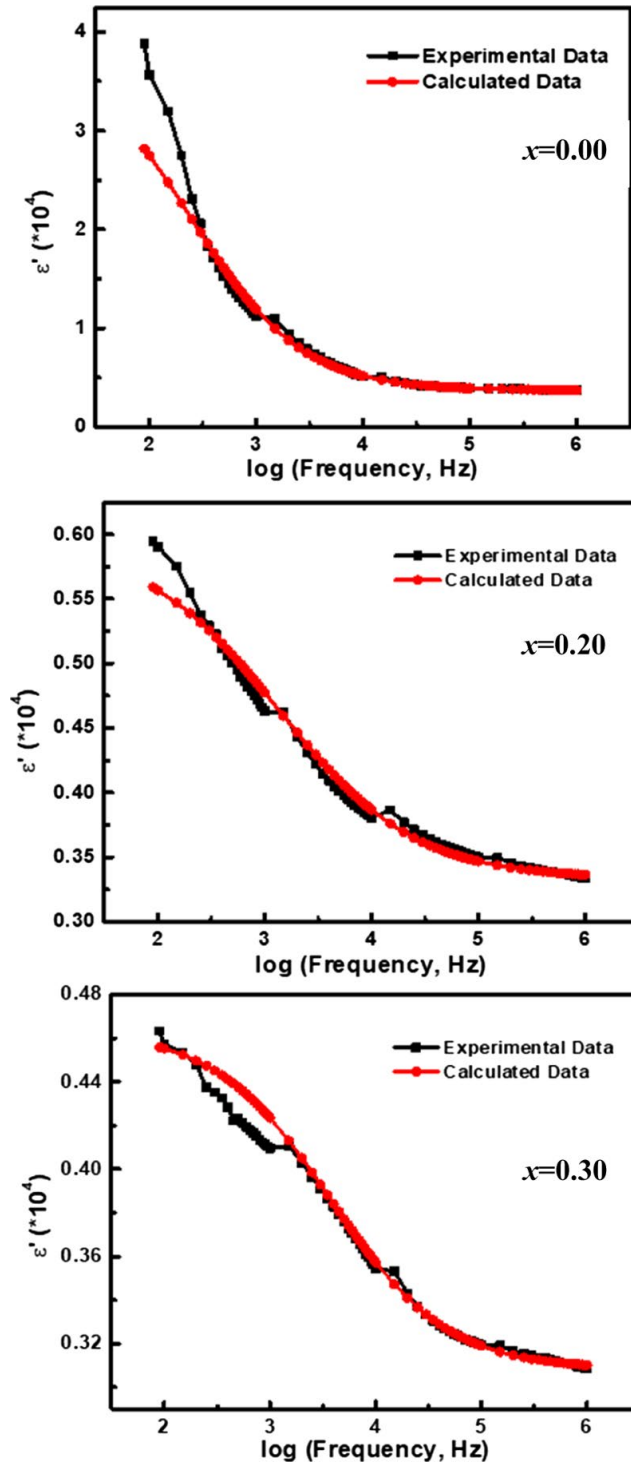


Figure 6.12: Variation of real part of the dielectric constant of GFO compounds with frequency. The dispersion behavior in all these plots fits to the modified Debye function.

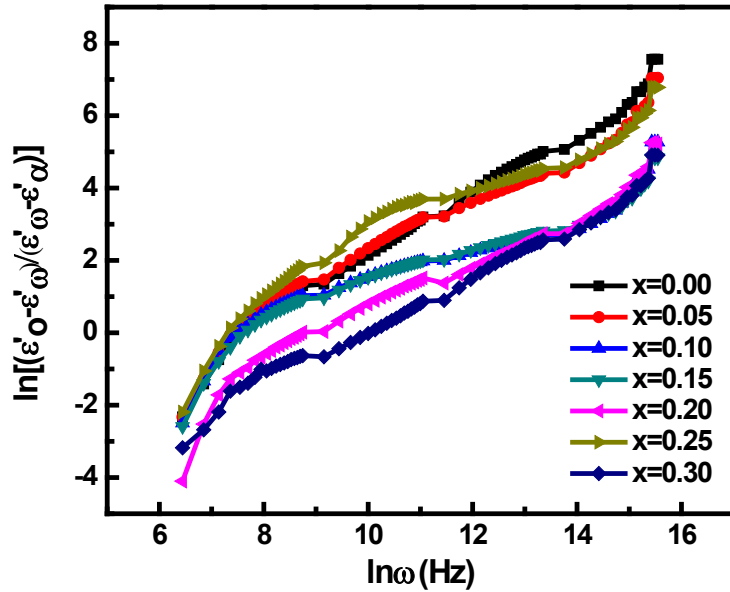


Figure 6.13: Variation of $\ln[(\epsilon'_0 - \epsilon'_\omega)/(\epsilon'_\omega - \epsilon'_\infty)]$ vs $\ln \omega$ for GFO compounds at room temperature.

Temperature dependence of the dielectric behavior of GFO compounds has been studied in order to further understand the effect of Fe incorporation on the properties of intrinsic Ga_2O_3 . The temperature-dependent plots of ϵ' for GFO compounds are presented in Figure 6.14. The data were recorded at variable frequencies in the range of 1 kHz to 1 MHz. For all the GFO compounds, dielectric constant increases monotonically with temperature at all frequencies. However, the rate of increment is higher for the lower frequencies. At the low frequency range, all types of polarizing factors, such as ionic, electronic, dipolar, and space charge, contribute to the larger values of dielectric constant. At higher frequency, ϵ' reaches a constant value. This might be due to the fact that at higher frequency, polarization decreases as electron hopping cannot follow the fast-changing alternating current after a certain frequency level of the externally applied field. This is the reason why ϵ' value is almost constant for 1 MHz (Figure 6.14) throughout the whole

temperature range. Predominantly higher dielectric constant values observed in GFO compounds at 1 kHz are attributed to the electrode material interface polarization.

Low-temperature dielectric relaxation mainly occurs due to the influence of charge carriers contributing to the interfacial polarization. At higher temperature and with increasing dopant concentration, a strong interaction between the lattice and the charge carrier occurs and due to the formation of highly insulating grain boundaries, single relaxation behavior can be noticed. Also, space charge polarization at the grain boundaries assisted by high temperature oxygen vacancies contributes to the dielectric relaxation behavior at high temperature.¹³³ Dielectric relaxation mechanism of a ceramic material depends on sensitive factors such as microstructural and atomic defects (e.g., porosity, Schottky and Frenkel defects), temperature, associated electro-magnetic field, ionic substitution, relative percentage of grain and grain boundary, and so on. Incorporation of iron in pure β -Ga₂O₃ has slightly increased the interionic distance. Because of the higher bond length and/or interionic distance, electron hopping distances increase for GFO compounds.

Figure 6.15 illustrates the loss tangent versus temperature plot as a function of frequency for GFO compounds at different frequencies. It can be observed that $\tan \delta$ increases with the increasing temperature and obtains maxima. Both temperature and frequency have profound influence on dielectric loss values.^{118, 145} Pure β -Ga₂O₃ exhibits low dielectric losses at different frequencies compared to the Fe-doped Ga₂O₃ compounds. Dielectric loss increases gradually with increasing temperature up to 350 °C in all the studied compositions at different frequencies. However, beyond 350 °C, dielectric loss increases drastically, and it is more predominant at low frequency (1 kHz) in the all the compositions. Dielectric loss also increases with increasing Fe concentration. The high dielectric losses at higher temperatures attributed to (a) hopping of

thermally trapped electrons between different lattice sites and (b) thermally activated motion of oxygen vacancies.

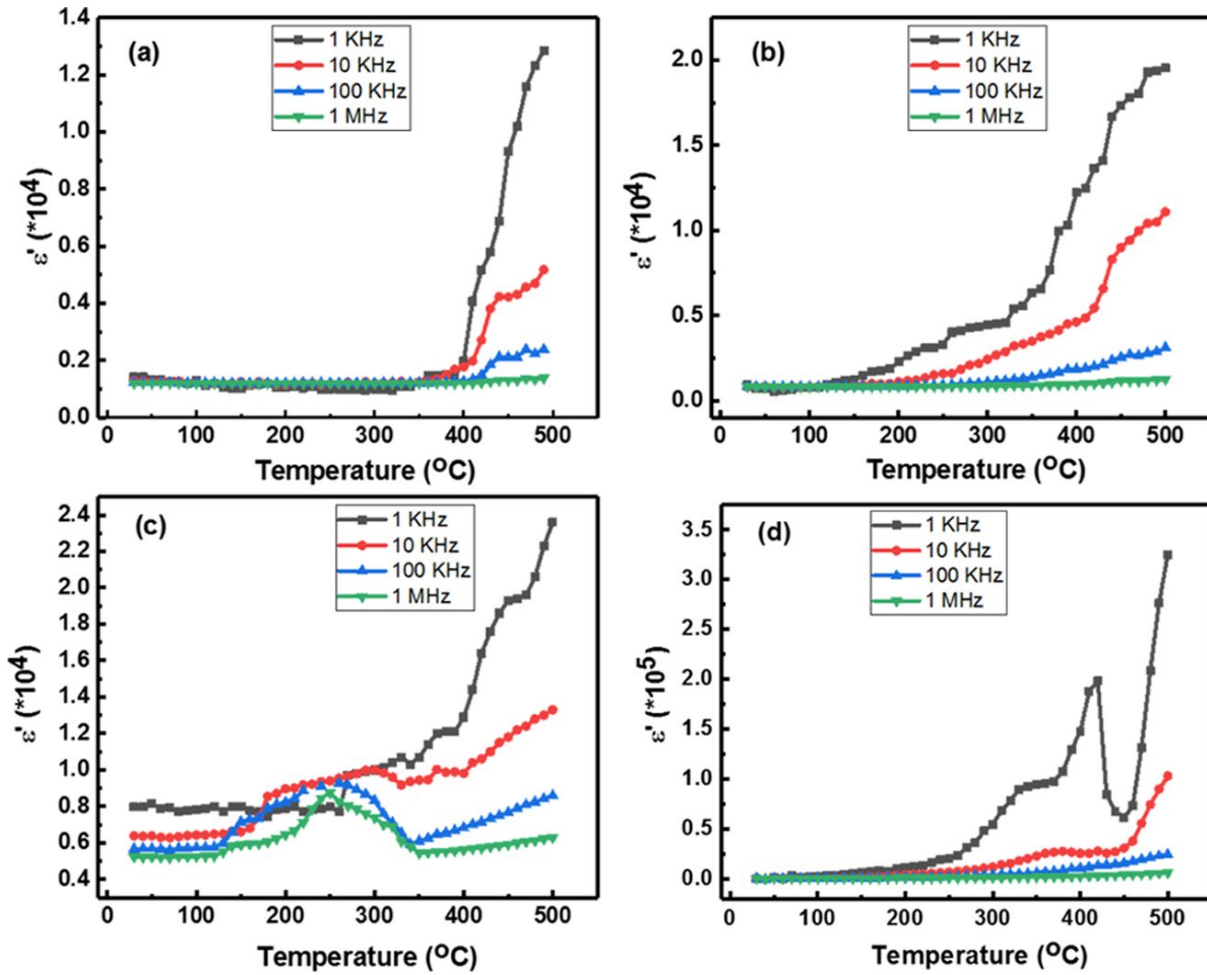


Figure 6.14: Variation of dielectric constant (ϵ') with temperature at different frequencies of the GFO compounds. (a) $x = 0.00$, (b) $x = 0.15$, (c) $x = 0.20$, and (d) $x = 0.30$.

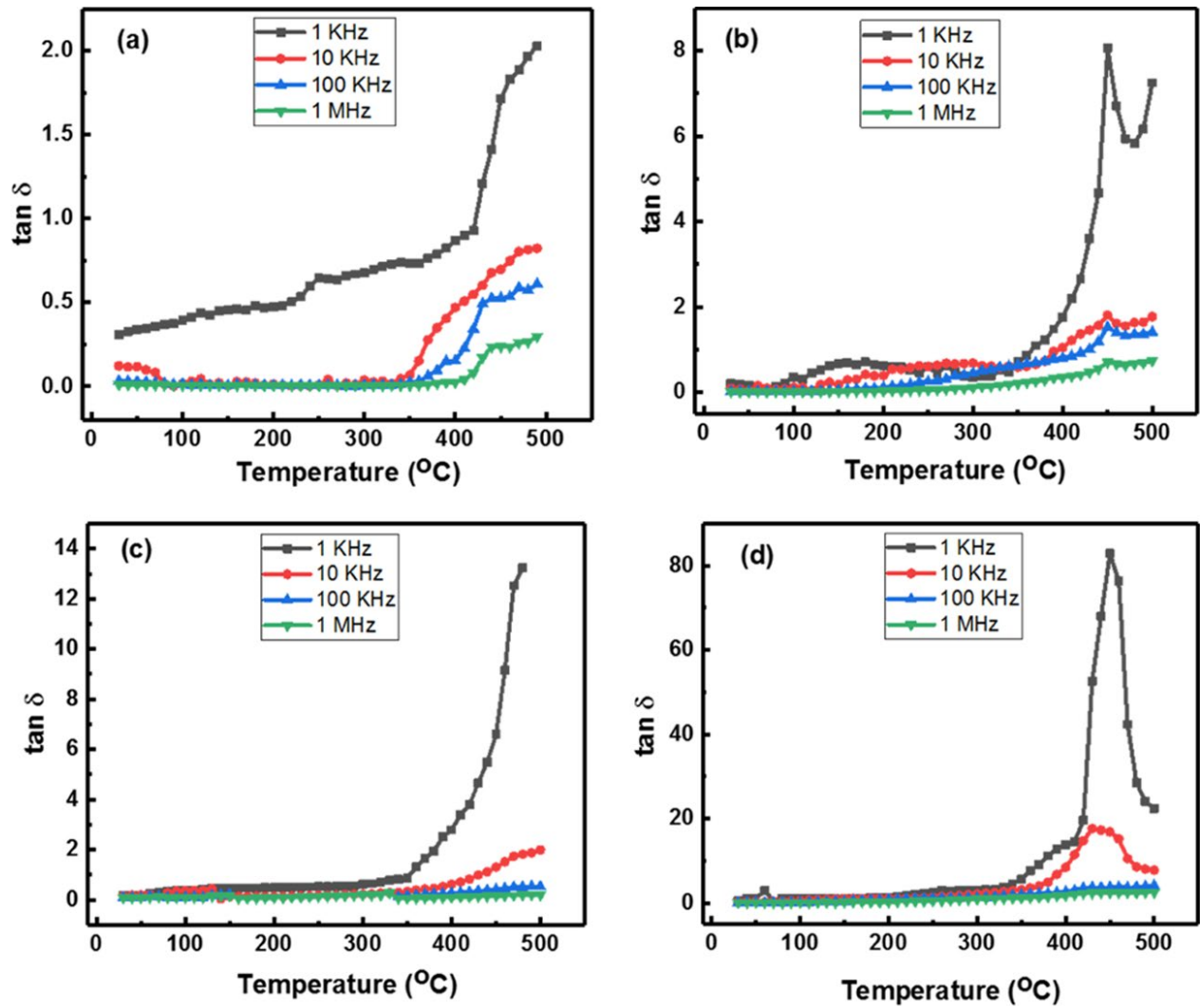


Figure 6.15: Variation of $\tan \delta$ with temperature at different frequencies of the GFO compounds. (a) $x = 0.00$, (b) $x = 0.15$, (c) $x = 0.20$, and (d) $x = 0.30$.

Chapter 7: Applications

7.1 OPTICAL

The optical absorption spectra and associated data analyses of GFO compounds are presented in Figure 7.1. It is evident from the optical absorption spectra (Figure 7.1(a)) that the Fe doping induces a change in the absorption edge. From the cutoff wavelengths of all of the compounds, it is evident that the GFO compounds with Fe concentration $x \leq 0.10$ exhibit the absorption edge in the UV regions (≤ 400 nm), whereas compounds with Fe concentration $x \geq 0.15$ exhibit the absorption edge in the visible region (≥ 400 nm). As the concentration of Fe increases, the absorption edge shifts from the UV to visible region, which is referred to as “red shift”. In all of the GFO compounds, the progressive shift in the absorption edge is clearly noted. Moreover, a small absorption edge at ≈ 450 nm was found in Fe-substituted compounds (indicated with a red oval in Figure 7.1(a)). Such small absorption band is associated with a double excitation process of Fe^{3+} - Fe^{3+} and is due to transitions from ${}^6\text{A}_1(\text{S}) + {}^6\text{A}_2(\text{S})$ to ${}^4\text{T}_1(\text{G}) + {}^4\text{T}_2(\text{G})$.¹⁴⁷⁻¹⁴⁹ Figure 7.1(b) represents the enlarged profile of Fe-induced double-excitation process. The inset in Figure 7.1(b) represents the relative intensity of Fe-induced absorption edge associated with a double excitation process with Fe concentration. From the inset figure, it is evident that the relative intensity of Fe peak increases with increasing Fe content, as expected.

Figure 7.2 shows the variation in the band gap of GFO compounds with Fe concentration. The determination of the cut-off wavelength to calculate the band gap is presented in the inset of Figure 7.2. The band gap of intrinsic Ga_2O_3 is 4.56 (± 0.01) eV, which is in good agreement with that reported in the literature.¹⁵⁰ However, Fe incorporation into Ga_2O_3 considerably decreases the band gap even at a very initial concentration. At the very first step of Fe, i.e., $x = 0.05$, the GFO compounds experience a significant reduction in band gap from 4.56 to 3.34 eV (Figure 7.2).

However, further doping of Fe still induces the band gap narrowing but at a much lower rate. Overall, the band gap finally reduces to 2.95 (± 0.01) eV when Fe content is increased to $x = 0.30$. While such a reduction in band gap is also noted in Cu-, W-, Mo-, and Ti-doped Ga_2O_3 , the red shift observed in these GFO compounds even for a lower content of Fe is very significant.

The chemistry behind the observed wide-range spectral selectivity and red-shift band gap in GFO compounds can be explained as follows. Based on the XRD data and refinement procedure, the substitutional nature of Fe in Ga_2O_3 is evident for the entire range of dopant composition. This can be easily understood from the considerations of the Shannon ionic radii of Ga and Fe. The ionic radii of Ga and Fe are in excellent close match with each other: Ga^{3+} , 0.62 Å (octahedral coordination) and 0.47 Å (tetrahedral coordination); and Fe^{3+} , 0.64 Å (octahedral coordination) and 0.49 Å (tetrahedral coordination).¹²⁰ Therefore, Fe^{3+} can be substituted in the Ga site, which can replace Ga^{3+} from both octahedral and tetrahedral positions in stoichiometric proportion. Thus, no perturbation to the parent crystal structure, i.e., monoclinic structure of $\beta\text{-Ga}_2\text{O}_3$, is seen even at the highest concentration ($x = 0.30$) of Fe doping into Ga_2O_3 . Under such isostructural configuration, electronic structural changes occur due to the Fe substituting for Ga. Thus, the substantial red shift observed in band gap can be explained based on the sp-d exchange interaction between valence band electrons and localized d electrons of Fe in Ga_2O_3 . The sp-d exchange interactions led to positive and negative corrections to valence and conduction bands; as a consequence, band gap narrowing occurs in the systems with sp-d exchange interactions.¹⁵¹⁻¹⁵³ In the present case, the outer-most electron configurations of Ga^{3+} and Fe^{3+} are $3d^{10}$ and $3d^5$, respectively. Therefore, in intrinsic Ga_2O_3 , 3d electrons do not involve in hybridization, whereas in the case of Fe-doped Ga_2O_3 compounds, $3d^5$ electrons involve in hybridization with O p-orbitals. Owing to this, there is a strong s-d and p-d exchange interactions present in GFO

compounds, which leads to abrupt band gap narrowing. These interactions and, hence, the spectral selectivity and band gap can be tuned by carefully controlling the Fe content and, hence, the dopant chemistry in GFO compounds.

Figure 7.3 represents the schematic energy diagram of intrinsic β -Ga₂O₃ and Fe³⁺ doped Ga₂O₃. The figure clearly shows positive and negative corrections to the valance band and conduction band due to sp-d exchange interaction in Fe³⁺ doped Ga₂O₃, associated band gap narrowing. As explained, in the case of intrinsic β -Ga₂O₃, valance band edge is dominated by O 2p orbitals and conduction band is dominated by Ga 4s orbitals, whereas in the case of Fe³⁺ doped compounds, valance band edge is dominated by O 2p orbitals and conduction band edge is dominated by Ga 4s and Fe 3d in contrast to intrinsic β -Ga₂O₃. The sp-d exchange originates in Fe-doped compounds due to the contribution of Fe 3d electrons to conduction band.

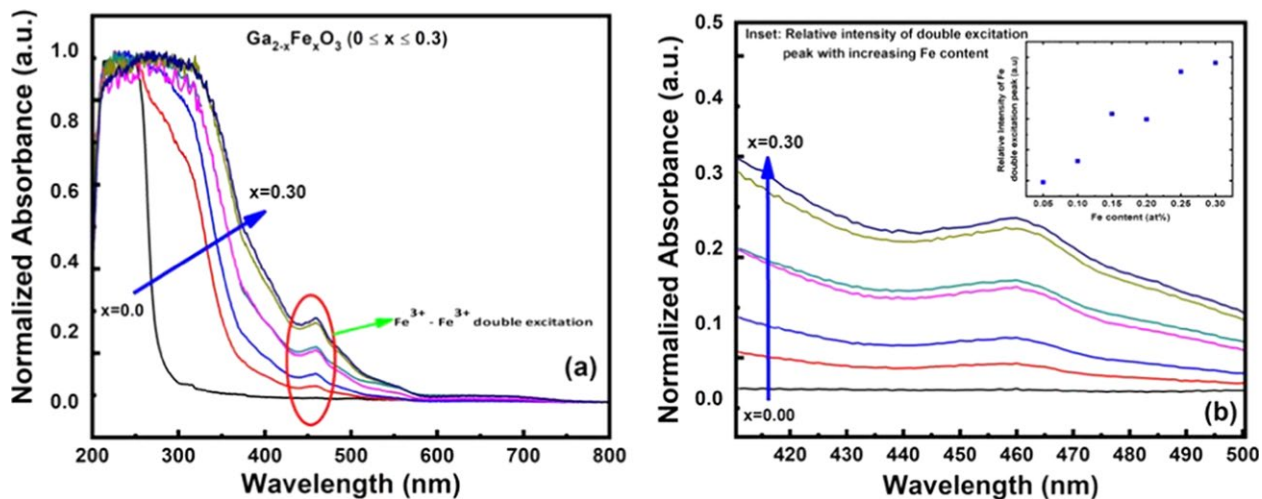


Figure 7.1: (a) Optical absorption spectra of GFO. (b) Enlarged profile representing the intensity variation of peak associated with Fe³⁺-Fe³⁺ double-excitation process (Inset: relative intensity of Fe-induced double-excitation edge vs Fe content).

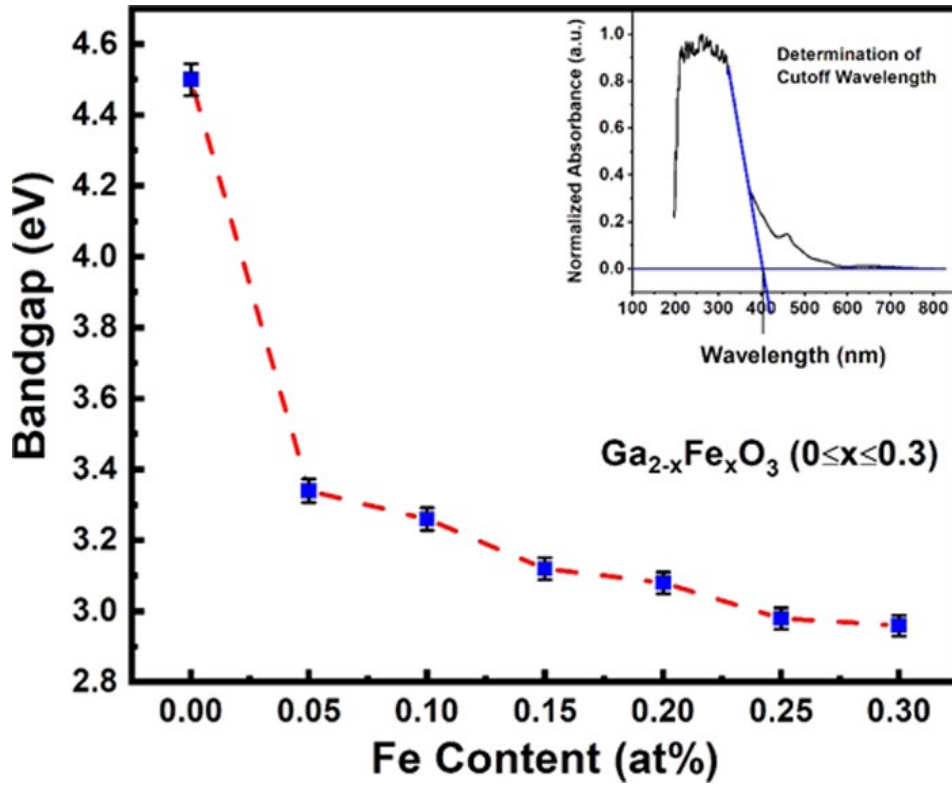


Figure 7.2: Band gap variation with Fe content. Significant reduction in band gap in GFO compounds is evident.

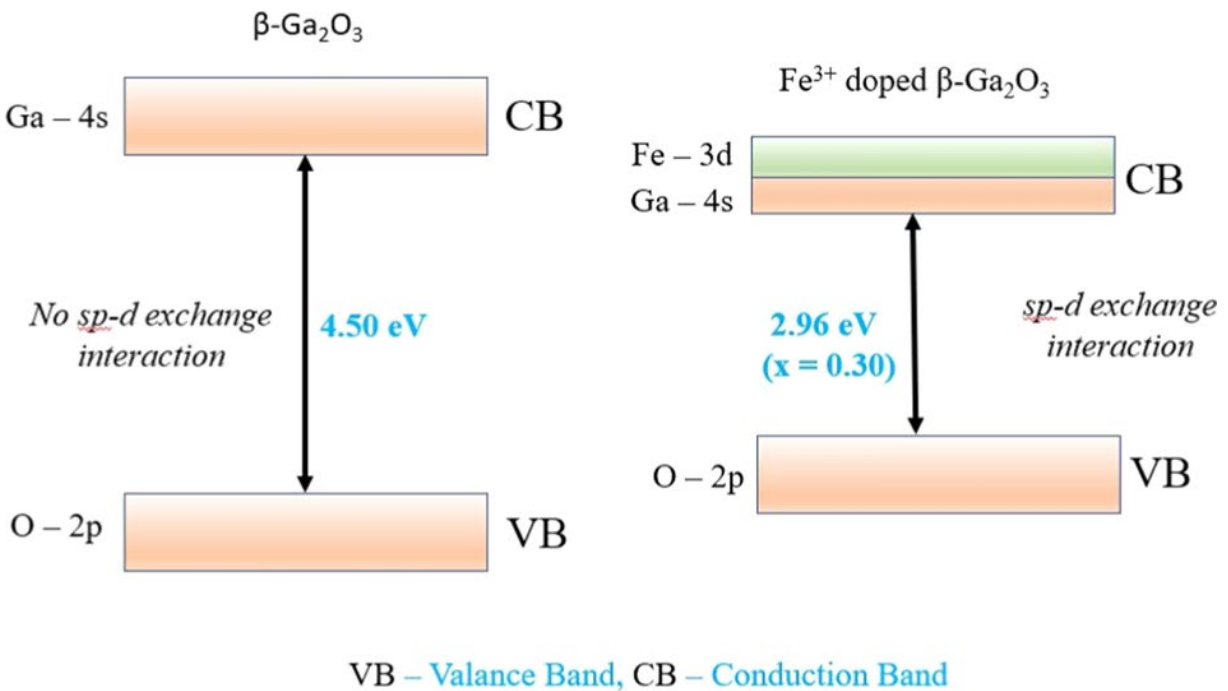


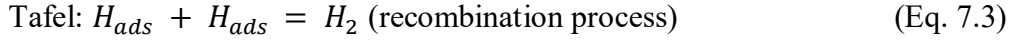
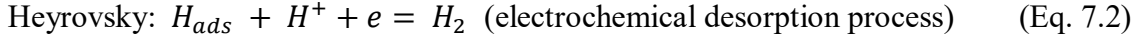
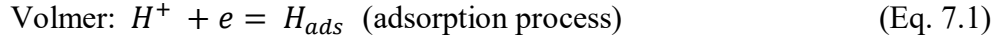
Figure 7.3: Schematic energy diagram of intrinsic and Fe-doped Ga_2O_3 .

7.2: ELECTROCATALYTIC ACTIVITY

After confirming that Fe doping in GFO can intimately modulate its optical properties and band gap, we explored its potential to elicit unconventional properties in Ga_2O_3 . While the use of Ga_2O_3 for lasers,¹⁵⁴ phosphors,¹⁵⁵ etc. is being explored in detail, its potential as a catalyst is comparatively less explored. Recent studies indicate that Ga_2O_3 has considerable utility as photocatalysts for the creation of H_2 fuel, especially through water splitting.¹⁵⁶ However, owing to the large band gap of Ga_2O_3 that makes electrocatalytic reactions tedious, the applicability of Ga_2O_3 -based materials toward electrocatalytic processes remained unexplored. Optical band-gap analysis of GFO compounds reveals that there is significant reduction in optical band gap, which could also impact its electrocatalytic characteristics.

Figure 7.4 illustrates the electrocatalytic analysis of intrinsic Ga_2O_3 and two Fe doped Ga_2O_3 samples ($x= 0.15$ and 0.30 , respectively) employing HER as the model reaction. To the best of our knowledge, Ga_2O_3 -based samples (individually) as an electrocatalyst for HER are still not reported in the literature. As expected, the parent Ga_2O_3 sample did not exhibit any electrocatalytic activity under aerobic conditions within the potential range explored in the study. However, both the doped samples (GFO) demonstrated appreciable electrocatalytic activity toward the generation of H_2 through electrocatalytic water splitting (Figure 7.4(a)). Moreover, the doping percentages demonstrated an intricate relationship to the observed catalytic activity (Figure 7.4). The GFO sample with lower doping concentration ($x= 0.15$) demonstrated superior catalytic activity compared to GFO with $x= 0.30$ Fe doping (Figure 7.4(a)). GFO sample with $x= 0.15$ has an onset potential of ~ 900 mV and a Tafel slope of 210 mVdec^{-1} , whereas the GFO with $x= 0.30$ showed an onset of 1036 mV and a Tafel slope of 290 mVdec^{-1} (Figure 7.4). Three principal steps involved

in the conversion of H^+ to H_2 are commonly expressed as the Volmer (eq. 9.1), Heyrovsky (eq. 9.2), and Tafel (eq. 9.3) equations:



The high value of the Tafel slope for GFO samples reveals that the process is mostly governed through the Volmer-Heyrovsky mechanism. The inset of Figure 7.4(a) demonstrates the enlarged view of selected potential range showing the onset potential for each sample. The lower-onset potential and Tafel slope, in combination with a higher current density, revealed the superiority of $x=0.15$ GFO sample and also emphasize the importance of ideal doping content to get enhanced catalytic activity. The electrocatalytic generation of H_2 demonstrated here proves for the first time that simple doping can evoke novel electrocatalytic performances in Ga_2O_3 -based material systems.

We believe that the inculcation and modulation of electrocatalytic activity in traditionally noncatalytic Ga_2O_3 samples through Fe doping are the result of three disparate mechanisms. While it is trivial to mention that the creation of new catalytic centers in Ga_2O_3 through Fe is the reason for the electrocatalytic performance, the nonlinear and bell-shaped behavior of catalytic activity points to a more complex enabling mechanism. It is reported that transition-metal doping adjacent to catalytic centers (mostly electronegative elements such as oxygen or sulfur) in electrocatalysts can enhance its activity by lowering the hydrogen adsorption free energy (ΔG_H).¹⁵⁷⁻¹⁵⁹ Hence, the lattice inclusion of Fe while doping creates highly catalytic centers and lowers hydrogen adsorption free energy (ΔG_H) by weakening the bonds between Ga and O atoms in the lattice, resulting in a more favorable adsorption of proton and its subsequent reduction to H_2 . However,

this still does not explain the modulation of catalytic activity with respect to doping content, as well as the bell-shaped behavior of the activity.

The dependence of electron mobility and conductivity of the sample on catalyst performance in HER is well demonstrated. A higher electron mobility and conductivity will allow the generated electrons to travel across the catalyst to reach the active centers to enable faster reduction, which results in lower-onset potential. The presence of metals in the sample is expected to minimally raise the conductivity values of the doped samples. However, the enhanced conductivity does not seem to follow a linear relationship with doping. From the XPS study (**Figure 6.10**), it is established that lower doping concentration of Fe has two valence states of +2 and +3, whereas the higher one has Fe only in the +3-oxidation state. The presence of Fe in mixed valence states can impart enhanced conductivity and electron mobility within the system via intervalence charge transfer.¹⁶⁰ Hence, between GFO sample ($x= 0.15$ and 0.30), owing to the presence of mixed valence states of Fe, the $x= 0.15$ GFO sample has the highest conductivity and hence demonstrates better activity. In addition to decreasing the ΔG_H value and increasing the conductivity, Fe doping also decreases the band gap of the material. Based on the observed catalytic activity, we hypothesize that the band positions (especially the conduction band) for doped samples are such that proton reduction is easier for the lower doping concentrations (illustrated in Figure 7.5). Hence, as a cumulative effect of the above-stated three phenomena, GFO samples with $x= 0.15$ Fe content demonstrate the best catalytic activity toward HER.

Though we were able to inculcate appreciable electrocatalytic activity in Ga_2O_3 through simple metal doping, it is worth noting that the obtained results are not optimal for their application as an efficient electrocatalyst. However, the aim of the study was to create a new avenue for Ga_2O_3 -based material in electrocatalysis and to prove that doping-induced band gap tuning can be an

effective pathway to generate tunable electrocatalytic activity in a system that had no activity in the pristine state. We postulate that engineering the doping concentration, doping type, the size and shape, inducing more catalytic centers, or creating high activity hybrids, etc. can result in Ga₂O₃-based catalyst with significantly embellished catalytic properties. However, such optimizations are beyond the scope of this work, and efforts in this direction are currently being undertaken.

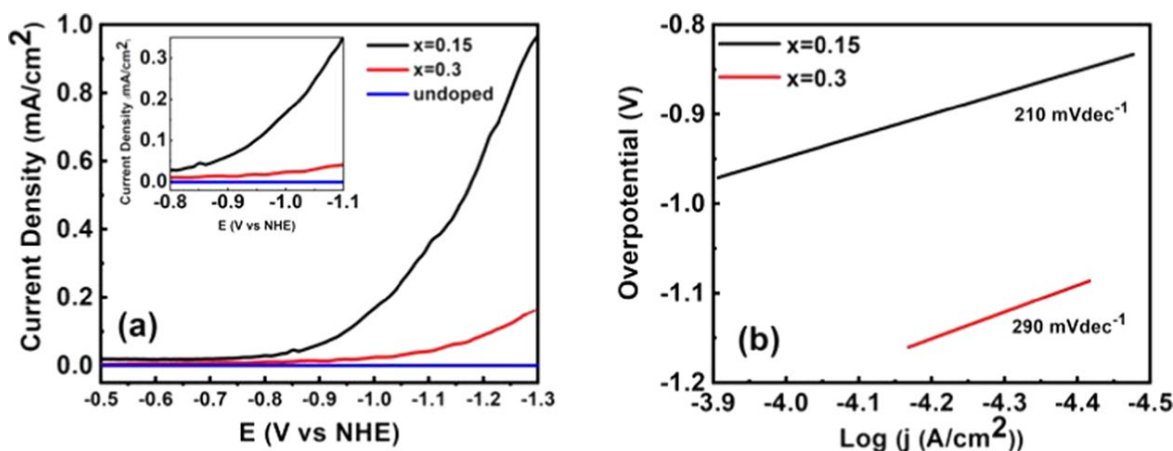


Figure 7.4: Electrochemical characterization of the doped and undoped Ga₂O₃. (a) Polarization curves obtained at a 20 mVs⁻¹ scan rate and (b) Tafel slopes for *x*= 0.15- and 0.30-doped samples.

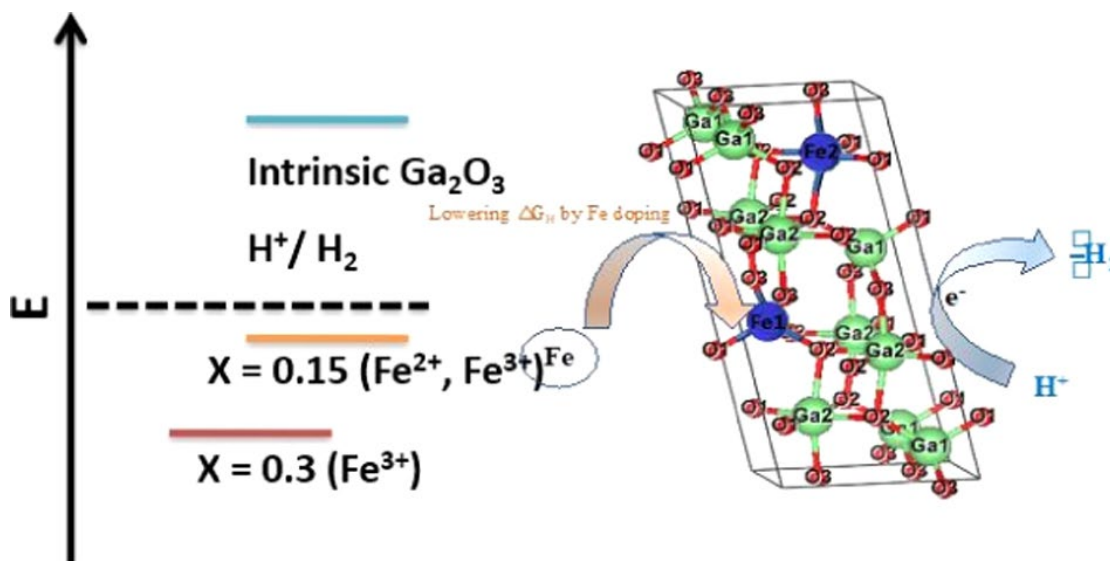


Figure 7.5: Hypothetical schematic showing the band positions in the conduction band for intrinsic and Fe-doped compounds.

Chapter 8: Summary and Conclusions

GFO ($x = 0.10$) compounds were synthesized by employing a high temperature solid-state chemical reaction method and varying the thermal conditions. The effects of thermochemical processing conditions on the structural and dielectric properties of GFO have been established. GFO materials crystallized in the β -Ga₂O₃ phase. The sintering temperature strongly influenced the microstructure and electrical properties of GFO materials. The average crystallite size varied in the range of 55-64 nm for variation at $T_{\text{sint}} = 900\text{--}1200$ °C. The particle coalescence was relatively higher and better in GFO samples sintered at 1100–1200 °C; the relative porosity decreased from 39% to 28%, with increasing T_{sint} from 900 to 1200 °C. The EDS spectral data and elemental mapping data confirmed the high chemical quality and demonstrated the uniform distribution of elemental composition throughout the microstructure of GFO materials. The deconvoluted XPS spectra of Fe 2p region showed that the Fe exhibited mixed valance state (i.e., Fe³⁺ and Fe²⁺) for $T_{\text{sint}} = 1200$ °C sample whereas single valance state (i.e. Fe³⁺) can be observed for rest of the sintered samples.

The dielectric constant values of GFO synthesized at $T_{\text{sint}} = 1200$ °C were relatively higher compared to those prepared at lower T_{sint} . The frequency dispersion of the dielectric constant fitted to the modified Debye model, which considered the multiple ions contributing to the dielectric relaxation process. The temperature-dependent dielectric constant plots indicated a thermally activated mechanism that was of sheer importance for the observed high-temperature phenomena. The spreading factor and relaxation time, calculated using Cole-Cole plots, were in the ranges of 0.65-0.76 and 10^{-4} s, respectively. The results demonstrated that densification and control over the microstructure and properties of GFO can be achieved by optimizing the sintering temperature.

New GFO compounds were fabricated maintaining the optimum synthesis condition (i.e., $T_{\text{sint}} = 1200$ °C) by varying the dopant iron concentration ($x = 0.00-0.30$). The phase purity and crystal structure of the synthesized compounds were confirmed by XRD analysis. The analysis of XRD pattern revealed that the synthesized compounds were stabilized in monoclinic phase similar to pure Ga_2O_3 with a $C2/m$ space group. Morphology of the sintered samples revealed rod-shaped particle features, and, with increasing Fe content, the particle size distribution got narrowed down. The stoichiometry of the compounds was verified by EDS. It was evident from chemical analysis that almost each compound maintained the proper stoichiometric ratio with desired composition. XANES study also revealed that the doped iron species nearly equally substituted Ga^{3+} from both tetrahedral and octahedral coordinate positions. Frequency-dependent dielectric behavior of all the synthesized compounds replicated the Maxwell-Wagner type dielectric relaxation at lower frequencies. Temperature-dependent dielectric data also exhibited salient characteristic features of the GFO compounds. The spreading factor values increased from about 0.58-0.60 on increasing the Fe concentration in intrinsic Ga_2O_3 . The scientific understanding derived from this model system of Fe doping into Ga_2O_3 may be useful and can be applicable to a large class of transition metal doped Ga_2O_3 materials.

Chemical analyses indicated high-quality GFO materials, where Fe exhibited mixed chemical valence states (Fe^{3+} , Fe^{2+}) for a lower concentration of Fe doping. However, for doping with higher Fe ($x = 0.20-0.30$) content, iron ions exhibited only the single chemical valence state (Fe^{3+}). Significant red shift of the optical band gap occurred in GFO compounds compared to intrinsic Ga_2O_3 . Iron doping facilitated strong sp-d exchange interaction, which originated from the $3d^5$ electrons of Fe^{3+} , was accounted for the observed red shift in the GFO compounds. In

addition, a signature of Fe^{3+} - Fe^{3+} double excitation process was evident as a small optical absorption edge at ≈ 450 nm in GFO compounds.

Moreover, GFO compounds ($x = 0.00, 0.15,$ and 0.30) exhibited electrocatalytic water splitting toward the generation of H_2 in contrast to intrinsic Ga_2O_3 . The onset potentials and Tafel slopes of two GFO ($x = 0.15$ and 0.30) samples were like: onset potential ~ 900 mV and Tafel slope ~ 210 mVdec⁻¹ for $x = 0.15$ and onset potential ~ 1036 mV and Tafel slope ~ 290 mVdec⁻¹ for $x = 0.30$. The electrocatalytic activity of the Fe doped compounds was attributed to create new catalytic centers, enhanced conductivity, and electron mobility. As a concluding and general remark, for the first time, we explored a new pathway of deriving electrocatalytic behavior in Fe-doped Ga_2O_3 , while such activity was totally absent in the intrinsic or undoped phase. Therefore, the outcomes and implications derived from this work may be applicable to a large class of compounds, and further options may be available to design functional materials for electrocatalytic energy production.

Chapter 9: Future Studies

The following suggestions can be adopted to accomplish more extensive research on this material system:

1. Measurement of electrical properties employing Hall effect in order to determine the carrier mobility, carrier concentration, and the type of conductivity. This experiment can also provide information which may be critical for versatile applications such as solar cell transistor, diodes, transparent conductive oxides (TCO) and high-power electronics.
2. This hybrid material system can be used for efficient thin film fabrication for extreme environment sensor application.
3. As we doped iron in Ga_2O_3 in our case, we can do the opposite i.e., doping of Ga in Fe_2O_3 and compare the respective properties.
4. Other transparent metal ions can also be doped in Ga_2O_3 in order to find new avenues of solving different scientific puzzles.

Bibliography

1. World Energy Outlook 2017 IEA (2017), "World Energy Outlook 2017", IEA, Paris <https://www.iea.org/reports/world-energy-outlook-2017>.
2. Ren, Q.; Wang, H.; Lu, X. F.; Tong, Y. X.; Li, G. R., Recent Progress on MOF-Derived Heteroatom-Doped Carbon-Based Electrocatalysts for Oxygen Reduction Reaction. *Advanced Science* **2018**, *5* (3), 1700515.
3. Zeng, M.; Li, Y., Recent advances in heterogeneous electrocatalysts for the hydrogen evolution reaction. *Journal of Materials Chemistry A* **2015**, *3* (29), 14942-14962.
4. Gong, M.; Dai, H., A mini review of NiFe-based materials as highly active oxygen evolution reaction electrocatalysts. *Nano Research* **2015**, *8* (1), 23-39.
5. Morales-Guio, C. G.; Stern, L.-A.; Hu, X., Nanostructured hydrotreating catalysts for electrochemical hydrogen evolution. *Chemical Society Reviews* **2014**, *43* (18), 6555-6569.
6. Turner, J. A., Sustainable hydrogen production. *Science* **2004**, *305* (5686), 972-974.
7. Chen, Z.; Higgins, D.; Yu, A.; Zhang, L.; Zhang, J., A review on non-precious metal electrocatalysts for PEM fuel cells. *Energy & Environmental Science* **2011**, *4* (9), 3167-3192.
8. Domen, K.; Ikeda, S.; Takata, T.; Tanaka, A.; Hara, M.; Kondo, J. N., Mechano-catalytic overall water-splitting into hydrogen and oxygen on some metal oxides. *Applied energy* **2000**, *67* (1-2), 159-179.
9. Wang, J.; Zhong, H.-x.; Wang, Z.-l.; Meng, F.-l.; Zhang, X.-b., Integrated three-dimensional carbon paper/carbon tubes/cobalt-sulfide sheets as an efficient electrode for overall water splitting. *ACS nano* **2016**, *10* (2), 2342-2348.
10. Huang, Z.-F.; Song, J.; Li, K.; Tahir, M.; Wang, Y.-T.; Pan, L.; Wang, L.; Zhang, X.; Zou, J.-J., Hollow cobalt-based bimetallic sulfide polyhedra for efficient all-pH-value electrochemical

and photocatalytic hydrogen evolution. *Journal of the American Chemical Society* **2016**, *138* (4), 1359-1365.

11. Qian, Y.; Khan, I. A.; Zhao, D., Electrocatalysts derived from metal–organic frameworks for oxygen reduction and evolution reactions in aqueous media. *Small* **2017**, *13* (37), 1701143.

12. Tian, N.; Zhou, Z.-Y.; Sun, S.-G.; Ding, Y.; Wang, Z. L., Synthesis of tetrahexahedral platinum nanocrystals with high-index facets and high electro-oxidation activity. *science* **2007**, *316* (5825), 732-735.

13. Gu, H.; Fan, W.; Liu, T., Phosphorus-doped NiCo₂S₄ nanocrystals grown on electrospun carbon nanofibers as ultra-efficient electrocatalysts for the hydrogen evolution reaction. *Nanoscale Horizons* **2017**, *2* (5), 277-283.

14. Roy, N.; Leung, K. T.; Pradhan, D., Nitrogen doped reduced graphene oxide based Pt–TiO₂ nanocomposites for enhanced hydrogen evolution. *The Journal of Physical Chemistry C* **2015**, *119* (33), 19117-19125.

15. Khdary, N. H.; Ghanem, M. A., Highly dispersed platinum nanoparticles supported on silica as catalyst for hydrogen production. *RSC Advances* **2014**, *4* (91), 50114-50122.

16. Zhang, H.; Hu, C.; Chen, S.; Zhang, K.; Wang, X., Synthesis of SnO₂ nanostructures and their application for hydrogen evolution reaction. *Catalysis letters* **2012**, *142* (6), 809-815.

17. Kumar, K.; Canaff, C.; Rousseau, J.; Arrii-Clacens, S.; Napporn, T. k. W.; Habrioux, A. I.; Kokoh, K. B., Effect of the Oxide–Carbon Heterointerface on the Activity of Co₃O₄/NRGO Nanocomposites toward ORR and OER. *The Journal of Physical Chemistry C* **2016**, *120* (15), 7949-7958.

18. Miura, A.; Rosero-Navarro, C.; Masubuchi, Y.; Higuchi, M.; Kikkawa, S.; Tadanaga, K., Nitrogen-Rich Manganese Oxynitrides with Enhanced Catalytic Activity in the Oxygen Reduction Reaction. *Angewandte Chemie International Edition* **2016**, *55* (28), 7963-7967.
19. Xia, W.-Y.; Li, N.; Li, Q.-Y.; Ye, K.-H.; Xu, C.-W., Au-NiCo₂O₄ supported on three-dimensional hierarchical porous graphene-like material for highly effective oxygen evolution reaction. *Scientific reports* **2016**, *6*, 23398.
20. Li, T.; Xue, B.; Wang, B.; Guo, G.; Han, D.; Yan, Y.; Dong, A., Tubular monolayer superlattices of hollow Mn₃O₄ nanocrystals and their oxygen reduction activity. *Journal of the American Chemical Society* **2017**, *139* (35), 12133-12136.
21. Liu, L.; Wang, J.; Hou, Y.; Chen, J.; Liu, H. K.; Wang, J.; Wu, Y., Self-Assembled 3D Foam-Like NiCo₂O₄ as Efficient Catalyst for Lithium Oxygen Batteries. *Small* **2016**, *12* (5), 602-611.
22. Park, M. G.; Lee, D. U.; Seo, M. H.; Cano, Z. P.; Chen, Z., 3D ordered mesoporous bifunctional oxygen catalyst for electrically rechargeable zinc-air batteries. *Small* **2016**, *12* (20), 2707-2714.
23. Shanmugam, S.; Gedanken, A., Synthesis and electrochemical oxygen reduction of platinum nanoparticles supported on mesoporous TiO₂. *The Journal of Physical Chemistry C* **2009**, *113* (43), 18707-18712.
24. Bauer, A.; Chevallier, L.; Hui, R.; Cavaliere, S.; Zhang, J.; Jones, D.; Rozière, J., Synthesis and characterization of Nb-TiO₂ mesoporous microsphere and nanofiber supported Pt catalysts for high temperature PEM fuel cells. *Electrochimica acta* **2012**, *77*, 1-7.
25. Ercolano, G.; Cavaliere, S.; Jones, D. J.; Rozière, J., Electrospun Ni nanofibres as Pt supports for PEMFC electrodes. *ECS Transactions* **2015**, *69* (17), 1237-1242.

26. Du, Q.; Wu, J.; Yang, H., Pt@ Nb-TiO₂ catalyst membranes fabricated by electrospinning and atomic layer deposition. *ACS Catalysis* **2014**, *4* (1), 144-151.
27. Savych, I.; Subianto, S.; Nabil, Y.; Cavaliere, S.; Jones, D.; Rozière, J., Negligible degradation upon in situ voltage cycling of a PEMFC using an electrospun niobium-doped tin oxide supported Pt cathode. *Physical Chemistry Chemical Physics* **2015**, *17* (26), 16970-16976.
28. Park, H. W.; Lee, D. U.; Zamani, P.; Seo, M. H.; Nazar, L. F.; Chen, Z., Electrospun porous nanorod perovskite oxide/nitrogen-doped graphene composite as a bi-functional catalyst for metal air batteries. *Nano Energy* **2014**, *10*, 192-200.
29. Chikoidze, E.; Fellous, A.; Perez-Tomas, A.; Sauthier, G.; Tchelidze, T.; Ton-That, C.; Huynh, T. T.; Phillips, M.; Russell, S.; Jennings, M., P-type β -gallium oxide: a new perspective for power and optoelectronic devices. *Materials Today Physics* **2017**, *3*, 118-126.
30. Zheng, B.; Hua, W.; Yue, Y.; Gao, Z., Dehydrogenation of propane to propene over different polymorphs of gallium oxide. *Journal of Catalysis* **2005**, *232* (1), 143-151.
31. Rafique, S.; Han, L.; Tadjer, M. J.; Freitas Jr, J. A.; Mahadik, N. A.; Zhao, H., Homoepitaxial growth of β -Ga₂O₃ thin films by low pressure chemical vapor deposition. *Applied Physics Letters* **2016**, *108* (18), 182105.
32. López, I. a.; Nogales, E.; Méndez, B.; Piqueras, J.; Peche, A.; Ramírez-Castellanos, J.; González-Calbet, J. M., Influence of Sn and Cr doping on morphology and luminescence of thermally grown Ga₂O₃ nanowires. *The Journal of Physical Chemistry C* **2013**, *117* (6), 3036-3045.
33. Zhang, W.; Naidu, B. S.; Ou, J. Z.; O'Mullane, A. P.; Chrimes, A. F.; Carey, B. J.; Wang, Y.; Tang, S.-Y.; Sivan, V.; Mitchell, A., Liquid metal/metal oxide frameworks with incorporated Ga₂O₃ for photocatalysis. *ACS applied materials & interfaces* **2015**, *7* (3), 1943-1948.

34. Sakata, Y.; Matsuda, Y.; Yanagida, T.; Hirata, K.; Imamura, H.; Teramura, K., Effect of metal ion addition in a Ni supported Ga₂O₃ photocatalyst on the photocatalytic overall splitting of H₂O. *Catalysis letters* **2008**, *125* (1-2), 22-26.
35. Wang, X.; Shen, S.; Jin, S.; Yang, J.; Li, M.; Wang, X.; Han, H.; Li, C., Effects of Zn²⁺ and Pb²⁺ dopants on the activity of Ga₂O₃-based photocatalysts for water splitting. *Physical Chemistry Chemical Physics* **2013**, *15* (44), 19380-19386.
36. Hayashi, H.; Huang, R.; Ikeno, H.; Oba, F.; Yoshioka, S.; Tanaka, I.; Sonoda, S., Room temperature ferromagnetism in Mn-doped γ - Ga₂O₃ with spinel structure. *Applied physics letters* **2006**, *89* (18), 181903.
37. Greil, P., Advanced engineering ceramics. *Advanced Engineering Materials* **2002**, *4* (5), 247-254.
38. Du, S.; Tian, Y.; Liu, H.; Liu, J.; Chen, Y., Calcination effects on the properties of gallium-doped zinc oxide powders. *Journal of the American Ceramic Society* **2006**, *89* (8), 2440-2443.
39. Chappell, J.; Ring, T. A.; Birchall, J. D., Particle size distribution effects on sintering rates. *Journal of Applied Physics* **1986**, *60* (1), 383-391.
40. Coble, R. L., Sintering crystalline solids. II. Experimental test of diffusion models in powder compacts. *Journal of Applied Physics* **1961**, *32* (5), 793-799.
41. Hojo, J.; Oono, R.; Kato, A., The sinterability of ultrafine WC powders obtained by a CVD method. *Journal of Materials Science* **1980**, *15* (9), 2335-2344.
42. Kumar, P. J.; Nishimura, K.; Senna, M.; Düvel, A.; Heitjans, P.; Kawaguchi, T.; Sakamoto, N.; Wakiya, N.; Suzuki, H., A novel low-temperature solid-state route for nanostructured cubic garnet Li₇La₃Zr₂O₁₂ and its application to Li-ion battery. *RSC Advances* **2016**, *6* (67), 62656-62667.

43. Xu, W.; Cao, H.; Liang, L.; Xu, J.-B., Aqueous solution-deposited gallium oxide dielectric for low-temperature, low-operating-voltage indium oxide thin-film transistors: a facile route to green oxide electronics. *ACS applied materials & interfaces* **2015**, 7 (27), 14720-14725.
44. Mezzadri, F.; Calestani, G.; Boschi, F.; Delmonte, D.; Bosi, M.; Fornari, R., Crystal structure and ferroelectric properties of ϵ -Ga₂O₃ films grown on (0001)-sapphire. *Inorganic chemistry* **2016**, 55 (22), 12079-12084.
45. Yamaga, M.; Villora, E. G.; Shimamura, K.; Ichinose, N.; Honda, M., Donor structure and electric transport mechanism in β -Ga₂O₃. *Physical Review B* **2003**, 68 (15), 155207.
46. Varley, J. B.; Weber, J. R.; Janotti, A.; Van de Walle, C. G., Oxygen vacancies and donor impurities in β -Ga₂O₃. *Applied Physics Letters* **2010**, 97 (14), 142106.
47. Romanosky, R. R.; Maley, S. M. In *Harsh environment sensor development for advanced energy systems*, Micro-and Nanotechnology Sensors, Systems, and Applications V, International Society for Optics and Photonics: 2013; p 87250H.
48. Fleischer, M.; Meixner, H., Gallium oxide thin films: a new material for high-temperature oxygen sensors. *Sensors and Actuators B: Chemical* **1991**, 4 (3-4), 437-441.
49. Patil, S. B.; Kim, I. Y.; Gunjekar, J. L.; Oh, S. M.; Eom, T.; Kim, H.; Hwang, S.-J., Phase tuning of nanostructured gallium oxide via hybridization with reduced graphene oxide for superior anode performance in Li-ion battery: an experimental and theoretical study. *ACS applied materials & interfaces* **2015**, 7 (33), 18679-18688.
50. Stepanov, S.; Nikolaev, V.; Bougrov, V.; Romanov, A., GALLIUM OXIDE: PROPERTIES AND APPLICATIONS - A REVIEW. *Rev. Adv. Mater. Sci* **2016**, 44, 63-86.

51. Medvedeva, J. E.; Hettiarachchi, C. L., Tuning the properties of complex transparent conducting oxides: Role of crystal symmetry, chemical composition, and carrier generation. *Physical Review B* **2010**, *81* (12), 125116.
52. de Boisbaudran, L., On the chemical and spectroscopic characters of a new metal (gallium). *The London, Edinburgh, and Dublin Philosophical Magazine and Journal of Science* **1875**, *50* (332), 414-416.
53. Mudavakkat, V.; Atuchin, V.; Kruchinin, V.; Kayani, A.; Ramana, C., Structure, morphology and optical properties of nanocrystalline yttrium oxide (Y₂O₃) thin films. *Optical Materials* **2012**, *34* (5), 893-900.
54. Perevalov, T.; Atuchin, V. V.; Gritsenko, V.; Komonov, A.; Korolkov, I.; Pokrovsky, L. D.; Shih, C. W.; Chin, A.; Kruchinin, V. N., Optical properties of TiO₂ films deposited by reactive electron beam sputtering. **2017**.
55. Ramana, C.; Vemuri, R.; Kaichev, V.; Kochubey, V.; Saraev, A.; Atuchin, V., X-ray photoelectron spectroscopy depth profiling of La₂O₃/Si thin films deposited by reactive magnetron sputtering. *ACS applied materials & interfaces* **2011**, *3* (11), 4370-4373.
56. Ramana, C.; Atuchin, V.; Pokrovsky, L.; Becker, U.; Julien, C., Structure and chemical properties of molybdenum oxide thin films. *Journal of Vacuum Science & Technology A: Vacuum, Surfaces, and Films* **2007**, *25* (4), 1166-1171.
57. Atuchin, V. V.; Gavrilova, T. A.; Gromilov, S. A.; Kostrovsky, V. G.; Pokrovsky, L. D.; Troitskaia, I. B.; Vemuri, R.; Carbajal-Franco, G.; Ramana, C., Low-temperature chemical synthesis and microstructure analysis of GeO₂ crystals with α -quartz structure. *Crystal Growth and Design* **2009**, *9* (4), 1829-1832.

58. Tomm, Y.; Ko, J.; Yoshikawa, A.; Fukuda, T., Floating zone growth of β -Ga₂O₃: a new window material for optoelectronic device applications. *Solar energy materials and solar cells* **2001**, *66* (1-4), 369-374.
59. Ramachandran, R. K.; Dendooven, J.; Botterman, J.; Sree, S. P.; Poelman, D.; Martens, J. A.; Poelman, H.; Detavernier, C., Plasma enhanced atomic layer deposition of Ga₂O₃ thin films. *Journal of Materials Chemistry A* **2014**, *2* (45), 19232-19238.
60. Jin, C.; Kim, H.; An, S.; Lee, C., Synthesis of Au in Ga₂O₃ peapodded nanorods and their photoluminescence properties. *Chemical engineering journal* **2012**, *191*, 457-462.
61. Guo, D.; Wu, Z.; An, Y.; Li, X.; Guo, X.; Chu, X.; Sun, C.; Lei, M.; Li, L.; Cao, L., Room temperature ferromagnetism in (Ga_{1-x}Mn_x)₂O₃ epitaxial thin films. *Journal of Materials Chemistry C* **2015**, *3* (8), 1830-1834.
62. Baban, C.; Toyoda, Y.; Ogita, M., Oxygen sensing at high temperatures using Ga₂O₃ films. *Thin Solid Films* **2005**, *484* (1-2), 369-373.
63. Bartic, M.; Baban, C. I.; Suzuki, H.; Ogita, M.; Isai, M., β -Gallium Oxide as Oxygen Gas Sensors at a High Temperature. *Journal of the American Ceramic Society* **2007**, *90* (9), 2879-2884.
64. Orita, M.; Ohta, H.; Hirano, M.; Hosono, H., Deep-ultraviolet transparent conductive β -Ga₂O₃ thin films. *Applied Physics Letters* **2000**, *77* (25), 4166-4168.
65. Lopez, I.; Utrilla, A. D.; Nogales, E.; Mendez, B.; Piqueras, J.; Peche, A.; Ramírez-Castellanos, J.; González-Calbet, J. M., In-doped gallium oxide micro-and nanostructures: morphology, structure, and luminescence properties. *The Journal of Physical Chemistry C* **2012**, *116* (6), 3935-3943.

66. Shimura, K.; Yoshida, H., Effect of doped zinc species on the photocatalytic activity of gallium oxide for hydrogen production. *Physical Chemistry Chemical Physics* **2012**, *14* (8), 2678-2684.
67. Zhang, Y.; Yan, J.; Li, Q.; Qu, C.; Zhang, L.; Xie, W., Optical and structural properties of Cu-doped β -Ga₂O₃ films. *Materials Science and Engineering: B* **2011**, *176* (11), 846-849.
68. Peelaers, H.; Van de Walle, C. G., Doping of Ga₂O₃ with transition metals. *Physical Review B* **2016**, *94* (19), 195203.
69. Li, Y.; Trinchi, A.; Wlodarski, W.; Galatsis, K.; Kalantar-Zadeh, K., Investigation of the oxygen gas sensing performance of Ga₂O₃ thin films with different dopants. *Sensors and Actuators B: Chemical* **2003**, *93* (1-3), 431-434.
70. Rubio, E.; Ramana, C., Tungsten-incorporation induced red-shift in the bandgap of gallium oxide thin films. *Applied Physics Letters* **2013**, *102* (19), 191913.
71. Manandhar, S.; Ramana, C., Direct, functional relationship between structural and optical properties in titanium-incorporated gallium oxide nanocrystalline thin films. *Applied Physics Letters* **2017**, *110* (6), 061902.
72. Oleksak, R. P.; Stickle, W. F.; Herman, G. S., Aqueous-based synthesis of gallium tungsten oxide thin film dielectrics. *Journal of Materials Chemistry C* **2015**, *3* (13), 3114-3120.
73. López, I.; Alonso-Orts, M.; Nogales, E.; Méndez, B.; Piqueras, J., Influence of Li doping on the morphology and luminescence of Ga₂O₃ microrods grown by a vapor-solid method. *Semiconductor Science and Technology* **2016**, *31* (11), 115003.
74. Roy, S.; Ramana, C., Effect of Thermochemical Synthetic Conditions on the Structure and Dielectric Properties of Ga_{1.9}Fe_{0.1}O₃ Compounds. *Inorganic chemistry* **2018**, *57* (3), 1029-1039.

75. Kim, D.-Y.; Miyoshi, S.; Tsuchiya, T.; Yamaguchi, S., Electronic defect formation in Fe-doped BaZrO₃ studied by X-ray absorption spectroscopy. *Chemistry of Materials* **2014**, *26* (2), 927-934.
76. An, Y.; Guo, D.; Li, Z.; Wu, Z.; Zhi, Y.; Cui, W.; Zhao, X.; Li, P.; Tang, W., Dual-band photodetector with a hybrid Au-nanoparticles/ β -Ga₂O₃ structure. *RSC advances* **2016**, *6* (71), 66924-66929.
77. Feng, W.; Wang, X.; Zhang, J.; Wang, L.; Zheng, W.; Hu, P.; Cao, W.; Yang, B., Synthesis of two-dimensional β -Ga₂O₃ nanosheets for high-performance solar blind photodetectors. *Journal of Materials Chemistry C* **2014**, *2* (17), 3254-3259.
78. Chen, C.-C.; Chen, C.-C., Morphology and Electrical Properties of Pure and Ti-Doped Gas-Sensitive Ga₂O₃ Film Prepared by Rheotaxial Growth and Thermal Oxidation. *Journal of materials research* **2004**, *19* (4), 1105-1117.
79. Girija, K.; Thirumalairajan, S.; Mastelaro, V. R.; Mangalaraj, D., Photocatalytic degradation of organic pollutants by shape selective synthesis of β -Ga₂O₃ microspheres constituted by nanospheres for environmental remediation. *Journal of Materials Chemistry A* **2015**, *3* (6), 2617-2627.
80. Roy, R.; Hill, V.; Osborn, E., Polymorphism of Ga₂O₃ and the system Ga₂O₃—H₂O. *Journal of the American Chemical Society* **1952**, *74* (3), 719-722.
81. Levin, I.; Brandon, D., Metastable alumina polymorphs: crystal structures and transition sequences. *Journal of the american ceramic society* **1998**, *81* (8), 1995-2012.
82. Chikoidze, E.; Von Bardeleben, H.; Akaiwa, K.; Shigematsu, E.; Kaneko, K.; Fujita, S.; Dumont, Y., Electrical, optical, and magnetic properties of Sn doped α -Ga₂O₃ thin films. *Journal of Applied Physics* **2016**, *120* (2), 025109.

83. Marezio, M.; Remeika, J., Bond Lengths in the α -Ga₂O₃ Structure and the High-Pressure Phase of Ga_{2-x}Fe_xO₃. *The Journal of Chemical Physics* **1967**, *46* (5), 1862-1865.
84. Geller, S., Crystal structure of β -Ga₂O₃. *The Journal of Chemical Physics* **1960**, *33* (3), 676-684.
85. He, H.; Orlando, R.; Blanco, M. A.; Pandey, R.; Amzallag, E.; Baraille, I.; Rérat, M., First-principles study of the structural, electronic, and optical properties of Ga₂O₃ in its monoclinic and hexagonal phases. *Physical Review B* **2006**, *74* (19), 195123.
86. Shinohara, D.; Fujita, S., Heteroepitaxy of corundum-structured α -Ga₂O₃ thin films on α -Al₂O₃ substrates by ultrasonic mist chemical vapor deposition. *Japanese Journal of Applied Physics* **2008**, *47* (9R), 7311.
87. Lee, S. D.; Akaiwa, K.; Fujita, S., Thermal stability of single crystalline alpha gallium oxide films on sapphire substrates. *physica status solidi (c)* **2013**, *10* (11), 1592-1595.
88. Ahman, J.; Svensson, G.; Albertsson, J., A reinvestigation of β -Ga₂O₃ oxide. *Acta Crystallogr., Sect. C* **1996**, *52*, 1336-1338.
89. Ichinose, N.; Shimamura, K.; Aoki, K.; Villora, E. A. G., β -Ga₂O₃ single crystal growing method, thin-film single crystal growing method, Ga₂O₃ light-emitting device, and its manufacturing method. Google Patents: 2010.
90. Kuramata, A.; Koshi, K.; Watanabe, S.; Yamaoka, Y.; Masui, T.; Yamakoshi, S., High-quality β -Ga₂O₃ single crystals grown by edge-defined film-fed growth. *Japanese Journal of Applied Physics* **2016**, *55* (12), 1202A2.
91. Green, A. J.; Chabak, K. D.; Baldini, M.; Moser, N.; Gilbert, R.; Fitch, R. C.; Wagner, G.; Galazka, Z.; Mccandless, J.; Crespo, A., β -Ga₂O₃ MOSFETs for Radio Frequency Operation. *IEEE Electron Device Letters* **2017**, *38* (6), 790-793.

92. Higashiwaki, M.; Sasaki, K.; Murakami, H.; Kumagai, Y.; Koukitu, A.; Kuramata, A.; Masui, T.; Yamakoshi, S., Recent progress in Ga₂O₃ power devices. *Semiconductor Science and Technology* **2016**, *31* (3), 034001.
93. Ahn, S.; Ren, F.; Kim, J.; Oh, S.; Kim, J.; Mastro, M. A.; Pearton, S., Effect of front and back gates on β -Ga₂O₃ nano-belt field-effect transistors. *Applied Physics Letters* **2016**, *109* (6), 062102.
94. Zinkevich, M.; Morales, F. M.; Nitsche, H.; Ahrens, M.; Rühle, M.; Aldinger, F., Microstructural and thermodynamic study of γ -Ga₂O₃. *Zeitschrift für Metallkunde* **2004**, *95* (9), 756-762.
95. Huang, R.; Hayashi, H.; Oba, F.; Tanaka, I., Microstructure of Mn-doped γ -Ga₂O₃ epitaxial film on sapphire (0001) with room temperature ferromagnetism. *Journal of applied physics* **2007**, *101* (6), 063526.
96. Tabaza, W.; Swart, H.; Kroon, R., Luminescence of Ce doped MgAl₂O₄ prepared by the combustion method. *Physica B: Condensed Matter* **2014**, *439*, 109-114.
97. Tan, S.; Gil, L. B.; Subramanian, N.; Sholl, D. S.; Nair, S.; Jones, C. W.; Moore, J. S.; Liu, Y.; Dixit, R. S.; Pendergast, J. G., Catalytic propane dehydrogenation over In₂O₃-Ga₂O₃ mixed oxides. *Applied Catalysis A: General* **2015**, *498*, 167-175.
98. Kawaharamura, T.; Dang, G. T.; Furuta, M., Successful growth of conductive highly crystalline Sn-doped α -Ga₂O₃ thin films by fine-channel mist chemical vapor deposition. *Japanese Journal of Applied Physics* **2012**, *51* (4R), 040207.
99. Yoshioka, S.; Hayashi, H.; Kuwabara, A.; Oba, F.; Matsunaga, K.; Tanaka, I., Structures and energetics of Ga₂O₃ polymorphs. *Journal of Physics: Condensed Matter* **2007**, *19* (34), 346211.

100. Cótica, L. F.; Santos, G. M.; Freitas, V. F.; Coelho, A. A.; Pal, M.; Santos, I. A.; Garcia, D.; Eiras, J. A.; Guo, R.; Bhalla, A. S., Room temperature nonlinear magnetoelectric effect in lead-free and Nb-doped AlFeO₃ compositions. *Journal of Applied Physics* **2015**, *117* (6), 064104.
101. Whittingham, M. S., Solid state chemistry and its applications: Anthony R. West, John Wiley & Sons, New York (1987), 734 pages \$103.00 hardcover, \$39.95 softcover. Elsevier: 1989.
102. Wikipedia, Iron(III) Oxide.
103. Rodríguez-Carvajal, J., Recent advances in magnetic structure determination by neutron powder diffraction. *physica B* **1993**, *192* (1-2), 55-69.
104. Abràmoff, M. D.; Magalhães, P. J.; Ram, S. J., Image processing with ImageJ. *Biophotonics international* **2004**, *11* (7), 36-42.
105. Wikipedia, X-ray Photoelectron Spectroscopy.
106. Fairley, N.; Carrick, A., *Recipes for XPS Data Processing*. Acolyte Science: 2005.
107. Végh, J., The Shirley background revised. *Journal of electron spectroscopy and related phenomena* **2006**, *151* (3), 159-164.
108. Chen, L. X.; Liu, T.; Thurnauer, M. C.; Csencsits, R.; Rajh, T., Fe₂O₃ nanoparticle structures investigated by X-ray absorption near-edge structure, surface modifications, and model calculations. *The Journal of Physical Chemistry B* **2002**, *106* (34), 8539-8546.
109. Zhou, X.; Heigl, F.; Ko, J.; Murphy, M.; Zhou, J.; Regier, T.; Blyth, R.; Sham, T., Origin of luminescence from Ga₂O₃ nanostructures studied using x-ray absorption and luminescence spectroscopy. *Physical Review B* **2007**, *75* (12), 125303.
110. Wikipedia, X-ray Absorption Near Edge Structure.
111. Wikipedia, Raman Spectroscopy.

112. Dakhel, A., Investigation of opto-dielectric properties of Ti-doped Ga₂O₃ thin films. *Solid state sciences* **2013**, *20*, 54-58.
113. Yao, Y.; Davis, R. F.; Porter, L. M., Investigation of different metals as ohmic contacts to β-Ga₂O₃: comparison and analysis of electrical behavior, morphology, and other physical properties. *Journal of Electronic Materials* **2017**, *46* (4), 2053-2060.
114. Mei, X.; Wang, Y.; Chen, L.; Zhang, C.; Ma, Y.; Zeng, Y.; Jiang, Y., The effects of sintering conditions on the properties of Ga-doped zinc oxide ceramics. *Materials Research Innovations* **2015**, *19* (sup9), S9-306-S9-309.
115. Troitskaia, I.; Gavrilova, T.; Gromilov, S.; Sheglov, D.; Atuchin, V.; Vemuri, R.; Ramana, C., Growth and structural properties of α-MoO₃ (0 1 0) microplates with atomically flat surface. *Materials Science and Engineering: B* **2010**, *174* (1-3), 159-163.
116. Solodovnikov, S. F.; Atuchin, V. V.; Solodovnikova, Z. A.; Khyzhun, O. Y.; Danylenko, M. I.; Pishchur, D. P.; Plyusnin, P. E.; Pugachev, A. M.; Gavrilova, T. A.; Yelissev, A. P., Synthesis, structural, thermal, and electronic properties of palmierite-related double molybdate α-Cs₂Pb(MoO₄)₂. *Inorganic chemistry* **2017**, *56* (6), 3276-3286.
117. Williamson, G.; Hall, W., X-ray line broadening from filed aluminium and wolfram. *Acta metallurgica* **1953**, *1* (1), 22-31.
118. Atuchin, V.; Gavrilova, T.; Grivel, J.-C.; Kesler, V.; Troitskaia, I., Electronic structure of layered ferroelectric high-k titanate Pr₂Ti₂O₇. *Journal of Solid State Chemistry* **2012**, *195*, 125-131.
119. Jangir, R.; Porwal, S.; Tiwari, P.; Mondal, P.; Rai, S.; Ganguli, T.; Oak, S.; Deb, S., Photoluminescence study of β-Ga₂O₃ nanostructures annealed in different environments. *Journal of Applied Physics* **2012**, *112* (3), 034307.

120. Roy, S.; Mallesham, B.; Zade, V. B.; Martinez, A.; Shutthanandan, V.; Thevuthasan, S.; Ramana, C., Correlation between Structure, Chemistry, and Dielectric Properties of Iron-Doped Gallium Oxide ($\text{Ga}_{2-x}\text{Fe}_x\text{O}_3$). *The Journal of Physical Chemistry C* **2018**, *122* (48), 27597-27607.
121. Mallesham, B.; Roy, S.; Bose, S.; Nair, A. N.; Sreenivasan, S.; Shutthanandan, V.; Ramana, C. V., Crystal Chemistry, Band-Gap Red Shift, and Electrocatalytic Activity of Iron-Doped Gallium Oxide Ceramics. *ACS Omega* **2019**.
122. Lim, C. S.; Aleksandrovsky, A. S.; Molokeev, M. S.; Oreshonkov, A. S.; Atuchin, V. V., Microwave synthesis and spectroscopic properties of ternary scheelite-type molybdate phosphors $\text{NaSrLa}(\text{MoO}_4)_3: \text{Er}^{3+}, \text{Yb}^{3+}$. *Journal of Alloys and Compounds* **2017**, *713*, 156-163.
123. Liu, Y.; Patterson, B., Grain growth inhibition by porosity. *Acta metallurgica et materialia* **1993**, *41* (9), 2651-2656.
124. NIST XPS.
125. Bandi, M.; Zade, V.; Roy, S.; Nair, A. N.; Seacat, S.; Sreenivasan, S.; Shutthanandan, V.; Van de Walle, C. G.; Peelaers, H.; Ramana, C., Effect of Ti Induced Chemical Inhomogeneity on Crystal Structure, Electronic Structure and Optical Properties of Wide Band Gap Ga_2O_3 . *Crystal Growth & Design* **2020**.
126. Zade, V.; Mallesham, B.; Roy, S.; Shutthanandan, V.; Ramana, C., Electronic Structure of Tungsten-Doped $\beta\text{-Ga}_2\text{O}_3$ Compounds. *ECS Journal of Solid State Science and Technology* **2019**, *8* (7), Q3111-Q3115.
127. Hu, X.; Yu, J. C.; Gong, J.; Li, Q.; Li, G., $\alpha\text{-Fe}_2\text{O}_3$ nanorings prepared by a microwave-assisted hydrothermal process and their sensing properties. *Advanced Materials* **2007**, *19* (17), 2324-2329.

128. Kraushofer, F.; Jakub, Z.; Bichler, M.; Hulva, J.; Drmota, P.; Weinold, M.; Schmid, M.; Setvin, M.; Diebold, U.; Blaha, P., Atomic-Scale Structure of the Hematite α -Fe₂O₃ (1 $\bar{1}$ 02)“R-Cut” Surface. *The Journal of Physical Chemistry C* **2018**, *122* (3), 1657-1669.
129. Zacherle, T.; Schmidt, P.; Martin, M., Ab initio calculations on the defect structure of β -Ga₂O₃. *Physical Review B* **2013**, *87* (23), 235206.
130. Varley, J. B.; Peelaers, H.; Janotti, A.; Van de Walle, C. G., Hydrogenated cation vacancies in semiconducting oxides. *Journal of Physics: Condensed Matter* **2011**, *23* (33), 334212.
131. Dong, L.; Jia, R.; Xin, B.; Peng, B.; Zhang, Y., Effects of oxygen vacancies on the structural and optical properties of β -Ga₂O₃. *Scientific reports* **2017**, *7* (1), 1-12.
132. Ágoston, P.; Albe, K.; Nieminen, R. M.; Puska, M. J., Intrinsic n-type behavior in transparent conducting oxides: A comparative hybrid-functional study of In₂O₃, SnO₂, and ZnO. *Physical review letters* **2009**, *103* (24), 245501.
133. Ingebrigtsen, M. E.; Varley, J.; Kuznetsov, A. Y.; Svensson, B. G.; Alfieri, G.; Mihaila, A.; Badstübner, U.; Vines, L., Iron and intrinsic deep level states in Ga₂O₃. *Applied Physics Letters* **2018**, *112* (4), 042104.
134. Yu, J.; Paradis, P.-F.; Ishikawa, T.; Yoda, S.; Saita, Y.; Itoh, M.; Kano, F., Giant dielectric constant of hexagonal BaTiO₃ crystal grown by containerless processing. *Chemistry of materials* **2004**, *16* (21), 3973-3975.
135. Huang, Y.; Huang, X.; Schadler, L. S.; He, J.; Jiang, P., Core@ double-shell structured nanocomposites: a route to high dielectric constant and low loss material. *ACS applied materials & interfaces* **2016**, *8* (38), 25496-25507.
136. Kakade, S. G.; Ma, Y.-R.; Devan, R. S.; Kolekar, Y. D.; Ramana, C. V., Dielectric, complex impedance, and electrical transport properties of erbium (Er³⁺) ion-substituted

nanocrystalline, cobalt-rich ferrite ($\text{Co}_{1.1}\text{Fe}_{1.9-x}\text{Er}_x\text{O}_4$). *The Journal of Physical Chemistry C* **2016**, *120* (10), 5682-5693.

137. Koops, C., On the dispersion of resistivity and dielectric constant of some semiconductors at audiofrequencies. *Physical Review* **1951**, *83* (1), 121.

138. Verma, A.; Thakur, O.; Prakash, C.; Goel, T.; Mendiratta, R., Temperature dependence of electrical properties of nickel–zinc ferrites processed by the citrate precursor technique. *Materials Science and Engineering: B* **2005**, *116* (1), 1-6.

139. Yuan, J.-K.; Yao, S.-H.; Dang, Z.-M.; Sylvestre, A.; Genestoux, M.; Bail, J., Giant dielectric permittivity nanocomposites: realizing true potential of pristine carbon nanotubes in polyvinylidene fluoride matrix through an enhanced interfacial interaction. *The Journal of Physical Chemistry C* **2011**, *115* (13), 5515-5521.

140. Juarez-Perez, E. J.; Sanchez, R. S.; Badia, L.; Garcia-Belmonte, G.; Kang, Y. S.; Mora-Sero, I.; Bisquert, J., Photoinduced giant dielectric constant in lead halide perovskite solar cells. *The journal of physical chemistry letters* **2014**, *5* (13), 2390-2394.

141. Almond, D. P.; Bowen, C. R., An explanation of the photoinduced giant dielectric constant of lead halide perovskite solar cells. *The journal of physical chemistry letters* **2015**, *6* (9), 1736-1740.

142. Bharathi, K. K.; Ramana, C., Improved electrical and dielectric properties of La-doped Co ferrite. *Journal of Materials Research* **2011**, *26* (4), 584-591.

143. Kolekar, Y.; Sanchez, L.; Ramana, C., Dielectric relaxations and alternating current conductivity in manganese substituted cobalt ferrite. *Journal of Applied Physics* **2014**, *115* (14), 144106.

144. Mangalaraja, R.; Manohar, P.; Gnanam, F.; Awano, M., Electrical and magnetic properties of $\text{Ni}_{0.8}\text{Zn}_{0.2}\text{Fe}_2\text{O}_4$ /silica composite prepared by sol-gel method. *Journal of materials science* **2004**, *39* (6), 2037-2042.
145. Ramana, C.; Kolekar, Y.; Kamala Bharathi, K.; Sinha, B.; Ghosh, K., Correlation between structural, magnetic, and dielectric properties of manganese substituted cobalt ferrite. *Journal of applied physics* **2013**, *114* (18), 183907.
146. He, Y.; Miao, Y.; Li, C.; Wang, S.; Cao, L.; Xie, S.; Yang, G.; Zou, B.; Burda, C., Size and structure effect on optical transitions of iron oxide nanocrystals. *Physical review B* **2005**, *71* (12), 125411.
147. Hashimoto, T.; Yamada, T.; Yoko, T., Third-order nonlinear optical properties of sol-gel derived $\alpha\text{-Fe}_2\text{O}_3$, $\gamma\text{-Fe}_2\text{O}_3$, and Fe_3O_4 thin films. *Journal of applied physics* **1996**, *80* (6), 3184-3190.
148. Toloman, D.; Popa, A.; Stan, M.; Silipas, T.; Biris, A. In *Identification of different iron sites in $\beta\text{-Ga}_2\text{O}_3$ nanoparticles by spectroscopic methods*, AIP Conference Proceedings, AIP Publishing LLC: 2015; p 060005.
149. Onuma, T.; Saito, S.; Sasaki, K.; Masui, T.; Yamaguchi, T.; Honda, T.; Higashiwaki, M., Valence band ordering in $\beta\text{-Ga}_2\text{O}_3$ studied by polarized transmittance and reflectance spectroscopy. *Japanese Journal of Applied Physics* **2015**, *54* (11), 112601.
150. Shannon, R. D., Revised effective ionic radii and systematic studies of interatomic distances in halides and chalcogenides. *Acta crystallographica section A: crystal physics, diffraction, theoretical and general crystallography* **1976**, *32* (5), 751-767.

151. Bouaine, A.; Brihi, N.; Schmerber, G.; Ulhaq-Bouillet, C.; Colis, S.; Dinia, A., Structural, optical, and magnetic properties of Co-doped SnO₂ powders synthesized by the coprecipitation technique. *The Journal of Physical Chemistry C* **2007**, *111* (7), 2924-2928.
152. Li, Y.; Sun, J.; Meng, X.; Chu, J.; Zhang, W., Structural and optical properties of Ba (Co_x,Ti_{1-x})O₃ thin films fabricated by sol-gel process. *Applied physics letters* **2004**, *85* (11), 1964-1966.
153. Stroud, D.; Ehrenreich, H., Band structure of SiGe: Coherent-potential approximation. *Physical Review B* **1970**, *2* (8), 3197.
154. Mu, W.; Yin, Y.; Jia, Z.; Wang, L.; Sun, J.; Wang, M.; Tang, C.; Hu, Q.; Gao, Z.; Zhang, J., An extended application of β-Ga₂O₃ single crystals to the laser field: Cr⁴⁺: β-Ga₂O₃ utilized as a new promising saturable absorber. *RSC Advances* **2017**, *7* (35), 21815-21819.
155. Tamura, T.; Setomoto, T.; Taguchi, T., Illumination characteristics of lighting array using 10 candela-class white LEDs under AC 100V operation. *Journal of Luminescence* **2000**, *87*, 1180-1182.
156. Li, X.; Zhen, X.; Meng, S.; Xian, J.; Shao, Y.; Fu, X.; Li, D., Structuring β-Ga₂O₃ photonic crystal photocatalyst for efficient degradation of organic pollutants. *Environmental science & technology* **2013**, *47* (17), 9911-9917.
157. Escalera-López, D.; Niu, Y.; Yin, J.; Cooke, K.; Rees, N. V.; Palmer, R. E., Enhancement of the hydrogen evolution reaction from Ni-MoS₂ hybrid nanoclusters. *ACS catalysis* **2016**, *6* (9), 6008-6017.
158. Hota, P.; Bose, S.; Dinda, D.; Das, P.; Ghorai, U. K.; Bag, S.; Mondal, S.; Saha, S. K., Nickel-Doped Silver Sulfide: An Efficient Air-Stable Electrocatalyst for Hydrogen Evolution from Neutral Water. *ACS omega* **2018**, *3* (12), 17070-17076.

159. Shi, Y.; Zhou, Y.; Yang, D.-R.; Xu, W.-X.; Wang, C.; Wang, F.-B.; Xu, J.-J.; Xia, X.-H.; Chen, H.-Y., Energy level engineering of MoS₂ by transition-metal doping for accelerating hydrogen evolution reaction. *Journal of the American Chemical Society* **2017**, *139* (43), 15479-15485.
160. Park, J. G.; Aubrey, M. L.; Oktawiec, J.; Chakarawet, K.; Darago, L. E.; Grandjean, F.; Long, G. J.; Long, J. R., Charge delocalization and bulk electronic conductivity in the mixed-valence metal–organic framework Fe(1,2,3-triazolate)₂(BF₄)_x. *Journal of the American Chemical Society* **2018**, *140* (27), 8526-8534.

Vita

Swadipta Roy was born on November 9, 1989, in India. In February 2014, Mr. Roy received Bachelor of Engineering in Metallurgy and Materials Engineering from the Bengal Engineering and Science University, Shibpur (BESUS). Immediately after that, he enrolled in the graduate program for Metallurgical Engineering and Material Science at Indian Institute of Technology Bombay (IIT B) and received a Master of Technology degree with specialization in Corrosion Science and Engineering in August 2015. Mr. Roy then worked as a project staff at IIT B for a year. Mr. Roy started his Ph.D. in the University of Texas at El Paso in August 2016 in the Department of Metallurgical, Materials and Biomedical Engineering. He spent more than a year as a Ph.D. Research Intern at Pacific Northwest National Laboratory (PNNL) during 2018-2019. He has currently two first author and several co-author publications in various innovative scientific journals.

Contact Information: swadiptaroy@gmail.com